

Ultrafast Energy Transfer Processes in Functional Organic Materials: Quantum Dynamical Treatment Including Noise and Disorder

Dissertation

zur Erlangung des Doktorgrades
der Naturwissenschaften

vorgelegt beim Fachbereich 14
der Johann Wolfgang Goethe-Universität
in Frankfurt am Main

von

Jan Michael Wahl

aus

Frankfurt am Main

Frankfurt am Main
2016

(D30)

vom Fachbereich 14 Biochemie, Chemie und Pharmazie
der Johann Wolfgang Goethe - Universität als Dissertation angenommen.

Dekan: Prof. Dr. Michael Karas
Gutachter: Prof. Dr. Irene Burghardt
Prof. Dr. Josef Wachtveitl

Datum der Disputation:

Abstract

Photoinduced energy transfer processes and reactions play an important role in many areas of chemistry, physics and biology. Among the most prominent examples are biological light-harvesting in photosynthesis and excitation energy transfer in functional materials. Here, we focus upon the second type of systems, which are used, e.g., in organic electronics as well as in a variety of tailored donor-acceptor units and switches. More specifically, we study two types of functional organic systems: First, oligo-*para*-phenylene-vinylene (OPV) and oligo-thiophene (OT) as building blocks for paradigm materials used in organic photovoltaics. Second, a small donor-acceptor dyad, i.e., dithienylethene boron-dipyrromethene (DTE-BODIPY) which has been developed and investigated in collaboration with the experimental groups of K. Rück-Braun (TU Berlin) and J. Wachtveitl (Goethe University).

In order to understand the relevant energy transfer mechanisms, we employ first-principles electronic structure and quantum dynamical studies. Parametrized model Hamiltonians based on high-level *ab initio* calculations are combined with high-dimensional quantum dynamical or mixed quantum-classical simulations. The parametrization of the Hamiltonian is carried out for small fragments which allow for an electronic-structure treatment, while the Hamiltonian as such can be used for much larger systems. The dynamical calculations rely either on the Multi-Configuration Time-Dependent Hartree (MCTDH) method which permits a full quantum treatment, or else on the semi-classical Ehrenfest method, which allows to treat larger systems. The Ehrenfest method was implemented in an independent code, including Langevin driving by an environment.

In the oligomer (OPV, OT) systems, the dynamics in the presence of a structural defect was investigated. We aim to understand the dynamical phenomena induced by photoexcitation, which involve the migration of electronic excitations (excitons). We also aim to clarify the "spectroscopic unit" concept that postulates the confinement of photoinduced electronic excitations (excitons) due to geometric defects.

The system is defined in a Frenkel exciton basis, where each basis function describes strongly localized electron-hole pairs on a monomer unit. Delocalized electronic excitations are represented as superpositions of such localized Frenkel states. Beyond the Frenkel picture, a generalized electron-hole basis including charge-transfer states, i.e., allowing for spatial separation of electrons and holes, is also addressed. The parametrization of the model Hamiltonian is based upon high level electronic structure calculations by the Algebraic Diagrammatic Construction (ADC(2)) method, in conjunction with a transition density analysis. This level of treatment

allows a correct identification of the supermolecular states as Frenkel type exciton states, and their distinction from charge-transfer states. To include vibronic effects, low and high-frequency modes representing torsional and bond-length-alternation (BLA) coordinates of the system are included. To this end, potential energy surface (PES) cuts are carried out and mapped upon a global potential surface.

With this setup, the quantum dynamical and mixed quantum-classical simulations for hexamer and 20-mer OPV and OT species were carried out. These calculations show that excitation energy transfer takes place on a sub-picosecond time scale and strongly correlates with structural defects. In the hexamer system, a coherent spreading of the exciton across a torsional defect is observed and simulations of a 20-mer system provide evidence for a „coherent hopping“ type mechanism of exciton migration. On a time scale of less than 100 femtoseconds, exciton trapping effects are observed. The effect of fluctuations is included either at a quantum level (quantum fluctuations at $T=0$) or else via the semi-classical Ehrenfest/Langevin approach. The latter is not adequate to describe the details of exciton dynamics and trapping, but is suitable to model a fluctuation-driven hopping type dynamics of trapped states on a longer time scale and as a function of temperature.

The study of the photodynamics of the second system, i.e., the DTE-BODIPY dyad, aims to explain the experimentally observed ultrafast appearance of vibrational excitation of the BODIPY moiety, following electronic excitation of the DTE moiety in a time-resolved UV/Vis pump-probe experiment. Our study therefore focuses on the photoinduced vibrational energy redistribution (IVR) on a sub-ps time scale. A model Hamiltonian representing the DTE-BODIPY dyad is developed and parametrized using Time-Dependent Density Functional Theory (TDDFT) calculations. From a complete set of normal modes, localized modes on the DTE and BODIPY moieties are constructed, some of which are coupled and transmit vibrational excitation to the BODIPY moiety. This transfer is found to be driven by a reservoir of vibronically excited DTE modes. The time scale and characteristic frequencies of the experimentally observed IVR process are well reproduced by our high-dimensional MCTDH simulations. A strong dependence of the IVR process on local and environmental couplings is found.

Zusammenfassung

Photoinduzierte Energietransferprozesse und -reaktionen spielen in vielen Gebieten von Chemie, Physik und Biologie eine wichtige Rolle. Zu den prominentesten Beispielen zählen der Lichtsammelprozess in der Photosynthese und der Anregungsenergieübertrag in funktionellen Materialien. Der Fokus dieser Arbeit liegt auf letzterem Bereich, genauer auf organischer Elektronik und flexiblen Donor-Akzeptor-Bausteinen und Schaltern. Im Besonderen werden hier zwei verschiedene Typen von funktionellen organischen Systemen betrachtet: zum einen oligomere Fragmente organischer halbleitender Polymere wie Oligo-*p*-Phenylene-Vinylene (OPV) und Oligo-Thiophen (OT), welche als Bausteine für neuartige organische Solarzellen dienen, und zum anderen kleine funktionelle Donor-Akzeptor-Einheiten wie Dithienylethen-Borodipyrromethen (DTE-BODIPY). Letzteres wurde in Kooperation mit den experimentellen Gruppen von K. Rück-Braun (TU Berlin) und J. Wachtveitl (Goethe Universität) untersucht.

Um die relevanten Energietransfermechanismen genauer zu verstehen, wurden an diesen Systemen elektronische Strukturrechnungen und quantendynamische Untersuchungen durchgeführt. Hierzu wurden mittels *ab initio*-Methoden Modell-Hamiltonians parametrisiert und mit hochdimensionalen quantendynamischen oder semiklassischen Methoden kombiniert. Während die Parametrisierung für kleinere Fragmente durchgeführt wurde, lässt sich der so parametrisierte Hamiltonian ohne Weiteres auf größere Systeme erweitern. Die dynamischen Studien der betreffenden Systeme wurden mittels der Multikonfigurationellen Zeitabhängigen Hartree (MCTDH)-Methode durchgeführt, welche eine vollständige quantendynamische Beschreibung des Systems zulässt. Für größere Systeme wurde die semiklassische Ehrenfest Methode in Verbindung mit dem Langevin-Ansatz zur Beschreibung von Umgebungseffekten genutzt. Hierzu wurde ein eigens für diese Methode und Systeme geschriebenes Programm eingesetzt.

Im Falle der OT- und OPV-Oligomere wurde die Dynamik bei Vorliegen eines strukturellen Defekts untersucht. Ziel war es hierbei, die dynamischen Phänomene, welche durch die Photoanregung induziert werden, zu untersuchen. Des Weiteren wurde untersucht, ob das Konzept von „spektroskopischen Einheiten“, welche die Lokalisierung der Anregung durch strukturelle Defekte beschreibt, in diesen Systemen zutrifft. Hierzu wurden die Systeme in einer Frenkel-Basis definiert, welche ein auf einem Monomer lokalisiertes Elektron-Loch-Paar beschreibt. Delokalisierte elektronische Anregungen können somit als Superposition solcher Frenkel-Zustände beschrieben werden. Neben der Frenkel-Basis wurde aber auch eine verallgemeinerte Elektron-Loch-Basis verwendet, welche über zusätzliche Ladungstransferzustände eine räumliche Separation von Elektronen und Löchern erlaubt.

Die Parametrisierung des OPV- und OT-Hamiltonians erfolgte mittels der Algebraischen Diagrammatischen Konstruktions (ADC(2))-Methode, welche in Kombination mit einer Übergangs-Dichte-Matrix-Analyse eine sehr akkurate Beschreibung der Frenkel- und Ladungstransferzustände basierend auf den supermolekularen Zuständen erlaubt. Um vibronische Effekte auf die Dynamik miteinzubeziehen, wurden nieder- und hochfrequente Torsions- und alternierende Bindungslängenmoden des Systems im Hamiltonian berücksichtigt. Hierzu wurden eindimensionale Schnitte der Potentialflächen entlang dieser Koordinaten berechnet und mittels einer Transformation in diabatische Potentialflächen überführt.

Mit diesem Setup wurden die quantendynamischen und semiklassischen Simulationen für ein OPV/OT-Hexamere und ein 20-mer durchgeführt. Die Ergebnisse dieser Simulationen zeigen, dass der Energietransfer auf einer Subpikosekunden-Zeitskala stattfindet und eine starke Abhängigkeit vom Vorliegen eines strukturellen Defekts aufweist. Des Weiteren konnte auf einer Zeitskala von 100 Femtosekunden eine Lokalisierung des Exzitons beobachtet werden. Fluktuationseffekte werden zudem über Quantenfluktuationen im Falle von MCTDH bzw. über thermische Fluktuationen im Falle des Ehrenfest-/Langevin-Ansatzes berücksichtigt. Letzterer ist jedoch nicht in der Lage, die kohärente Charakteristik der mit den Schwingungsmoden gekoppelten Exziton- und Lokalisierungsdynamik wiederzugeben. Dagegen kann dieser Ansatz erfolgreich genutzt werden, um eine fluktuationsgetriebene „Hopping“-Dynamik des quasi-stationären Zustandes auf einer längeren Zeitskala in Abhängigkeit von der Temperatur zu beschreiben.

Die Beschreibung der Photodynamik der DTE-BODIPY-Dyade zielt darauf ab, experimentell beobachtete vibrationelle Schwingungen des BODIPY-Fragments zu erklären, die ohne eine direkte Anregung dieses Fragments zustande kommen. Diese wurden nach einer selektiven Anregung des DTE-Fragments in zeitaufgelösten UV/Vis Anreg-Abtast-Experimenten beobachtet. Der Fokus der Untersuchung liegt daher auf der Beschreibung der photoinduzierten intramolekulare Energieumverteilung (IVR) auf einer Subpikosekunden-Zeitskala. Die DTE-BODIPY-Dyade wurde mittels eines Hamiltonians, welcher durch TDDFT-Rechnungen parametrisiert wurde, dargestellt. Basierend auf den Normalmoden des Systems, wurden lokale DTE- und BODIPY-Moden konstruiert, wobei einige dieser Moden miteinander gekoppelt sind und die Photoanregung des DTE auf das BODIPY-Fragment übertragen. Hierbei zeigte sich, dass die Zeitskala und die charakteristischen Frequenzen des Experiments mittels der hochdimensionalen MCTDH-Methode gut reproduziert wurden. Aus den Simulationen ergab sich zudem, dass der beobachtete Energietransfer stark von einem Reservoir von vibrationell angeregten lokalen DTE-Moden beeinflusst wird. Der untersuchte IVR- Prozess zeigt zudem eine ausgeprägte Abhängigkeit von lokalen Kopplungen und der Kopplung an eine Umgebung.

Contents

List of Figures	III
List of Tables	V
1 Deutsche Zusammenfassung	1
2 Introduction	9
3 Theoretical Background	17
3.1 Energy Transfer Models for Inorganic and Organic Systems	17
3.2 Energy Transfer in Silicon and Organic Polymer based Solar Cells .	24
3.3 Model Hamiltonians for Energy Transfer Processes	26
4 Theoretical Methods	31
4.1 Basic Approximations and <i>ab initio</i> Methods	32
4.1.1 The Born-Oppenheimer Approximation	32
4.1.2 Hartree-Fock	34
4.1.3 DFT and TDDFT	35
4.1.4 High-Level <i>ab initio</i> Methods: MP2, CC2 and ADC(2) . . .	37
4.2 Beyond Born-Oppenheimer	42
4.3 Multiconfiguration Time-Dependent Hartree	43
4.4 Ehrenfest Dynamics	44
4.4.1 Ehrenfest Equations of Motion: Wave Function Based Ansatz	46
4.4.2 Ehrenfest Equations of Motion: Density Matrix Based Ansatz	47
4.4.3 Multiconfigurational Ehrenfest Dynamics	48
5 Results	55
5.1 Implementation of Ehrenfest Dynamics	57
5.2 Exact Adiabatic-to-Diabatic Transformation	65
5.3 Exciton Dynamics on a Minimal Oligo-Thiophene Lattice	69
5.3.1 Quantum Chemical Method and Model	71
5.3.2 Model Hamiltonian	73
5.3.3 Electronic Structure Calculations	75
5.3.4 Exciton Dynamics on a Minimal Lattice	83
5.3.5 Exciton Dynamics on a Large Lattice	89
5.3.6 Conclusion	93

5.4	Exciton Dynamics on a Minimal Oligo- <i>p</i> -Phenylene Vinylene Lat- tice studied by MCTDH and Ehrenfest Dynamics	97
5.4.1	Model System and Model Hamiltonian	98
5.4.2	Quantum Dynamics	103
5.4.3	Conclusion	119
5.5	Vibrational Energy Redistribution in a DTE-BODIPY System . . .	123
5.5.1	Electronic Structure Calculations	125
5.5.2	Model System	128
5.5.3	Quantum Dynamics	132
5.5.4	Conclusion	138
6	Concluding Remarks and Outlook	143
	Bibliography	149
	Publication List	163
	Statutory declaration	166

List of Figures

1	Principle of functional materials.	9
2	Exciton models.	18
3	Electron transfer process in photosynthesis.	20
4	Different types of solar cells.	21
5	Illustration of EET theories.	23
6	Band diagram of a solar cell.	24
7	Different steps of the solar energy conversion process.	25
8	Ehrenfest dynamics program scheme.	57
9	Temperature effect on the initial Wigner sampling.	59
10	Accuracy of different integrators.	61
11	Potential matrix representation.	66
12	Adiabatic-diabatic transformation procedure.	67
13	Exciton transfer pathway in a polymeric PT system.	69
14	Exciton dynamics on a oligo-thiophene lattice after photoexcitation.	70
15	Quantum dynamical polythiophene model.	72
16	Ground and excited state structure of oligo-thiophene.	75
17	Ground and excited state BLA values of oligo-thiophene.	77
18	Transition densities of oligo-thiophene.	77
19	<i>Ab initio</i> center of mass population of oligo-thiophene.	79
20	Dependency of the excitation energy on PT chain length.	79
21	Total energies of torsional and BLA coordinate of PT octamer.	80
22	Results of the adiabatic-diabatic transformation for PT octamer.	81
23	PES of the torsional and the BLA coordinate of PT octamer.	81
24	Torsional dynamics of PT Frenkel model.	84
25	Exciton dynamics of PT Frenkel.	84
26	PT Frenkel model trapping effect.	85
27	PT CT model torsional dynamics.	86
28	PT CT model trapping effect.	87
29	<i>e-h</i> dynamics of PT CT model.	88
30	Electronic coherence of PT CT model.	89
31	PT 20-mer exciton dynamics.	91
32	PT 20-mer exciton dynamics with local coordinates.	92
33	PPV model system.	99
34	Potential energy surfaces of PPV octamer.	101

35	Schematic PPV polymer representation.	103
36	Ehrenfest convergence.	105
37	PPV hexamer expectation values.	106
38	PPV hexamer state population.	107
39	PPV Frenkel state population for TDH, MCTDH, Ehrenfest.	108
40	PPV wave function ansatz vs. density ansatz.	110
41	PPV dissipative dynamics.	111
42	Analysis of different Langevin implementations.	113
43	Effect of noise and disorder on EET in PPV.	115
44	PPV exciton trapping effect at 1 K.	117
45	PPV exciton trapping effect at 100 K.	118
46	Concept of DTE-BODIPY system.	123
47	Ring-opening reaction of DTE-BODIPY system.	124
48	Exp. DTE-BODIPY results.	125
49	Ground and excited state DTE-BODIPY structure.	126
50	Theoretical energy shift ΔE_i	127
51	DTE-BODIPY normal modes of interest.	127
52	Mapping of DTE-BODIPY structure to quantum dynamical model.	128
53	DTE-BODIPY fragment based spectral density.	130
54	DTE-BODIPY fragment to normal mode transformation.	131
55	Effect of local mode coupling on DTE-BODIPY dynamics.	134
56	Local mode energy in DTE-BODIPY system.	134
57	Effect of inter-molecular coupling on DTE-BODIPY dynamics.	135
58	Effect of dissipative environment on DTE-BODIPY dynamics.	136
59	Comparison of experimental and theoretical DTE-BODIPY results.	137

List of Tables

1	Oligo-thiophene bond length values.	76
2	Oligo-thiophene excitation energies.	78
3	Parameter of functional form of PT torsional coordinate.	82
4	Parameter of functional form of PT BLA coordinate.	82
5	Parameter of functional form of PPV torsional coordinate.	102
6	Parameter of functional form of PPV BLA coordinate.	102
7	Parameters of the DTE-BODIPY model Hamiltonian.	132

1 | Deutsche Zusammenfassung

Photoinduzierte Energietransferprozesse und -reaktionen spielen in vielen Gebieten von Chemie, Physik und Biologie eine wichtige Rolle. Zu den prominentesten Beispielen zählen der Lichtsammelprozess in der Photosynthese und der Anregungsenergietransfer in funktionellen Materialien.

Der Fokus dieser Arbeit liegt auf letzterem Bereich, genauer auf organischer Elektronik und flexiblen Donor-Akzeptor Bausteinen und Schaltern. Speziell wurden die folgenden zwei Typen von funktionellen organischen Systemen untersucht: zum einen organische halbleitende Oligomer-Fragmente wie Oligo-*p*-Phenylene-Vinylene (OPV) und Oligo-Thiophen (OT) und zum anderen kleine funktionelle Donor-Akzeptor Einheiten wie Dithienylethen-Bordipyrrromethen (DTE-BODIPY). Letzteres wurde in Kooperation mit den experimentellen Gruppen von K. Rück-Braun (TU Berlin) und J. Wachtveitl (Goethe Universität) untersucht.

Um die relevanten Energietransfermechanismen nach einer Photoanregung genauer zu verstehen, wurden an diesen Systemen elektronische und quantendynamische Untersuchungen durchgeführt. Hierzu wurden mittels *ab initio*-Methoden Hamiltonians parametrisiert und mit hochdimensionalen quantendynamischen oder semiklassischen Methoden kombiniert. Während die Parametrisierung für kleinere Fragmente durchgeführt wurde, lässt sich der parametrisierte Hamiltonian ohne Weiteres auf größere Systeme erweitern. Um kohärente Phänomene auf ultrakurzen Zeitskalen korrekt zu erfassen, wurden die dynamischen Studien mittels der Multi-konfigurationellen Zeitabhängigen Hartree (MCTDH)-Methode durchgeführt, welche eine vollständige quantendynamische Beschreibung des Systems inklusive einer korrekten Beschreibung kohärenter Prozesse darstellt. Für größere Systeme wurde die semiklassische Ehrenfest-Methode in Verbindung mit dem Langevin-Ansatz zur Beschreibung von Umgebungseffekten genutzt. In diesem Zusammenhang wurde eigens für diese Untersuchungen ein FORTRAN 90-Computercode entwickelt. Im Gegensatz zu einer vollständigen quantendynamischen Beschreibung mittels MCTDH ist die Ehrenfest-Methode als Mean-Field-Methode aufgrund fehlender Korrelationen nicht in der Lage, Kohärenzeffekte korrekt wiederzugeben. Allerdings erlaubt die Ehrenfest-Methode eine Simulation der Dynamik auf einer Zeitskala von 10-100 Pikosekunden und in Kombination mit dem Langevin-Ansatz eine explizite Beschreibung der Temperatur.

Im Falle der OT- und OPV-Oligomere wurde die Dynamik der elektronischen Anregung (Exzitonen) bei Vorliegen eines strukturellen Defekts untersucht. Ziel war es

dabei, die durch die Photoanregung induzierten dynamischen Phänomene zu analysieren. Insbesondere wurde untersucht, ob das Konzept von „spektroskopischen Einheiten“, welche die Lokalisierung der Anregung durch strukturelle Defekte beschreibt, in diesen Systemen zutrifft. Typischerweise liegt die Delokalisierungslänge der Anregung bei 5-15 Monomereinheiten. Der hierzu genutzte Hamiltonian beschreibt das zu untersuchende Polymersystem in einer Elektron-Loch-Basis, welche es erlaubt, die elektronische Dynamik in eine monomerbasierte Darstellung zu übersetzen. Im einfachsten Fall wird der Hamiltonian in einer Frenkel-Basis beschrieben, die ein auf einem Monomer lokalisiertes Elektron-Loch Paar beschreibt. Die räumliche Ausdehnung der Anregung kann nun über eine Superposition dieser Zustände beschrieben werden. Diese Elektron-Loch-Basis lässt sich jedoch auch unter Einbeziehung von Ladungstransferzuständen in eine verallgemeinerte Basis überführen, welche eine Separation des Elektron-Loch-Paares erlaubt. Des Weiteren beinhaltet das Modell eine koordinatenabhängige Kopplung dieser Zustände sowie eine generelle Beschreibung von für die Exzitodynamik ausschlaggebenden Koordinaten. Hierbei wurden niederfrequente Torsionsmoden sowie hochfrequente Bindungsmoden (auch alternierende Bindungslängen oder BLA genannt) zwischen den Monomereinheiten berücksichtigt, da diese Koordinaten einen großen Einfluss auf den Überlapp des π -Systems der Polymere haben. Die Parametrisierung dieser Koordinaten erfolgte über eindimensionale Potentialschnitte, welche mittels der Algebraischen Diagrammatischen Konstruktions (ADC(2))-Methode berechnet wurden. Um dissipative Effekte, etwa durch Umgebungsmoden, zu berücksichtigen, wurde in der quantendynamischen Beschreibung das Caldeira-Leggett Modell genutzt. Im semiklassischen Fall erfolgte diese Beschreibung mittels des Langevin-Ansatzes.

Bei den untersuchten Systemen handelt es sich um kleine Fragmente aus einer PPV- oder PT-Kette, wobei der Fokus der Arbeit auf der Exzitodynamik innerhalb dieser Ketten liegt. Diese Fragmente bieten die Möglichkeit, die Exzitodynamik mittels akkurater, multikonfigurationeller Methoden theoretisch zu studieren.

Der hier entwickelte Hamiltonian beinhaltet wie bereits erwähnt verschiedene, für die Dynamik wichtige Koordinaten und wurde für das jeweilige System anhand berechneter Potentialschnitte parametrisiert. Da der Hamiltonian elektronisch angeregte Zustände beinhaltet, wurde die auf eine genaue Beschreibung angeregter Zustände entwickelte ADC(2)-Methode genutzt. Diese Analyse bestätigt, dass die Frenkel-Zustände als *particle-in-a-box*-Eigenzustände beschrieben werden können, wobei der niedrigste Frenkel-Zustand auch gleichzeitig der niedrigste, knotenfreie *particle-in-a-box*-Eigenzustand ist. Diese Zustände weisen einen ausgeprägten

Diagonalcharakter bezüglich der Elektron-Loch-Basis auf. Alle weiteren Frenkel-Zustände können zudem über die Anzahl der Knoten identifiziert werden. Dagegen besitzen Ladungs-Transfer-Zustände einen ausgeprägten außerdiagonalen Anteil. Zur Verwendung der Potentialkurven für die folgenden quantendynamischen Berechnungen wurden diese mittels eines eigens hierfür entwickelten Transformationsverfahrens in eine diabatische Darstellung überführt. Anschließend wurden diese Potentialschnitte an analytische Funktionen gefittet.

Basierend auf dem beschriebenen Hamiltonian und den über die Transformation der *ab initio*-Potentialflächen erhaltenen funktionellen Darstellungen wurden quantendynamische Simulationen mittels der MCTDH-Methode durchgeführt. Ziel dieser Simulationen war es, die Exziton- und Kerndynamik (bzw. die Dynamik des Freiheitsgrades) nach einer Photoanregung bei Vorliegen eines strukturellen Defekts in der Mitte der Polymerkette zu untersuchen. Da die quantendynamischen Methoden numerisch aufwendig sind und als Funktion der Systemgröße exponentiell skalieren, wurde die OPV- und OT-Systemgröße auf eine Hexamer- sowie eine 20-mer-Oligomerkette beschränkt. Mit Hilfe dieses Systems ist man jedoch schon in der Lage, Erkenntnisse über die Exzitondynamik nach einer Photoanregung zu gewinnen. Des Weiteren ist das 20-mer groß genug, um die typische Delokalisierungslänge der Anregung auf 5-15 Monomeren wiederzugeben.

Im Falle des PT-Systems konnte gezeigt werden, dass die exzitonische Dynamik ausgehend von einem Subfragment auf einer sub-Pikosekunden-Zeitskala abläuft. Hierbei verteilt sich das anfangs kompakte Exziton auf das gesamte Polymer und bildet nach ca. 700 fs einen quasi-stationären Zustand, welcher die höchste Population in der Mitte der Kette aufweist, während die Population nach außen hin abnimmt. Dieser Zustand ist direkt vergleichbar mit dem Frenkelzustand niedrigster Energie, der durch Geometrieoptimierung aus den *ab initio* Berechnungen erhalten wurde. Dieser Zustand kann ebenfalls über einen relaxierten, knotenfreien *particle-in-a-box* Eigenzustand beschrieben werden. Dieses Verhalten zeigt, dass das untersuchte Oligomer als J-Aggregat betrachtet werden kann.

Des Weiteren konnte gezeigt werden, dass die beobachtete Exzitondynamik eine starke Korrelation zur Kerngeometrie aufweist. So konnte gezeigt werden, dass ein in unmittelbarer Nähe eines Torsionsdefektes lokalisiertes Exziton sich innerhalb von ≈ 250 fs über das gesamte Gitter ausdehnt, während die Torsion innerhalb von ≈ 750 fs planarisiert.

Die Simulationen an einem 20-mer zeigen darüber hinaus, dass ein weiter vom Torsionsdefekt entferntes Exziton eine ultraschnelle „Hopping“-artige Migrationsdynamik aufweist. In beiden Fällen treten kohärente transiente Effekte auf. Nach

ca. 500 fs wird ein quasi-stationärer Zustand erreicht, welcher als „getrapptes“ Exziton-Polaron bezeichnet wird. Der Trapping-Effekt wird in erster Linie durch die BLA- Koordinaten hervorgerufen. In diesem quasi-stationären Zustand sind die Bindungslängen in der Mitte der Kette deutlich verkürzt, während die Bindungslänge zum Rand der Kette hin wieder zunimmt. Wie bereits erwähnt deckt sich diese Beobachtung mit quantenchemischen Ergebnissen.

Die für das OPT-System erzielten Ergebnisse ließen sich, abgesehen von geringfügigen Abweichungen, direkt auf das OPV-System übertragen. Dies weist darauf hin, dass die beschriebenen Mechanismen in diesen System ähnlich und auch allgemeingültig sind.

Anhand der MCTDH-Methode können zwar die Elementarschritte der Exzitonodynamik untersucht werden, aber längere Zeitskalen und der Einfluss thermischer Fluktuationen sind nur bedingt zugänglich. Daher wurde die gemischt quantenklassische Ehrenfest-Methode implementiert und auf größere Systeme angewendet. Des Weiteren sollte untersucht werden, ob diese approximative Methode in der Lage ist, die exakte Referenzdynamik der MCTDH-Methode wiederzugeben.

Die Idee hierbei ist, die Wellenpaketdynamik mittels vieler unabhängiger Einzeltrajektorien abzubilden. Basierend auf dem Ehrenfest-Theorem, welches die Dynamik der quantendynamischen Erwartungswerten mit den klassischen Bewegungsgleichungen verbindet, konnte somit die Exzitonodynamik für größere Systeme analysiert werden. Des Weiteren können Dissipations- und Temperatureffekte mittels des Langevin-Ansatzes explizit beschrieben werden. Hierzu wurde ein auf diesen Anwendungszweck ausgelegtes FORTRAN 90-Programm geschrieben, anhand dessen eine Ehrenfestpropagation durchgeführt wird.

Die durchgeführten Vergleichsrechnungen zeigen, dass die Ehrenfest-Methode qualitativ in der Lage ist, die exzitonische und Kerndynamik der MCTDH-Simulation korrekt wiederzugeben. So war die Übereinstimmung der Exzitonodynamik speziell für Zeitskalen oberhalb einer Pikosekunde und den damit verbundenen quasi-stationären Zustand sehr gut. Auch die Übereinstimmung der Torsions- und BLA-Dynamik zeigte nur geringe Abweichungen. Allerdings konnte auch beobachtet werden, dass die zeitliche Auflösung der Exzitonodynamik, speziell auf der ultrakurzen Zeitskala bis zu 300 fs, nicht an die räumliche und zeitliche Auflösung der wellenfunktionsbasierten MCTDH Methode herankommt. Dies konnte jedoch aufgrund des Mean-Field-Charakters der Methode und den damit fehlenden Korrelationen auch nicht unbedingt erwartet werden.

Basierend auf diesen Ergebnissen wurde die Exzitonodynamik eines OPV-20-mers in Hinsicht auf den Einfluss von Temperatur und Geometrie untersucht. So konnte

gezeigt werden, dass die Exzitondynamik maßgeblich durch die Temperatur beeinflusst wird. Dies zeigt sich vor allem bei sehr niedrigen Temperaturen, bei denen ein kompaktes „Trapping“ des Exzitons in der Mitte der Polymerkette auf einer längeren Zeitskala beobachtet werden konnte. Dieser „Trapping“-Effekt ist allerdings unabhängig von der strukturellen Anfangsdeformation des Polymers und lässt sich auf die konzertierte Dynamik der hochfrequenten BLA-Koordinaten und der niederfrequenten Torsionskoordinaten zurückführen. Diese generieren ein energetisches Minimum, welches bei tiefen Temperaturen nur geringfügig verändert wird, da die thermischen Fluktuationen sehr eingeschränkt sind. Mit steigender Temperatur werden jedoch die thermischen Fluktuationen der Kernfreiheitsgrade ausgeprägter und eine kompakte „Hopping“-artige Exzitonpropagation in der Oligomerkette ist beobachtbar. Diese Dynamik lässt sich durch fluktuationsbedingte Übergänge zwischen lokalen Minima erklären, die im Wesentlichen durch starke geometrische Änderung der Torsionskoordinaten zustande kommen. Eine genauere Analyse zeigt, dass durch die erhöhte Temperatur die Torsionsdynamik innerhalb der gesamten Kette deutlich beeinflusst wird und sich so ein zeitabhängiger „minimum energy path“ über das gesamte Polymer ausbildet, der die Exzitondynamik maßgeblich beeinflusst. Eine weitere Erhöhung der Temperatur führt nun dazu, dass die Torsionsdynamik noch weiter verstärkt wird, was allerdings den zuvor klar definierten „minimum energy path“ zerstört. Dies spiegelt sich in der Exzitondynamik wider, welche sich bei hohen Temperaturen als sehr diffus erweist.

Im zweiten Anwendungsteil dieser Arbeit wurde der Einfluss von molekularen Schwingungen auf Dynamik in den elektronisch angeregten Zuständen einer DTE-BODIPY-Dyade theoretisch untersucht. Wie bereits erwähnt, wurde dieses Projekt parallel zu spektroskopischen Untersuchungen der Wachtveitl-Gruppe durchgeführt.

Das DTE-BODIPY-Molekül besteht aus einem Dithienylethen (DTE)-Photoschalter, welcher kovalent an ein Bordipyrrromethan (BODIPY)-Molekül gebunden ist. Mit Hilfe von UV-Licht bzw. sichtbarem Licht kann der DTE-Schalter sehr selektiv zwischen einer offenen und geschlossenen Form geschaltet werden. In Femtosekundenzeitaufgelösten Anreg/Abtast-Experimenten wurden nun nach einer selektiven Anregung des DTE-Fragments Schwingungen des BODIPY-Fragments detektiert. Mit Hilfe einer theoretischen Analyse, basierend auf TDDFT-Rechnungen, konnten diese Oszillationen eindeutig Normalmoden des Systems zugewiesen werden. Bemerkenswert hierbei ist allerdings, dass die experimentell beobachteten Schwingungen dem BODIPY-Fragment des Moleküls zugewiesen werden können, obwohl eine selektive Photoanregung des DTE Fragments induziert wurde und beide Fragmente

elektronisch entkoppelt sind. Gestützt durch die theoretische Analyse und die Visualisierung der berechneten Normalmoden kann diese Beobachtung anschaulich dadurch erklärt werden, dass die Photoanregung des DTE eine Planarisierung des DTE-Fragments nach sich zieht, welche mechanisch Energie auf das BODIPY überträgt und so die beobachteten Schwingungen induziert. Um ein besseres Verständnis des Mechanismus zu erhalten, wurde ein Modell der DTE-BODIPY-Dyade mit Blick auf eine quantendynamische Beschreibung entwickelt, welche darauf abzielt, den Einfluss verschiedener inter- und intra-molekularer Wechselwirkungen auf die Dynamik zu studieren. Dieses Modell beschreibt das DTE- und BODIPY-Fragment über gekoppelte harmonische Oszillatoren, welche anhand von TDDFT-Rechnungen parametrisiert wurden. Um den Franck-Condon-Punkt im angeregten Zustand und den folgenden Relaxationsprozess korrekt zu beschreiben, beinhaltet das Modell zusätzlich ein Reservoir an lokalen DTE-Moden. Diese Moden werden während der Photoanregung stark angeregt und spielen eine wesentliche Rolle in der Transferdynamik.

In der quantendynamischen Untersuchung konnte gezeigt werden, dass der durch die Photoanregung induzierte Energietransfer vom DTE- zum BODIPY-Fragment stark durch die Kopplung an die während der Photoanregung involvierten Normalmoden beeinflusst wird. Unabhängig von der Stärke der Kopplung zeigt sich aber auch, dass die Energietransferdynamik auf einer Zeitskala von ≈ 1.0 ps stattfindet, was in guter Übereinstimmung mit experimentellen Daten ist. Des Weiteren konnte gezeigt werden, dass Umgebungseffekte den Energietransfer ebenfalls stark beeinflussen, während die Kopplung zwischen DTE und BODIPY nur einen Einfluss auf die Frequenz des Transfers und nicht auf die Amplitude der Energie hat. Ein direkter Vergleich zwischen den quantendynamischen Studien und den experimentellen Daten zeigt zudem, dass das genutzte Modell vor allem auf einer Zeitskala bis zu ≈ 250 fs eine sehr gute Übereinstimmung mit den experimentellen Daten aufweist. Auch die Beschreibung eines stationären Zustandes auf einer längeren Zeitskala wird korrekt wiedergegeben.

Zusammenfassend lässt sich sagen, dass Energietransferphänomene in zwei sehr unterschiedlichen Systemklassen anhand von Modell-Hamiltonians und hochdimensionaler Quantendynamik studiert werden konnten. Des Weiteren zeigt der Vergleich mit der semiklassischen Ehrenfest-/Langevin-Methode, dass eine Schnittstelle zwischen der exakten quantendynamischen und semiklassischen Behandlung sinnvoll definiert werden kann und die Behandlung größerer Systeme und längerer Zeitskalen ermöglicht.

2 | Introduction

One of the most important processes in nature involving efficient energy transfer is the photosynthetic process in plants [1, 2]. This process has been perfectly optimized over about a billion years. Therefore, much work is in progress to mimic the energy transfer process of photosynthesis by developing functional materials which can be used, e.g., for optoelectronic devices.

In the middle of the 20th century, the first optoelectronic devices, e.g., solar cells, based on silicon were developed. These devices allow to convert solar energy into electric energy [3]. The efficiency of the first solar cells was below 2%, whereas by now, efficiency has been increased to $\approx 19\text{--}22\%$ for commercially available solar cells [4] (the record of a proof-of-principle device is $\approx 45\%$ [4]). However, silicon-based solar cells have the disadvantage that already a small amount of impurities can reduce the efficiency drastically [5].

An alternative to silicon-based optoelectronic devices are new types of devices based on functional organic materials, e.g., organic polymers [6–8] or small functional donor-acceptor systems. Beyond optoelectronics, many applications exist for optically excited organic building blocks, e.g., organic light emitting diodes [9, 10] or photocontrolled switches.

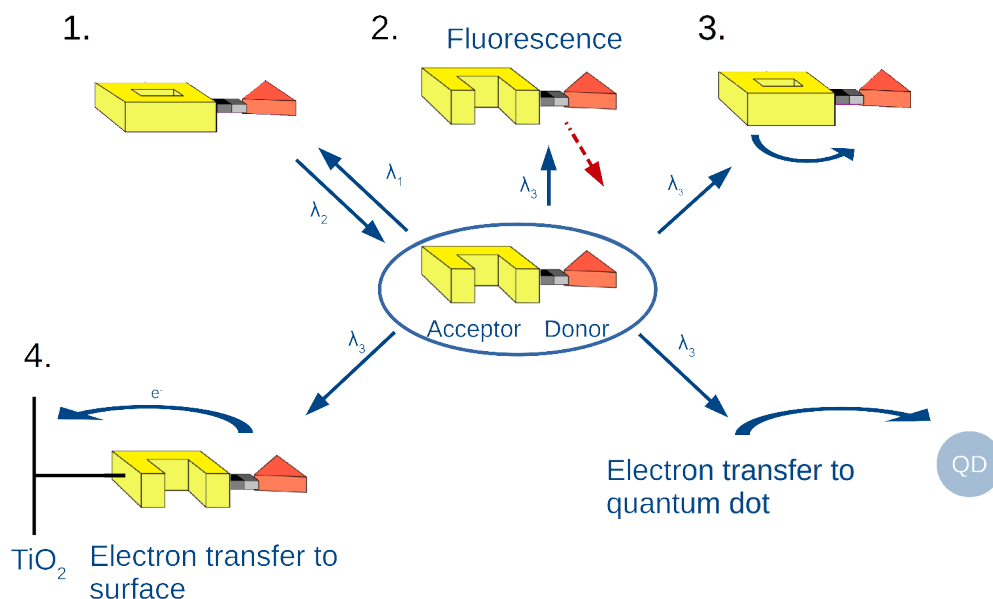


Figure 1: Illustration of different applications of a new type of donor-acceptor based functional material. The system state can be switched by light with different wavelengths resulting in different reaction pathways [11].

As shown in Fig.1, the functionality of typical donor-acceptor type systems is extremely variable and can be controlled by different excitation wavelengths. These properties can be used to trigger exactly defined states, e.g., „on“ or „off“ states and state dependent reactions.

One of the most important processes in these systems is excitation energy transfer (EET). Traditionally, EET is described by Förster theory [12] which, however, cannot capture ultrafast, coherent EET dynamics. Hence, much work is in progress on the experimental and theoretical side to elucidate the details of the EET mechanism for various chemical, material and biological systems. Especially the coherence time of the EET process is of interest, since for some systems, e.g., photosynthetic systems, a comparatively long coherence life time is observed [13]. The work of this thesis will focus on the elementary EET processes on an ultrafast time scale (sub-ps) in the following systems:

- (i) EET dynamics in an oligothiophene (OT) type system using a full quantum dynamical description.
- (ii) EET in an oligo-*p*-phenylene vinylene (OPV) type system depending on thermal noise and structural disorder using semi-classical and multiconfigurational methods.
- (iii) Photoinduced intra-molecular vibrational energy redistribution (IVR) processes in an electronically decoupled dithienylethene-boron-dipyrromethene (DTE-BODIPY) dyad.

These energy transfer processes taking place on an ultrafast time scale are of special interest, since the dynamics is expected to be at the border between a coherent and non-coherent („hopping-type“) process. Furthermore, the competition of different coupling mechanisms in the EET and IVR processes will be studied. In general, the work on these topics can help to understand the elementary transfer processes in such complex environments as biological and material systems.

To capture the coherent nature of the relevant processes on an ultrafast time scale, high dimensional quantum dynamical methods have to be used. In particular, highly efficient multiconfigurational methods have been developed over the last 25 years, namely the Multiconfiguration Time-Dependent Hartree method [14, 15]. This method alleviates the exponential scaling problem that makes quantum dynamics in many dimensions a challenging task.

Organic polymers are increasingly used as new component materials for the development for optoelectronic devices. Up to now, organic semi-conducting polymer

based solar cells have reached efficiencies up to 11% [7] as compared to about 20% for perovskite based solar cells [16, 17]. Due to EU regulations, it is more likely that organic polymer based solar cells or small functional donor-acceptor systems will be used for commercial applications.

Many experimental investigations are carried out in order to understand the photoinduced energy transfer processes in these materials [18–24]. In parallel, various theoretical models have been developed to simulate EET on different time scales. Overall, the EET mechanism in these materials is complex and depends on a number of aspects including (i) structural properties, (ii) electronic properties and (iii) electronic-vibrational (vibronic) coupling effects. In general, the structure of a polymer can contain ordered and disordered domains and can be controlled during the production process. Depending on the amorphous or regio-regular nature of the material at the nano-scale, an intra- or inter-molecular EET within the polymer chains can be dominant [25–28]. The resulting main pathway also depends on the electronic properties of the polymer, which are in turn influenced by the structure [29–31]. Depending on the structure and additives, the band-gap between valence and conduction band can be tuned, which directly effects the conductivity of the polymer. But also structural aspects, like defects in the polymer backbone, can influence EET; especially the intra-molecular transfer is affected by these defects [32, 33]. Furthermore, temperature has a very strong effect on the transfer dynamics in these systems [21, 33–35].

Using theoretical methods and models, new prospects are created to investigate the EET dynamics in these types of systems and help to understand the mechanism for efficient EET. Depending on the model and the approach, different aspects in the conversion process can be revealed but it is challenging to capture the complete process. Therefore, new techniques have to be developed to increase the system size accessible to the model and also the time scale under study.

Besides the photoinduced EET in semi-conducting polymers, similar transfer processes have been investigated for small functional organic donor-acceptor systems like dithienylethene-boron-dipyrromethene (DTE-BODIPY). The experimental observations indicate a molecular energy redistribution after photoexcitation via coupled molecular vibrational modes, similar to the vibronic contributions of the energy transfer in semi-conducting polymers [36–40]. As illustrated in Fig.1, these materials use light as a trigger to switch the system between different states with different properties. The requirements for these materials are: (i) selective excitation wavelengths, (ii) high efficiency, (iii) reversibility and (iv) low photobleaching. A promising material fulfilling these requirements is the above-mentioned

electronically decoupled DTE-BODIPY dyad, which has been developed by the group of K. Rück-Braun (TU Berlin) [11, 41, 42] and investigated by time-resolved pump-probe experiments in the group of J. Wachtveitl (Goethe University) [42]. Interestingly, the photodynamics of this system indicates that the IVR process takes place on a sub-ps time scale [42].

To describe the dynamics of these systems, the following strategy is employed: first-principles parametrized model Hamiltonian is constructed, using *ab initio* methods, and subsequently combined with a high-dimensional quantum description of the dynamics. The Hamiltonian comprises electronic and vibronic contributions, and dissipative effects are included as well (either by explicitly including many vibrational modes or by introducing a Langevin dynamics). One of the most challenging aspects of the theoretical description is the appropriate choice of the electronic structure methods and the model Hamiltonian describing the dynamics of the system. For the most part, high-level *ab initio* methods like the Algebraic Diagrammatic Construction (ADC(2)) scheme are used. On the quantum dynamics side, methods are needed that are capable to propagate tens or hundreds of modes on many non-adiabatically coupled potential surfaces. Therefore, we employed the above mentioned multiconfigurational techniques of the MCTDH class.

With this setup, the exciton dynamics in a PT or PPV oligomer system can be studied. In projects (i) and (ii), exciton dynamics in a Frenkel-type basis for PT and PPV on a minimal lattice is studied using the MCTDH method combined with an accurate parametrization. The model focuses on the effect of steric defects, such as torsional deformations of the polymer backbone, on the exciton dynamics. Furthermore, the effects of thermal noise and disorder are considered using the semi-classical Ehrenfest approach. This approach allows an explicit description of temperature and the treatment of larger model systems, which are needed to investigate the exciton dynamics in a more realistic setting. A FORTRAN 90 program was written to implement specifically an Ehrenfest/Langevin treatment for oligomer type systems. Furthermore, the „spectroscopic unit“ concept [43] is investigated using a larger PT system combined with the more powerful multilayer (ML) version of MCTDH [15].

In project (iii), the experimental observations of oscillatory signals in the photodynamics of a DTE-BODIPY dyad are described theoretically. To this end, we employ electronic structure calculations along with a normal mode decomposition, which is complemented by a transformation of normal modes into a local mode picture. This is performed by using results obtained from TDDFT calculations.

Furthermore, the system is mapped to an appropriate model Hamiltonian representing the system and the IVR process after photoexcitation in terms of the competition between intra- and inter-molecular coupling values.

The thesis is structured as following: (i) a review of the general energy transfer concepts and the theoretical methods will be given in Chp.3 and 4, (ii) computational aspects of the implementation of the Ehrenfest method are given in Chp.5.1, (iii) the exact adiabatic-diabatic mapping procedure is presented in Chp.5.2, (iv) the results for the investigation of the exciton dynamics in PT and PPV are presented in Chp.5.3 and 5.4, (v) the investigation of the IVR process in a DTE-BODIPY dyad is presented in Chp.5.5. Finally, some concluding remarks and a outlook are given in Chp.6.

Theoretical Background and Methods

3 | Theoretical Background

In this Chapter, a general overview over the most important mechanisms and models for energy transfer processes in organic and inorganic materials is presented. Furthermore, a brief introduction to semi-conducting systems and their application will be given.

This chapter is structured as follows: (i) a general introduction to energy transfer processes, (ii) an introduction to the theory of semi-conducting materials and, (iii) an overview over different models to describe the energy transfer dynamics in these materials. A detailed introduction of the particular systems will be given in Chap.5.

3.1 Models for Energy Transfer Processes in Inorganic and Organic Systems

The theoretical and experimental description of energy transfer processes is a field of intensive research in many groups around the world. Several groups, experimental and theoretical, are working on the description of the key steps of photo-induced excitation energy transfer (EET) in inorganic and organic materials [22, 44, 45].

In addition to EET, which is a pure electronic process, the intramolecular vibrational energy redistribution (IVR) is an additional important mechanism in several systems. In general, energy transfer processes can be found in a broad type of systems from light-harvesting systems of plants to semi-conducting polymers. In an one-electron picture, the description of EET is based on the assumption that an electron located in the electronic ground state is excited to a specific state (known as Franck-Condon excitation) upon irradiation by light. The electron in the excited state and the following dynamical process can be described by several models, depending on the localization of the electron and the „hole“ that is left behind in the ground-state configuration. The electron and the corresponding hole are often called *electron-hole pair* or *e-h pair*. In the following sections, the *e-h pair* is also considered as a quasi-particle that is called *exciton*. A characteristic quantity is the *e-h separation*, denoted coherence size Δ_{eh} . This quantity is to be distinguished from the delocalization length that describes the spatial extension of the exciton. Assuming an arbitrary system with a definite size, three different kinds of excitons are encountered, depending upon the material under investigation:

- Frenkel exciton: e - h pair well localized, no static el. dipole, coherence size $\Delta_{eh} = 0$
- Wannier-Mott exciton: e - h pair delocalized, no static el. dipole, coherence size $\Delta_{eh} \neq 0$
- Charge-transfer exciton: e - h pair separated, static el. dipole, coherence size $\Delta_{eh} \neq 0$

A Frenkel exciton [46] is typically found in molecular systems with a low dielectric constant which leads to a strong Coulomb interaction between electron and hole (the typical coupling strength is of the order of 0.1 - 1.0 eV). In case of larger systems e.g. in photosystems, a Frenkel exciton can be spatially located on a small part of the system e.g. an aromatic system or in case of a polymeric system on a monomer unit. The position and the spatial extent of the exciton can be calculated by theoretical approaches or determined experimentally. Typically, a Frenkel exciton is localized in a radius up to ≈ 1.0 nm, in case of organic polymeric systems on 1 monomer unit. The delocalization length of a Frenkel exciton over several monomer units is related to a superposition of localized e - h pairs, whereas the coherence size is 0. In terms of an e - h basis, the delocalization length can be described by the diagonal contributions and the coherence size by the off-diagonal contribution.

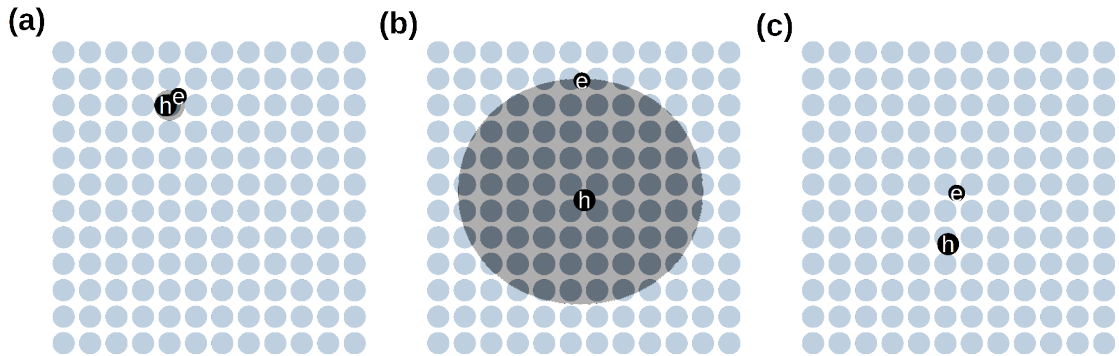


Figure 2: Schematic representation of different exciton models on a lattice (blue) (a) Frenkel exciton located on one monomer unit (b) Wannier Mott exciton delocalized over several monomer units and (c) Charge transfer exciton. The gray area indicates a bounded e - h pair.

In systems with a high dielectric constant, the Coulomb coupling between electron and hole is low, which leads to a strong delocalization of the electron-hole pair (the typical coupling strength is ≈ 0.01 eV). This type of exciton is called Wannier-Mott exciton [47] and often found in semi-conducting systems e.g quantum dots. In contrast to the Frenkel exciton, the spatial extent of the Wannier-Mott exciton

is up to 30 nm, depending on the type of system, also observable in a coherence size $\neq 0$.

In contrast to the still bound but delocalized $e-h$ pair in the Frenkel or Wannier-Mott type exciton, the charge-transfer exciton is a coulombic bounded $e-h$ pair. A charge-transfer exciton (CT) [48] is often observed in donor-acceptor type systems. To visualize the different type of exciton, a lattice can be assumed as a basis representing the different parts of a system (as shown in Fig.2). The representation shown in Fig.2 allows a mapping of a given system to this lattice, which can simplify the further analysis. As shown, the spatial extent of the Wannier-Mott exciton is much larger compared to the Frenkel or CT exciton. This fact can have a strong influence on the physical and optical properties of a system e.g the absorption properties of quantum dots. Furthermore, two elementary processes can be described using these exciton types:

- Exciton migration (energy transfer)
- Exciton dissociation (charge transfer)

Photosynthesis

One of the most studied systems by experimental and theoretical groups is the light harvesting system [2] of plants, which is essential for life on earth. The EET in light harvesting systems is an extremely complex reaction with a efficiency of $\approx 100\%$ which includes several steps carried out in several proteins [1, 44]. In this specific and unique system, nature has developed a very efficient and ultrafast mechanism to generate energy from sun light. In the so-called Z-scheme shown in Fig.3, the photoinduced charge-separation needed for the reduction of NADP^+ to NADPH is illustrated. This reduction is essential for all living organisms. In general, the first steps of the charge separation take place on a time scale of femto- to sub-pico seconds which is quite fast compared to the overall time of ≈ 500 ms for the whole photosynthetic process [49].

Even though the process of generating energy from sunlight including all steps of the reaction cycle is well known, it is still widely discussed whether this is a coherent or non-coherent process and if the coherence is essential for the high efficiency of the reaction. First experimental attempts to solve this question have been done by Fleming et al. using two-color-photon echo experiments on the Fenna-Matthew-Olsen (FMO) complex [50]. These experiments suggest that the high efficiency of the EET of the photosynthetic system is indeed a strong coherent reaction, which is strongly influenced by its environment and includes several intermediate energetic levels [51, 52].

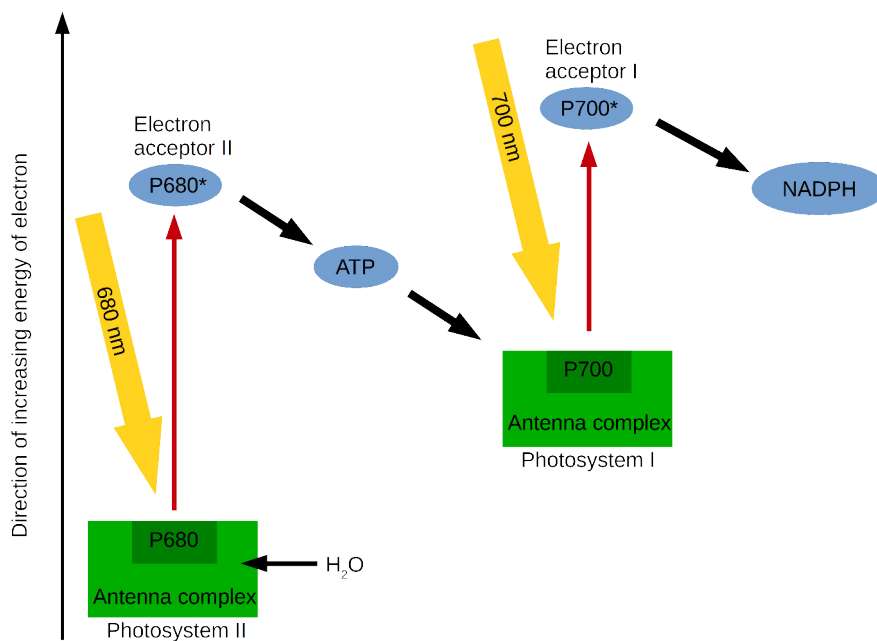


Figure 3: Schematic representation of the electron transport process in the photosynthetic process.

In addition to the experimental approaches, several theoretical studies have been done using different levels of theory e.g. a full quantum dynamical study on EET in the FMO complex [53–55]. One advantage of a theoretical description of these reactions is the high flexibility of the system setup. Using an appropriate model, several aspects, which are not accessible by experiments, can be described e.g pH dependency or different initial conditions. This helps to understand the fundamental principles and mechanism of EET which can then be used to design molecules and devices, which mimic the light-harvesting complex e.g new types of organic solar cells with a high power conversion factor. Such devices can help to reduce the amount of fossil energy resources and also offer a completely new type of applications [56–58].

Photovoltaics

The development of such molecules started with the development of inorganic solar cells by the end of the 19th century after exploring the photoelectric effect [59] by Heinrich Hertz. The photoelectric effect is the fundamental feature of any solar cell and therefore, a lot of investigations have been conducted to improve the efficiency of this effect in different materials e.g. silicon. In the 1950th, the first practical silicon-based solar cells for aerospace projects were developed by the Bell laboratories [3]. These solar cells had a poor efficiency ($\approx 6\%$) and were very costly (generation I solar cells; see lower panel of Fig.4). Due to an increase of efficiency and a better cost/Watt ratio (generation II solar cells), the world production of

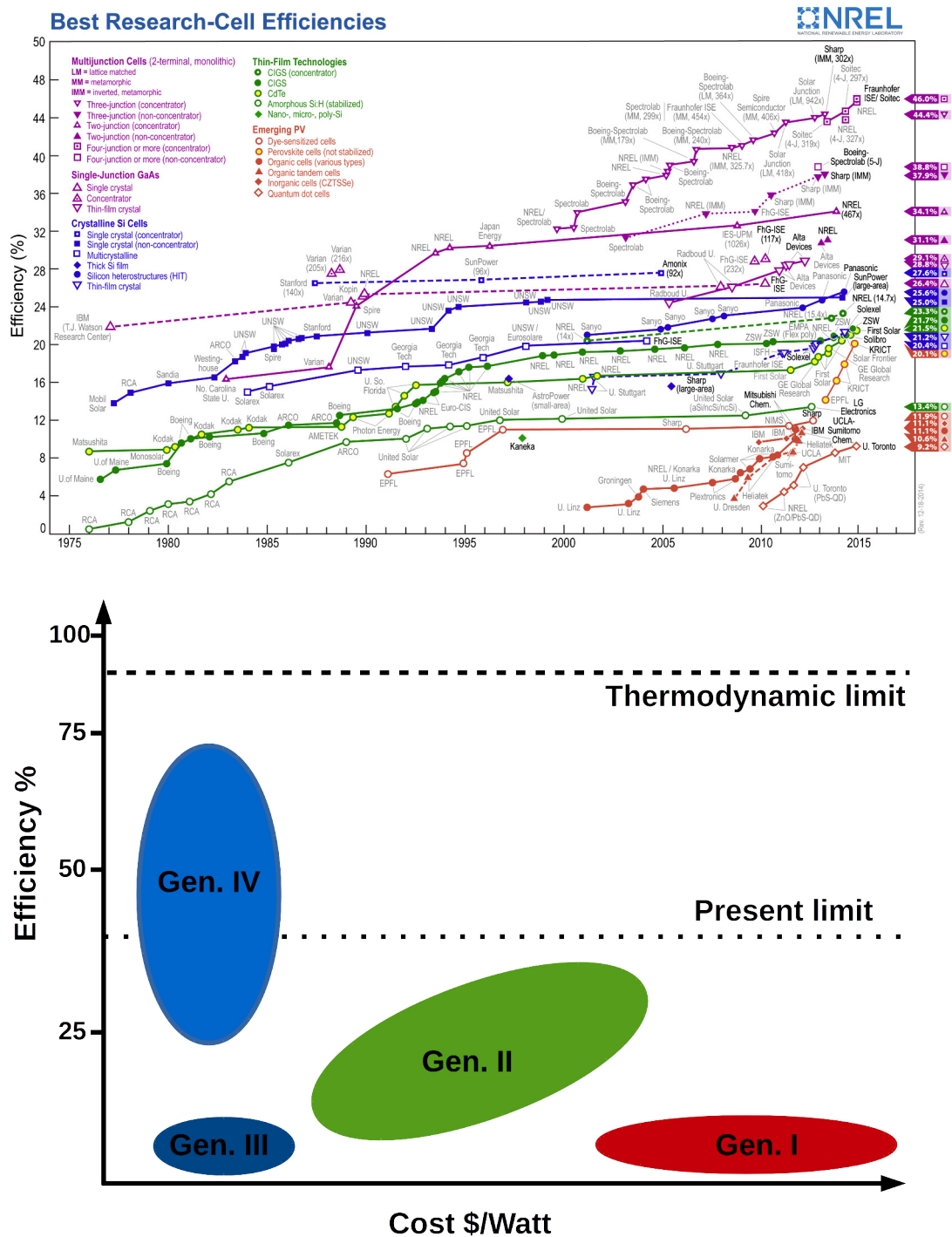


Figure 4: Overview of the development of organic solar cells. (upper panel) Development of the total efficiency of different types of solar cells (Figure taken from Ref.[4], 2015). (lower panel) Different generations of solar cells compared by efficiency and cost/watt ratio.

photovoltaic cells increased rapidly since then. These type of solar cells are still state-of-the-art solar cells (the standard efficiency of a silicon based solar-cell is $\approx 20\%$, for detailed informations on different types of solar-cells and their efficiency,

see upper panel of Fig.4). In the 1990th, the development of organic solar cells based on polymeric systems started (generation III) [7, 8]. The great advantage of these new generation of solar cells is the very easy and cheap production, and new physical properties of the material, e.g. they can be designed to have any color & shape [58, 60]. Due to these properties a huge range of applications is possible. As a proof-of-principle, ultra thin flexible LED displays or printable solar cells have been produced by several companies [9]. Up to now, the efficiency of these type of solar cells is about $\approx 12\%$ which is not sufficient for practical use, but as for generation II cells it is quite likely that the efficiency will be increased in the near future (generation IV) [6]. It is assumed that these future type solar cells might be usable for any kind of application and will help to reduce the consumption of non-regenerative fuels.

Energy Transfer Theories

Due to the ubiquitous appearance of EET and charge transfer (CT) in nature and synthetic materials, several theories have been developed over the years including different physical aspects relating to energy and charge transfer. The following rate (or kinetic) theories have been accepted by the experimental and theoretical community:

- Förster theory [61]
- Dexter theory [62]
- Marcus theory [63, 64]

For comparison, the first three theories are illustrated in Fig.5. Förster theory describes the energy transfer efficiency from a donor system to an acceptor system after photo-excitation depending on the distance of donor and acceptor, the orientation of the donor dipole and acceptor dipole and the spectral overlap of donor and acceptor. In general, the transfer rate depends on the donor acceptor distance r_{DA} by

$$k_{Förster} = k_D^{rad} \left(\frac{r_F}{r_{DA}} \right)^6 \quad (1)$$

with the Förster radius r_F . Due to the strong dependency on the radius, Förster theory can be used as a tool to measure distances in macromolecular systems. The physical origin of the energy transfer are dipole-dipole interactions. In principle, Förster theory describes the non-radiative energy transfer by assuming that an excited electron on the donor relaxes non-radiatively from the lowest excited

state S_1 to the ground state, while simultaneously an electron on the acceptor is excited. This mechanism is a one-step process. Förster theory is widely used in the experimental community, since it offers an easy and accurate method to determine intermolecular distances or transfer rates using spectroscopic methods.

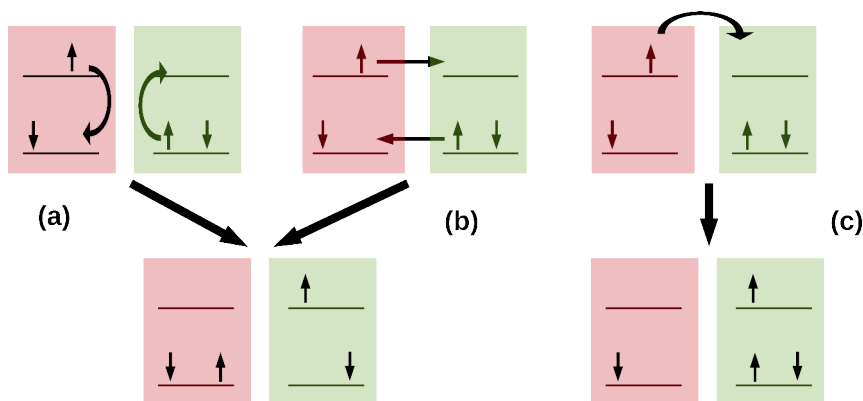


Figure 5: Comparison of different transfer theories from donor (red) to acceptor (green) for the singlet-singlet case. (a) Förster, (b) Dexter and (c) Marcus theory.

In contrast to Förster theory, Dexter theory is a theory describing the exchange efficiency of two electrons in the basis of overlapping wave functions

$$k_{ET} \propto J \exp\left[-\frac{2r}{L}\right] \quad (2)$$

$$J = \int f_D(\lambda) \epsilon_A(\lambda) \lambda^4 d\lambda \quad (3)$$

with the donor-acceptor distance r , the sum of the Van-der-Vaals radii of donor and acceptor L and the spectral overlap integral J . The spectral overlap integral J depends on the donor fluorescence spectra f_D , the acceptor absorption spectra ϵ_A and the wavelength λ . Due to the wave function overlap-based description, the typical range of Dexter transfer is up to 1 nm, whereas Förster theory describes transfer processes up to 10 nm, which is related to the dipole-dipole interactions.

In contrast to Förster and Dexter theory, which describe the non-radiative energy transfer from a donor to an acceptor, Marcus theory has been developed to describe the electron transfer occurring in e.g. redox reactions or electro-chemistry. The fundamental principles of the Marcus theory are: (i) the electron transfer process is described classically and (ii) the Franck-Condon principle is valid, which mean that the electronic transfer process is faster than the reorganization of the nuclear degrees of freedom. The electron transfer rate is defined by

$$k_{ET} = A \cdot \exp\left[-\frac{\Delta G}{RT}\right] \quad (4)$$

with the system dependent-constant A , the temperature T , the ideal gas constant R and the Gibbs energy ΔG . The Gibbs energy contains the dependency of the reorganization energy λ and is given by

$$\Delta G = \frac{(\Delta G^\circ + \lambda)^2}{4\lambda} \quad (5)$$

Besides different mechanisms of energy transfer, the time scale of these energy transfer is also important. As mentioned above, the time scale of energy transfer in organic systems like e.g. light harvesting complexes, is from several ps to ms. In contrast to such a long time scale, the time scale of energy transfer processes in organic semi-conductors is in the range of sub-ps to ns [22, 65, 66].

In the following section, the application of energy-transfer in the context of solar-cells (inorganic and organic) will be introduced.

3.2 Energy Transfer Processes in Silicon Based Solar Cells and Organic Semi-Conducting Polymers

As already mentioned, the understanding of the key steps in the light-to-energy conversion process in organic systems will help to improve the development of future devices, which mimic these process in a sufficient way. In the following section the principles of energy generation of inorganic silicon-based solar cells and organic polymeric solar cells will be introduced [67, 68].

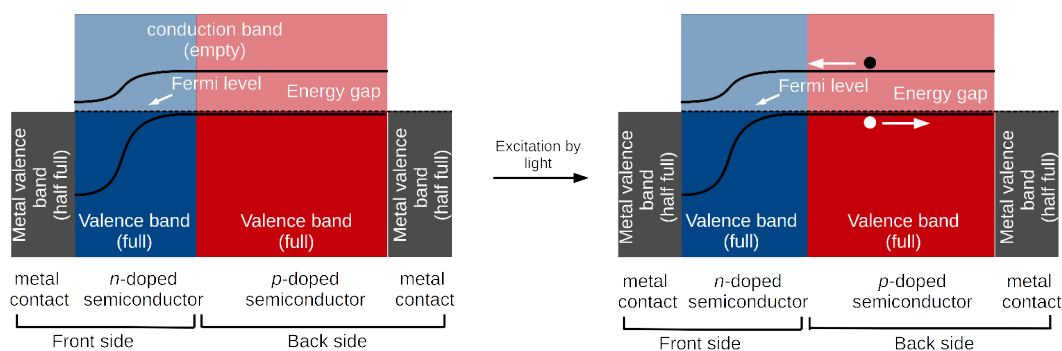


Figure 6: Band diagram of an inorganic silicon-based solar cell.

As shown in Fig.6, most modern silicon based solar cells are build by two electrodes, a negative doped part (n -doped) and a positive doped part (p -doped). A typical material for a n -doped silicon crystal is phosphorous, whereas boron is used for p -doped silicon crystals. The combination of p and n doped silicon allows an efficient solar cell, which can be explained by the fact that a n -doped material contains

'more' electrons, whereas an *p*-doped material contains 'more' holes. The resulting silicon crystals are highly ordered and already a small number of crystal defects can reduce the energy conversion efficiency drastically.

The most common way to visualize and explain the photoelectric effect and the principle of silicon-based solar cells is to use a valence and conducting band picture. As shown in Fig.6 in a simplified way, the front side of a solar cell is built by a metal contact (a very fine lattice) and the *n*-doped silicon. The *p*-doped silicon and another metal contact form the back side of the solar cell. A typical size for the *n*-doped layer is about $\approx 1 \mu\text{m}$ whereas the *p*-doped layer has a typical size of $\approx 600 \mu\text{m}$. A photoexcitation by light generates an electron-hole pair at the *p-n* interface. Due to the electric field gradient between the *n*- and *p*-layer, the electrons will be transported to the *n*-doped layer whereas the holes will be transported to the *p*-doped layer. Connecting both metal contacts, an electric current can be measured.

By optimizing the layer material and sizes, the contact material and by combining different doped layers, several different types of inorganic solar cells have been developed with a wide range of efficiency (as shown in Fig.4).

A completely different type of solar cell is based on semi-conducting polymers e.g. poly-*para*-phenylene vinylene, polythiophene or polyacetylene [69–73]. The common property of most of the semi-conducting organic polymers is a large conjugated π -system [74–77]. The principle of energy conversion by light is very similar to inorganic solar cells.

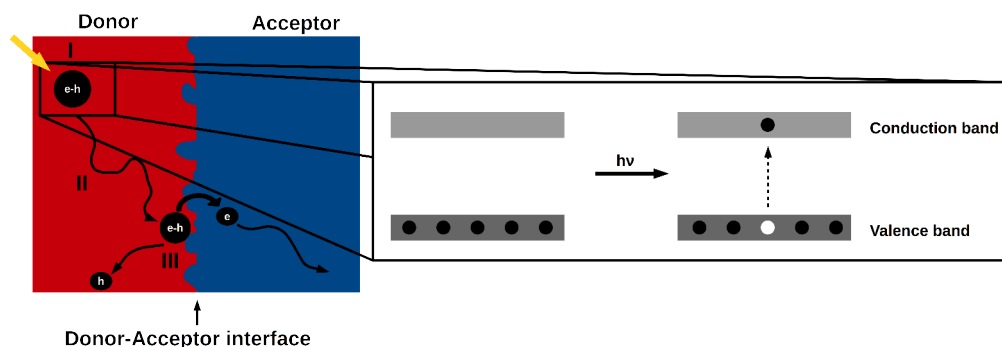


Figure 7: Steps during the energy conversion process after irradiation of a donor-acceptor (D-A) type system: (I) Exciton generation by irradiation (II) Exciton migration and (III) Charge separation at a donor-acceptor interface.

As in the inorganic case, the light-to-energy conversion in semi-conducting polymers is a complex, multi-step process, which cannot be described by a simple picture. Most of the semi-conducting polymers used for the new type of solar cells are built by a donor and an acceptor part [78–80]. As shown in Fig.7, the first and essential step in the conversion process is the absorption of a photon by the donor.

The absorption process is the elemental process to generate an electron-hole pair ($e-h$), which is needed for an energy transfer process. The absorption efficiency in these materials strongly depends on the energy gap between the valence and the conduction band [81]. For semi-conducting polymeric systems, this band-gap is mainly in the range of UV/Vis radiation and can be tuned by a controlled doping of the semi-conducting polymer with impurities or by a controlled production process of the chain length and the order/disorder of the system [60, 82–87].

In a second step, the $e-h$ pair, which can also be described in terms of a Frenkel or a Wannier-Mott exciton, starts to move from its initial position in the system. This movement is an oriented but random process, which depends on several aspects: the material itself, an external or internal gradient [78, 88] (e.g. an electric field), the local structure of the system [26, 89–91], temperature [25, 35, 78, 92] and structural defects [32, 93, 94]. All these aspects will influence the diffusion length of the exciton and therefore also the efficiency of the solar cell [87, 95, 96]. By understanding and optimizing the effect of these parameters, a strong improvement of organic photovoltaic materials can be achieved.

If the $e-h$ pair reaches the donor-acceptor hetero-junction (similar to the $n-p$ -interface), it is possible that the $e-h$ pair separates in a third step. For all steps, a recombination of the $e-h$ pair can take place, which will annihilate the excitation and therefore, it is important that the annihilation probability is low for an efficient light-to-energy conversion. The time scale of the first step is on the ultra-short fs range. This process is a Franck-Condon excitation from the electronic ground state to an excited state including the relaxation of the electronic wave function on the new excited state surface. In contrast to this ultrafast time scale, the second step can take place on a much longer time scale depending on the system and the donor-acceptor ratio and morphology. Typically, the diffusion of the $e-h$ pair takes place on a ps to sub-ns time scale. The final $e-h$ dissociation takes place on a sub-ps timescale. These different processes and their corresponding time scales have been investigated using experimental and theoretical approaches in order to get a better understanding of the mechanism behind the light-to-energy conversion.

3.3 Model Hamiltonians for Energy Transfer Processes

To study EET processes on a theoretical level, a Hamiltonian is needed to describe the physical properties of the type of energy transfer and the information about the system under study such as internal degrees of freedom, environment

or electron-phonon coupling effects. In principle, the full molecular Hamiltonian would describe the system perfectly. It is obvious that by using this Hamiltonian the computational effort is too high since it describes all physical and chemical aspects of the system explicitly. Thus approximations that restrict the description to the minimal set of DOFs are needed

$$H_{full} = H_{sys.} + H_{env.} + H_{sys.+env.} \quad (6)$$

$$H_{sys} = H_{nuc.} + H_{el.} + H_{nuc.+el.} \quad (7)$$

The first approximation is to decompose the full Hamiltonian into a sum of a system Hamiltonian $H_{sys.}$, an environmental Hamiltonian $H_{env.}$ and an interaction of both $H_{sys.+env.}$. For $H_{env.}$ several models e.g. hierarchical mode representation or a Langevin description can be used. This model also affects the interaction Hamiltonian $H_{sys.+env.}$ which couples the system to the environment e.g. a linear coupling. In contrast, the approximation of $H_{sys.}$ is essential, since on the one hand the system's properties have to be represented on a reasonable level of theory, on the other hand the computational costs should be as low as possible. By dividing this Hamiltonian into an electronic $H_{el.}$, a nuclear $H_{nuc.}$ and an interaction $H_{nuc.+el.}$ part, it is possible to approximate every term by simple expressions including e.g. only active degrees of freedom combined with an appropriate basis of the electronic wave function.

In the following, three widely used Hamiltonians for EET processes will be introduced and discussed, whereby the focus will lie on the Merrifield Hamiltonian, which has been adopted and modified in this work. A detailed description of the used model Hamiltonians including the parametrization is given in the respective sections of Chp.5. In the following list, the four Hamiltonians are listed, including references, for a more detailed description and derivation:

- Holstein Hamiltonian [97]
- Merrifield Hamiltonian [98, 99]
- Su-Schrieffer-Heeger (SSH) Hamiltonian [84, 100]

One of the first models to describe EET is the Holstein model, which was originally developed to describe electron-phonon interactions and self-trapping effects in molecular crystals in the 1950th. The general form of the Holstein Hamiltonian reads as follows

$$H_{Holstein} = -t_0 \sum_{i,j} c_i^\dagger c_j - g \sum_i c_i^\dagger c_i (a_i + a_i^\dagger) + \omega_0 \sum_i a_i^\dagger a_i \quad (8)$$

where the creation (annihilation) operator of fermions is given by c_j (c_j^\dagger), the creation (annihilation) operator of local vibrations is given by a_i (a_i^\dagger). w_0 denotes the local mode frequency, t_0 is the electron inter-site resonance integral and g denotes the electron-phonon coupling constant.

Almost parallel to the development of the Holstein type model, the Merrifield Hamiltonian was developed by R. E. Merrifield in the 1960th to describe excitons in molecular crystals including ionized states. This Hamiltonian is based on the exciton theory developed by Frenkel in 1931, which states that a photoexcitation cannot be seen as an excitation on a particular atom in a molecule or crystal, but as a 'shared' excitation of all or at least a few atoms. The general form of the Merrifield Hamiltonian is given by

$$H_{Merrifield} = \omega \sum_{\sigma} b_{\sigma}^* b_{\sigma} + \sum_k \epsilon(k) a_k^{\dagger} a_k + \gamma \omega N^{-0.5} \sum_k \sum_{\sigma} a_{k+\sigma}^* a_k (b_{\sigma} + b_{-\sigma}^{\dagger}) \quad (9)$$

with the creation (annihilation) operator b (b^\dagger) for the phonon, a (a^\dagger) for the exciton, the ground state frequency ω , the excitation energy ϵ and the electron-phonon coupling constant γ . This Hamiltonian captures the interactions between molecular degrees of freedom and excitons considering ground and excited state potentials. The wave function is expressed in terms of single excitonic states

$$\Psi = \sum_i c_i |\varphi_i\rangle \quad (10)$$

In the 1980th, the Su-Schrieffer-Heeger (SSH) Hamiltonian has been developed to describe the soliton formation in polymeric systems like *poly-acetylenes*. For a *poly-acetylene* chain with n repeating units, the SSH Hamiltonian is given by

$$H_{SSH} = - \sum_{i\sigma} t_{i+1,i} (c_{i+1,\sigma}^{\dagger} c_{i\sigma} + h.c.) + \frac{k}{2} \sum_i (u_{i+1} - u_i)^2 + \frac{m}{2} \sum_i \dot{u}_i^2 \quad (11)$$

where $t_{i+1,i} = t_0 - g(u_{i+1} - u_i)$ denotes the intersite hopping with the electron-phonon coupling constant g . c and c^\dagger denote the creation and annihilation operator. The electron spin is defined by σ , t_0 is the hopping in absence of vibrations, u_i are the coordinates (also called group displacement in the context of *poly-acetylene*), k is the force constant of the phonons and m denotes the mass of the repeating units.

The aim of all three models is the description of EET in molecular systems using an as most accurate and realistic description as possible. Nevertheless, all models have some differences, advantages and disadvantages and the main problem is not to find a good model in general, but to find a good model for the type of system

under study. The general problem of all models is an appropriate parametrization of the Hamiltonian, which can be very complicated for complex systems, especially if quantities such as electron-phonon coupling values are not easily accessible by experiments, while parameters such as frequencies can be taken from experiments or *ab initio* calculations.

The Merrifield type Hamiltonian and the Holstein Hamiltonian have been developed in the middle of the 20th century to explain photoreactions in molecular crystals. Their description is based on a molecular crystal with only a few active degrees of freedom and an appropriate basis for the wave function e.g. a Frenkel basis. While the Merrifield Hamiltonian uses a frequency representation throughout, the Holstein Hamiltonian uses an integral representation for the description of electrons, which allows a quantum description of trapping effects. Nevertheless, both types of Hamiltonians are widely used in the field of organic photovoltaics or photophysical processes in organic systems, since these models allow a simple but very intuitive description of EET processes. In contrast, the SSH Hamiltonian is widely used in the field of organic photosystems e.g. photosynthesis since the SSH Hamiltonian allows a distinction of electronic spins, which makes it very easy to compare theoretical results to EPR experiments [101]. The common aspect of all of these three Hamiltonian is the description of energy transfer in terms of electron or energy transfer after photoexcitation using a wave function description.

4 | Theoretical Methods

In this chapter, the relevant methods used in this thesis will be explained in a brief way. Detailed descriptions and derivations of all electronic structure methods can be found in the following reviews, articles and books:

- Hartree-Fock theory [102]
- DFT and TDDFT approaches [103–105]
- MP2, CC2 and ADC(2) methods [106–108]

A detailed description of the following quantum dynamical methods can be found in the following references:

- MCTDH method [15, 109, 110]
- Ehrenfest dynamics [111, 112]

In general, this chapter consists of five parts: part (i) introduces the basic approximations and *ab initio* methods used in this work, part (ii) describes the full quantum multiconfiguration time-dependent Hartree (MCTDH) method and part (iii) explains the semi-classical Ehrenfest method using a wave function/density matrix ansatz. If not specified, all equations are given in atomic units (the Planck constant \hbar , the elementary charge e , the electron mass m_e and the speed of light c are assumed to be 1). Small indices indicate the electronic and capital indices indicate the nuclear coordinates.

Before starting with the description of the relevant approximations and methods, a few words will be addressed to the problem of the theoretical framework of this work and computational chemistry in general.

In general, the exact description of any system can be done using the exact Hamiltonian including the exact wave function for a given system. For typical systems under study, solving the exact Schrödinger equation is analytically and numerically impossible (the Schrödinger equation can be solved exact for e.g. a hydrogen atom or helium cation). Therefore, several approximations and methods have been developed and introduced to solve the Schrödinger equation. The level of approximation starts with elementary ones like the Born-Oppenheimer approximation and is improved from the Hartree-Fock method to the Full CI method. The accuracy of the results for the system under study including all properties (e.g. total energies, excited state energies, relaxed geometries or frequencies) is strongly related

to the used method. For very simple methods like Hartree-Fock, a correct description of e.g. excited states including the correct ordering of the excited states is almost impossible. To solve this problem, better methods like CCS, CCSD, CC2 or ADC(2) are needed to describe excited states correct. The disadvantage of a better description is the computationally higher effort, which increases drastically with higher level methods (in general, every calculation is also scaled by the size of the basis-set which is another factor for the computational effort). Therefore, one has to find a tradeoff between an appropriate description of the molecule including the properties of interest and an acceptable computational time.

4.1 Basic Approximations and *ab initio* Methods

The goal of all quantum methods is to solve the time-(in)dependent molecular Schrödinger equation for a given Hamiltonian \hat{H}

$$\hat{H}\psi(x) = E\psi(x) \quad \text{time-independent Schrödinger equation} \quad (12)$$

$$\hat{H}\Psi(x, t) = i\hbar\frac{\partial}{\partial t}\Psi(x, t) \quad \text{time-dependent Schrödinger equation} \quad (13)$$

In general, the molecular Schrödinger equation is a high dimensional partial differential equation, which cannot be solved analytically (except systems with only one electron). Therefore, several approximations have to be used to solve the Schrödinger equation numerically.

4.1.1 The Born-Oppenheimer Approximation

The molecular Hamiltonian of a given system depends on the electronic and the nuclear degrees of freedom. The first approximation is achieved by separating the electronic and the nuclei part [113]. For this approximation, it is assumed that the electronic degrees of freedom react instantaneously on changes of the nuclei degree of freedom, which can be explained by the large difference of mass of the electronic and the nuclei DOF (the mass of an electron is ≈ 2000 smaller than the mass of a proton). In Eqn.15, the total molecular Hamiltonian is given by

$$H(r, R)\Psi(r, R) = E\Psi(r, R) \quad (14)$$

$$\begin{aligned} H = & - \sum_i^N \frac{1}{2} \nabla_i^2 - \sum_I^M \frac{1}{2M_I} \nabla_I^2 - \sum_i^N \sum_I^M \frac{Z_I}{|r_i - r_I|} \\ & + \sum_{i=1}^N \sum_{j>i}^N \frac{1}{|r_i - r_j|} + \sum_I^M \sum_{J>I}^M \frac{Z_I Z_J}{|r_I - r_J|} \end{aligned} \quad (15)$$

The mass of the nuclei is denoted by M_I , its charge by Z_I . The first two terms of Eqn.15 define the kinetic energy of electrons and nuclei, the third term defines the electron-nuclei interaction, the fourth term defines the electron-electron repulsion and the last term defines nuclei-nuclei repulsion. To separate the molecular Hamiltonian into an electronic part and a nuclei part, all terms of Eqn.15 depending only on the electronic part and parametrically on the nuclear coordinates are described by an electronic Hamiltonian

$$H_{el.} = - \sum_i^N \frac{1}{2} \nabla_i^2 - \sum_i^N \sum_I^M \frac{Z_I}{|r_i - r_I|} + \sum_{i=1}^N \sum_{j>i}^N \frac{1}{|r_i - r_j|} + V(R) \quad (16)$$

with the additive nuclear repulsion term $V(R)$ (the term $V(R) = \sum_I^M \sum_{J>I}^M \frac{Z_I Z_J}{|r_I - r_J|}$ is seen to be constant for a certain geometry). From this, an electronic Schrödinger equation can be constructed

$$H_{el.} \Psi_{el}(r; R) = E_{el.} \Psi_{el}(r; R) \quad (17)$$

where $\Psi(r; R)$ parametrically depends on the nuclear distance R . The total energy for a fixed geometry is given by

$$E_{total} = E_{el.} + \sum_I^M \sum_{J>I}^M \frac{Z_I Z_J}{|r_I - r_J|} \quad (18)$$

For the nuclear degrees of freedom a similar Hamiltonian can be constructed

$$H_{nuc.} = - \sum_I^M \frac{1}{2M_I} \nabla_I^2 + E_{total} \quad (19)$$

which includes the total energy E_{total} . From this approximation, the overall wave function $\Psi(r, R)$ can be described by a product of an electronic and an nuclear wave function

$$\Psi(r, R) = \Phi(R) \Psi_{el}(r; R) \quad (20)$$

Using these expressions, the electron-nuclear problem can be separated into two parts

$$H_{el.}(r; R)\Psi_{el.}(r; R) = E_{el.}(R)\Psi_{el.}(r; R) \quad (21)$$

$$i\hbar \frac{\partial}{\partial t} \Phi(R) = (\hat{T}_{nuc} + E_{el.}(R))\Phi(R) \quad (22)$$

In general, the Born-Oppenheimer approximation is valid as long as the electronic states are not degenerated with respect to the nuclear configuration. For regions near e.g. conical intersections or avoided crossings, the Born-Oppenheimer approximation breaks down.

4.1.2 Hartree-Fock

The fundamental problem in solving the electronic Schrödinger equation is a two-particle problem which is the result of the electron-electron repulsion in the electronic Hamiltonian. To solve this problem, the Hartree-Fock (HF) theory has been developed by D.R. Hartree and V. A. Fock in the 1930th. In the HF ansatz, the system is approximated by a set of noninteracting particles. The corresponding wave function is given by the product of one-particle wave functions

$$\Psi_{el.}(x_1, x_2, \dots, x_N; R) = \chi_i(x_1)\chi_j(x_2)\dots\chi_k(x_N) \quad (23)$$

This so-called Hartree-Product does not fulfill the Pauli antisymmetry principle. To fulfill this principle, a Slater-determinant is used to create an antisymmetric wave function

$$\begin{aligned} \Psi_{el.}(x_1, x_2, \dots, x_N; R) &= \frac{1}{\sqrt{N!}} \begin{vmatrix} \chi_i(x_1) & \chi_j(x_1) & \cdots & \chi_k(x_1) \\ \chi_i(x_2) & \chi_j(x_2) & \cdots & \cdots \\ \cdot & \cdot & \cdot & \cdot \\ \cdot & \cdot & \cdot & \cdot \\ \chi_i(x_N) & \cdots & \cdots & \chi_k(x_N) \end{vmatrix} \\ &= |\chi_i(x_1)\chi_j(x_2)\dots\chi_k(x_N)\rangle \end{aligned} \quad (24)$$

Using the wave function of Eqn.24 and the variational principle, the minimum energy of a system can be calculated by

$$E_0 \geq \langle \Psi_0 | H | \Psi_0 \rangle \quad (25)$$

using the optimal Ψ_0 function (using the exact wave function and the exact Hamiltonian, one would obtain the exact minimum energy). Therefore, the Hartree-Fock energy is determined by the eigenvalue problem

$$f(i)\chi(x_i) = \epsilon_i\chi(x_i) \quad (26)$$

with the Fock-operator f defined by

$$f(i) = h(i) + V^{HF}(i) \quad (27)$$

$$= -\frac{1}{2}\nabla_i^2 - \sum_{I=1}^M \frac{Z_I}{r_{iI}} + V^{HF}(i) \quad (28)$$

where $h(i)$ denotes the one-particle Hamiltonians and V^{HF} the Hartree-Fock potential. This potential includes a Coulomb (J) and exchange operator (K). In other words, using the Hartree-Fock approach, an electron i is described in the mean field of all other electrons by taking the correlation and the exchange of one electron with respect to all other electrons into account. Since the mean field depends on the wave function itself, this leads to a self-consistent-field procedure (SCF). This procedure allows to calculate the minimum energy for a given system using an initial guess for the wave function applied to the variational principle. During the SCF procedure, the wave function is optimized with respect to convergence parameter e.g. the change of total energy.

4.1.3 DFT and TDDFT

In contrast to the Hartree-Fock method, in density functional theory (DFT) the set of single-electron equations is derived in a different manner. The idea is not to use a complex wave function, which depends on the spin and the spatial coordinates for the electrons (for fixed nuclei positions) but to use a density, which is an equivalent representation to a wave function and only depends on the spatial coordinates of the electrons. The density is defined by

$$\rho = \sum_i^N |\chi_i|^2 \quad (29)$$

with the Slater-determinal wave function χ_i . The DFT method is based on the Hohenberg-Kohn (HK) theorems [114], which proof that for a given external potential $V_{ext.}$, the electronic ground-state energy of a system of N electrons is defined by a definite electron density (HK 1) and that the correct ground-state density minimizes the total energy of the system (HK 2). Therefore, the knowledge of the exact potential $V_{ext.}$ will lead to the exact ground-state minimum energy. Similar, to the SCF method of the Hartree-Fock approach, the Kohn-Sham self-consistent field method [115] has been developed to solve the Schrödinger equation.

For a non-interacting system of N electrons, the energy is given by

$$\begin{aligned}
 E[\rho(r)] = & \sum_{i=1}^N \left(\langle \chi_i | -\frac{1}{2} \nabla_i^2 | \chi_i \rangle - \langle \chi_i | \sum_{I=1}^M \frac{Z_I}{|r_i - r_I|} | \chi_i \rangle \right) \\
 & + \sum_{i=1}^N \langle \chi_i | \frac{1}{2} \int \frac{\rho(r')}{|r_i - r'|} dr' | \chi_i \rangle + E_{xc}[\rho(r)]
 \end{aligned} \tag{30}$$

with the kinetic energy of the electrons described by the first term, the second term describing the electron-nuclear repulsion, the third term describing the electron-electron repulsion and the last term E_{xc} defining the exchange-correlation energy including the exchange and correlation terms and also the classical self-interaction energy. Similar as in HF, an eigenvalue problem has to be solved

$$h_i^{KS} \chi_i = \epsilon_i \chi_i \tag{31}$$

by finding the optimal χ_i . The one-electron Kohn-Sham operator h_i is defined by

$$h_i^{KS} = -\frac{1}{2} \nabla_i^2 - \sum_{I=1}^M \frac{Z_I}{|r_i - r_I|} + \int \frac{\rho(r')}{|r_i - r_j|} dr' + V_{xc}[\rho(r)] \tag{32}$$

with the exchange-correlation functional $V_{xc}[\rho(r)]$. Due to the (so far) unknown exact potential of this term, an exact solution of the DFT method is not possible (only the exact form for the free electron gas is known, which is not helpful in this context). To avoid this problematic term, several functionals have been developed to approximate the exchange-correlation term in a correct way e.g. local density approximation (LDA) [116], gradient approximations (GGA) [117] or hybrid functionals like B3LYP [118].

So far, only the time-independent case has been considered. The time-dependent extension of the DFT ansatz is the so called time-dependent density functional theory (TDDFT), which can be derived using the Runge-Gross (RG) theorem [119]. The RG theorem is very similar to the HK theorems, and proves that an one-to-one mapping between the time-dependent density and the external potential exists (RK 1). In contrast to DFT which is based on the HK 2 theorem, an equivalent RG 2 theorem cannot be formulated. Nevertheless, the RG 1 theorem defines an action functional $A[\rho]$ for the time-dependent density for which the exact density is a stationary point. Based on the RG theorem, a Kohn-Sham like non-interacting system with an explicit time-dependency can be formulated

$$\left[-\frac{1}{2} \nabla^2 + v_s(r, t) \right] \phi_i(r, t) = i \frac{\partial}{\partial t} \phi_i(r, t) \tag{33}$$

with the potential $v_s(r, t)$

$$v_s(r, t) = v_s[\rho](r, t) = v_{ext}(r, t) + \int \frac{\rho(r', t)}{|r - r'|} dr' + V_{xc}[\rho(r)] \tag{34}$$

defined by the external potential $v_{ext}(r,t)$ and the action functional $V_{xc} = \frac{\delta A_{xc}}{\delta \rho}$. If the exchange-correlation action potential is known, the resulting density of the non-interacting system should be identical to the density of the interacting system. Unfortunately, this is not the case but TDDFT is applicable as an extension to DFT to calculate excited state. Usually, the same exchange-correlation functionals are used as in standard DFT.

Comparing the Hartree-Fock and the (TD-)DFT method, several aspects have to be considered. In HF theory, a wave function is used whereas in DFT a density is used. The consequence of this is that on the one hand, the density is an experimental available quantity and on the other hand, a density can be described only by three coordinates and the number of electrons. This benefit can be used for a computationally fast evaluation of the density, while for a wave function based method, increasing the system size will also increase the wave function rapidly. Therefore, DFT is able to describe larger systems including more electrons in a reliable time. The most important drawback of DFT is the approximation of the exchange-correlation functional: using a non-suitable XC-functional will lead to completely wrong results. Furthermore, the description of excited states, especially the description of charge-transfer states, can be very inaccurate. TDDFT often underestimates the excitation energy of CT states and therefore, the ordering of excited states calculated by TDDFT is untrustworthy. Therefore, it is always recommended to evaluate the used XC functional. Nevertheless, DFT and TDDFT are state-of-the-art methods for many applications and widely used even thanks to the fact that a lot of different XC-functionals have been developed e.g. long-range corrected functionals for a correct excited state description by TDDFT.

4.1.4 High-Level *ab initio* Methods: MP2, CC2 and ADC(2)

The main problem of standard TDDFT is the wrong description of charge-transfer states, the general underestimation of their electronic excitation energies and in some cases, the wrong description of molecular geometries. A lot of work has been done on the TDDFT side to overcome these problems by developing new functionals e.g hybrid or double hybrid functionals or long-range corrected functionals but the problem still exists.

Another approach to solve these problems is to use higher level methods which describe e.g. charge-transfer states on a correct level including electron correlation. Two of the most prominent and widely used methods are the second-order approximate coupled cluster singles and doubles theory (CC2) [120] and the algebraic diagrammatic construction second order (ADC(2)) method [107], which allow a

very accurate description of excitation energies and charge-transfer states even for larger molecules. Both methods, CC2 and ADC(2), are similar to perturbation theory, and therefore, the Møller-Plesset (MP) perturbation theory [121] will be introduced (to keep it short, only the lowest energy state will be considered) in the beginning of this section. The MP theory was developed in 1934 by C. Møller and M. S. Plesset to overcome the limitations of the Hartree-Fock theory by including electron correlation. The electron correlation is not explicitly described by HF theory and describes the electron-electron interaction. This interaction is important for a correct description of the system and cannot be described by a single Slater determinant, which is used in the HF method. Assuming that the total Hamiltonian is given by

$$H = H_0 + \lambda H' \quad (35)$$

$$H_0 \Phi_i = E_i \Phi_i \quad i = 0, 1, 2, \dots, \infty \quad (36)$$

with the unperturbed Hamiltonian H_0 , the perturbation H' and the perturbation parameter λ . For the unperturbed Hamilton operator ($\lambda = 0$), the solutions of Eqn.36 form a closed set and are known. These equations can be solved using approximations such as HF. The perturbed Schrödinger equation is given by

$$H\Psi = E_{Per.}\Psi \quad (37)$$

For $\lambda = 0$ one obtains

$$H_0\Phi_0 = E_0\Phi_0 \quad (38)$$

The energy and the wave function can be written in terms of a Taylor-expansion in powers of the perturbation parameter λ

$$E_{Per.} = \lambda^0 E_0 + \lambda^1 E_1 + \lambda^2 E_2 + \dots \quad (39)$$

$$\Psi = \lambda^0 \Psi_0 + \lambda^1 \Psi_1 + \lambda^2 \Psi_2 + \dots \quad (40)$$

With these expressions, Eqn.37 can be expressed by

$$\begin{aligned} & (H_0 + \lambda H')(\lambda^0 \Psi_0 + \lambda^1 \Psi_1 + \lambda^2 \Psi_2 + \dots) \\ & = (\lambda^0 E_0 + \lambda^1 E_1 + \lambda^2 E_2 + \dots)(\lambda^0 \Psi_0 + \lambda^1 \Psi_1 + \lambda^2 \Psi_2 + \dots) \end{aligned} \quad (41)$$

which includes all possible values for λ and therefore, all terms with the same order can be collected (for simplification, only terms up to second order will be shown)

$$\begin{aligned}
 \lambda^0 : H_0 \Psi_0 &= E_0 \Psi_0 \\
 \lambda^1 : H_0 \Psi_1 + H' \Psi_0 &= E_0 \Psi_1 + E_1 \Psi_0 \\
 \lambda^2 : H_0 \Psi_2 + H' \Psi_1 &= E_0 \Psi_2 + E_1 \Psi_1 + E_2 \Psi_2 \\
 &\vdots
 \end{aligned} \tag{42}$$

These expressions can be used to improve the calculation by including higher order terms. In general, to solve these equations, an appropriate unperturbed Hamiltonian has to be chosen. The most common choice is to take this as a sum over Fock operators, which will double include the average electron-electron repulsion. For this case, the perturbation becomes $V_{ee} - \langle V_{ee} \rangle$ which is also known as fluctuation potential.

$$\begin{aligned}
 H_0 &= \sum_{i=1}^{N_{elec}} F_i = \sum_{i=1}^{N_{elec}} \left(h_i + \sum_{j=1}^{N_{elec}} (J_j - K_j) \right) \\
 &= \sum_{i=1}^{N_{elec}} h_i + \sum_{i=1}^{N_{elec}} \sum_{j=1}^{N_{elec}} \langle g_{ij} \rangle = \sum_{i=1}^{N_{elec}} h_i + 2V \langle V_{ee} \rangle \\
 H' &= H - H_0 = \sum_{i=1}^{N_{elec}} \sum_{j>i}^{N_{elec}} g_{ij} - \sum_{i=1}^{N_{elec}} \sum_{j=1}^{N_{elec}} \langle g_{ij} \rangle = V_{ee} - 2\langle V_{ee} \rangle
 \end{aligned} \tag{43}$$

For the zeroth-order, one obtains the HF determinant for the wave function. In zeroth-order, the energy is just a sum of MO energies. For the first-order, one obtains the HF energy, which is given by

$$MP(0) : E(MP(0)) = \langle \Psi_0 | H_0 | \Psi_0 \rangle = \sum_{i=1}^{N_{elec}} \epsilon_i \tag{44}$$

$$MP(1) : E(MP(0)) + E(MP(1)) = \langle \Psi_0 | H' | \Psi_0 \rangle + \langle \Psi_0 | H_0 | \Psi_0 \rangle = E_{HF} \tag{45}$$

This is related to the fact that the overcounting of the electron-electron repulsion at zeroth-order is corrected by the first-order term and therefore, the electron correlation correction starts with the second-order term of the MP theory.

$$MP(2) : \sum_{i<j}^{occ} \sum_{a<b}^{virt} \frac{\langle \Phi_0 | H' | \Phi_{ij}^{ab} \rangle \langle \Phi_{ij}^{ab} | H' | \Phi_0 \rangle}{E_0 - E_{ij}^{ab}} \tag{46}$$

The matrix elements between the HF and the double excited determinants are given by two-electron integrals over MOs, which can be calculated using numerical methods. In accordance to Koopmans theorem, the difference in total energy becomes a difference in MO energies and therefore, the MP(2) energy is given by

$$E(MP(2)) = E(MP(1)) + \sum_{i<j}^{occ} \sum_{a<b}^{virt} \frac{\langle \phi_i \phi_j | \phi_a \phi_b \rangle - \langle \phi_i \phi_j | \phi_b \phi_a \rangle}{\epsilon_i + \epsilon_j - \epsilon_a - \epsilon_b} \tag{47}$$

In principle, the MP theory can be extended to higher order, while in practice, the numerical effort for these type of calculation is already very high and therefore, second-order type calculations are used for most systems. To improve the calculation of a specific type of correction (e.g. singles or doubles) a coupled cluster (CC) approach is used, which includes all corrections of a given type to infinite order (this is in contradiction to MP theory, which adds all types of corrections to a given order).

In CC, an excitation operator is defined by

$$T = T_1 + T_2 + T_3 + T_4 + \dots + T_{N_{elec}} \quad (48)$$

Depending on the type of T_i , one can generate the Slater determinants for singles, doubles etc. using a HF reference wave function Φ_0

$$T_1\Phi_0 = \sum_i^{occ} \sum_a^{virt} t_i^a \Phi_i^a \quad (49)$$

$$T_2\Phi_0 = \sum_{i<j}^{occ} \sum_{a<b}^{virt} t_{ij}^{ab} \Phi_{ij}^{ab} \quad (50)$$

The CC wave function is defined by

$$\Psi_{CC} = e^T \Phi_0 \quad (51)$$

$$e^T = 1 + T + \frac{1}{2}T^2 + \frac{1}{6}T^3 + \dots = \sum_{k=0}^{\infty} \frac{1}{k!} T^k \quad (52)$$

Using the expression of Eqn.48, one can define all types of excitations and rewrite the general Schrödinger equation in terms of the CC wave function

$$He^T \Phi_0 = Ee^T \Phi_0 \quad (53)$$

Projecting Eqn.53 onto a reference wave function and expanding out the exponentials, one will end up with the CC energy defined by

$$E_{CC} = \langle \Phi_0 | He^T | \phi_0 \rangle \quad (54)$$

To avoid computational effort, the CC theory is usually truncated after second-order. The CC2 method is an additional approximation to CC theory, which includes the equation for singles exact but approximates the doubles to first-order only. In other words, the CC2 equations are only a subset of the full CCSD equations. Therefore, CC2 is less expensive and accurate as "real" CCSD but still better than CIS or CCS.

In the ADC(2) approximation, a similar ansatz is used: the ADC(2) excitation energies are obtained as eigenvalues of a hermitian matrix. The basis of this ansatz

is the construction of a many-particle basis based on the exact ground state wave function $|\Psi_0\rangle$. To calculate the excited states, a set of excitation operators \hat{C}_I is applied on this ground state wave function, which are represented by pairs of creation and annihilation operators

$$\hat{C}_I \in \{ \hat{c}_a^\dagger \hat{c}_i; \hat{c}_b^\dagger \hat{c}_j \hat{c}_a^\dagger \hat{c}_i, a < b, i < j; \dots \} \quad (55)$$

Applying these excitation operators on the ground state wave function results in

$$|\Psi_I^\#\rangle = \hat{C}_I |\Psi_0\rangle \quad (56)$$

where the resulting states can be grouped into classes of single, doubled or higher excitations. The problem of this ansatz is the fact that the so obtained states are not necessarily orthogonal to each other. Therefore, the excited states wave function $|\Psi_I^\#\rangle$ has to be orthogonalized. This orthogonalization can be performed using e.g. a Gram-Schmidt orthogonalization, which results in the basis of orthonormal intermediate states $|\tilde{\Psi}_I\rangle$. These intermediate states can be used to construct a matrix representation of a shifted Hamiltonian $\hat{H} - E_0$

$$M_{I,J} = \langle \tilde{\Psi}_I | \hat{H} - E_0 | \tilde{\Psi}_J \rangle \quad (57)$$

where the diagonalization of $M_{I,J}$ will in principle result in the exact excited states and the excited states energies within the given single-particle basis. Due to the fact that neither the exact excited state or ground state energy is known, these energies have to be approximated by n -th order MP theory. This will result in the n -th order ADC equations.

In general, the theoretical effort of CC2 and ADC(2) scales by $\approx N^5$ compared to (TD-)DFT $\approx N^3$, which limits these high-level methods to smaller systems than in TDDFT case (N is the number of basis functions). The great advantage of the ADC(2) method over the CC2 method is the derivation of excitation energies: the ADC(2) excitation energies are obtained as eigenvalues of a hermitian matrix whereas the CC2 excitation energies are obtained as eigenvalues of a non-hermitian Jacobi matrix. The overall accuracy of both methods is comparable, but it is possible that the CC2 wave function can be less stable because of numerical problems which can complicate further analysis based on the wave function e.g. the analysis of electron-hole distributions. Therefore, MP2 and ADC(2) as implemented in the TURBOMOLE program package are used for the ground and excited state optimization, the calculation of the PES cuts and the analysis of the excited states using a density matrix approach.

4.2 Beyond Born-Oppenheimer: Dynamics on Non-Adiabatically Coupled Potential Energy Surfaces

In the framework of the BO-approximation, one neglects that the nuclear kinetic energy operator has non-zero matrix elements between different electronic eigen functions. However, these matrix elements are of key importance in excited-state dynamics since they generate ultrafast decay channels between different electronic states. If the states come energetically very close, non-adiabatic transitions due to the non-zero matrix elements can be observed. Therefore, a more general wave function ansatz, the so-called group BO ansatz, is needed, which allows to describe these phenomena

$$\Psi(r, R) = \sum_n \psi_n(r_{el.}; R) \phi_n(R) \quad (58)$$

where $\psi_n(r_{el.}; R)$ are solutions of the electronic Schrödinger equation. By integration over the electronic coordinates, it turns out that the nuclear wave functions $\phi(R)$ are coupled to each other

$$\left(-\frac{\hbar^2}{2M} \frac{\partial^2}{\partial R^2} + \epsilon_n(R) \right) \phi_n + \sum_{n \neq m} \hat{\Lambda}_{mn} \phi_m = E \phi_n \quad (59)$$

$\hat{\Lambda}_{mn}$ describes the non-adiabatic coupling and is given by

$$\hat{\Lambda}_{mn} = -\frac{\hbar^2}{M} \langle \psi_m | \frac{\partial}{\partial R} | \psi_n \rangle \frac{\partial}{\partial R} + \langle \psi_m | \hat{T}_N | \psi_n \rangle \quad (60)$$

For a more intuitive interpretation, a matrix representation can be used

$$i\hbar \frac{\partial}{\partial t} \begin{pmatrix} \phi_1(R, t) \\ \phi_2(R, t) \end{pmatrix} = \begin{pmatrix} \hat{T}_N + \epsilon_1(R) & \hat{\Lambda}_{12}(R) \\ \hat{\Lambda}_{21}(R) & \hat{T}_N + \epsilon_2(R) \end{pmatrix} \begin{pmatrix} \phi_1(R, t) \\ \phi_2(R, t) \end{pmatrix} \quad (61)$$

By applying an appropriate unitary transformation of the electronic wave functions, a diabatic representation is formulated. In the diabatic representation, the kinetic energy coupling almost vanish

$$\Phi^{dia.}(r_{el.}; R) = S(R) \psi^{ad.}(r_{el.}; R) \quad (62)$$

Using the matrix representation

$$i\hbar \frac{\partial}{\partial t} \begin{pmatrix} \tilde{\phi}_1(R, t) \\ \tilde{\phi}_2(R, t) \end{pmatrix} = \begin{pmatrix} \hat{T}_N + V_1^{dia}(R) & V_{12}(R) \\ V_{21}(R) & \hat{T}_N + V_2^{dia}(R) \end{pmatrix} \begin{pmatrix} \tilde{\phi}_1(R, t) \\ \tilde{\phi}_2(R, t) \end{pmatrix} \quad (63)$$

it turns out that the coupling terms can be described by a potential term. In practice, the diabatic representation is preferred since the diabatic states have a well defined electronic character. Furthermore, the calculation of derivative couplings is avoided (for a more detailed discussion, see Ref. [122]).

4.3 The Multiconfiguration Time-Dependent Hartree Method (MCTDH)

To describe quantum dynamical phenomena such as electron transfer processes or the dynamical interaction of a system with the environment, one has to solve the time-dependent Schrödinger equation for a system using a full quantum ansatz. A very effective approach is the so-called Multiconfiguration Time-Dependent Hartree (MCTDH) method, which has been developed by Meyer, Manthe and Cederbaum in 1990 [14, 109, 110, 123].

First attempts to solve the time-dependent Schrödinger equation have been done using the Time-Dependent Hartree (TDH) method. The great advantage of the MCTDH method is the very efficient and flexible full quantum correlated description of the wave function, which is also reliable for systems up to 100 degrees of freedom. The basis of the MCTDH method for a system with f degrees of freedom described by the coordinates q_1, \dots, q_f is a wave function of the form

$$\Psi(q_1, \dots, q_f, t) = \Psi(Q_1, \dots, Q_p, t) \quad (64)$$

$$= \sum_{j_1=1}^{n_1} \cdots \sum_{j_p=1}^{n_p} A_{j_1 \dots j_p}(t) \varphi_{j_1}^{(1)}(Q_1, t) \cdots \varphi_{j_p}^{(p)}(Q_p, t) = \sum_J A_J \Phi_J \quad (65)$$

$$= \sum_{j=1}^{n_\kappa} \varphi_j^{(\kappa)} \Psi_j^{(\kappa)} \quad (66)$$

The wave function Ψ is described by a direct-product of p sets of orthonormal time-dependent basis-functions φ^κ , the so-called *single-particle functions* (SPF). This ansatz is very similar to the standard wave packet expansion, but uses a time-dependent SPF basis. Applying the MCTDH wave function to the Dirac-Frenkel variational principle, a coupled set of equations can be obtained, one for the expansion coefficient and one for each set of SPFs

$$i\dot{A} = KA \quad (67)$$

$$i\dot{\varphi} = (1 - P^{(\kappa)})(\rho^{(\kappa)})^{-1} H^{(\kappa)} \varphi^{(\kappa)} \quad (68)$$

with the projector onto the space spanned by the SPFs

$$P^{(\kappa)} = \sum_j |\varphi_j^{(\kappa)}\rangle \langle \varphi_j^{(\kappa)}| \quad (69)$$

and the density matrix $\rho^{(\kappa)} = \langle \Psi_a^{(\kappa)} | \Psi_b^{(\kappa)} \rangle$. The Hamiltonian operator K is expressed in a matrix form represented in the basis of Hartree products

$$K_{JL} = \langle \Phi_J | H | \Phi_L \rangle \quad (70)$$

while the mean-field operator matrix $H^{(\kappa)}$ is given by

$$H_{ab}^{(\kappa)} = \langle \Psi_a^{(\kappa)} | H | \Psi_b^{(\kappa)} \rangle \quad (71)$$

with

$$\Psi_a^{(\kappa)} = \sum_{J^\kappa} A_{J^\kappa} \Phi_{J^\kappa} \quad (72)$$

The presented form of the wave function of the MCTDH formalism allows an efficient calculation using up to 100 DOF but is often limited to only a small number of electronic states (≈ 10 ; the computational effort strongly correlates with the used Hamiltonian and can be increased using the single-set formalism).

To overcome this limitation, the so called multilayer (ML) formalism is used [15]. This formalism expands the wave function in terms of n layers and allows the description of systems up to 1000 DOF and several 100 electronic states. The general form of the ML-MCTDH wave function is given by

$$|\Psi\rangle = \sum_{j_1} \sum_{j_2} \dots \sum_{j_M} A_{j_1, j_2, \dots, j_M}(t) \prod_{k=1}^M \left[\sum_{i_1} \sum_{i_2} \dots \sum_{i_Q} B_{i_1, i_2, \dots, i_Q}^{k, j_k}(t) \prod_{q=1}^Q |\nu_{i_q}^{k, q}(t)\rangle \right] \quad (73)$$

For comparison, see Eqn.65.

In general, the MCTDH equations are norm preserving and for time-independent operators, energy conserving, which is an important property of this method, since the norm is an important measure of the quality of a calculation. Furthermore, the density can be used as an additional measure of quality, since the eigenfunctions of the density matrix can be seen as natural orbitals and the eigenvalues provide the populations of this function, which is very similar to electronic structure calculations. Therefore, the natural orbital population gives an additional measure for the quality of a calculation.

4.4 Ehrenfest Dynamics

In contrast to the MCTDH method introduced in the previous section, the Ehrenfest approach is a semi-classical approach based on the Ehrenfest theorem [111,

124]. In general, the Ehrenfest theorem connects quantum mechanics to classical mechanics by assuming that the expectation values $\langle x \rangle_t$ and $\langle p \rangle_t$ of a moving wave packet are identical to the classical values x_t and p_t . Assuming the time-dependence of the expectation value of an operator $\langle A \rangle$

$$\langle A \rangle = \int \Psi^* A \Psi d\tau \quad (74)$$

then

$$\frac{d}{dt} \langle A \rangle = \left\langle \frac{d\Psi}{dt} | A \Psi \right\rangle + \left\langle \Psi | A \frac{d\Psi}{dt} \right\rangle + \left\langle \Psi | \frac{\partial A}{\partial t} \Psi \right\rangle \quad (75)$$

Using the fact that

$$i\hbar \frac{\partial \Psi}{\partial t} = H \Psi \quad (76)$$

$$i\hbar \frac{\partial \Psi^*}{\partial t} = -H \Psi^* \quad (77)$$

Eqn.75 can be rewritten

$$\frac{d}{dt} \langle A \rangle = \frac{1}{i\hbar} \langle -H \Psi | A \Psi \rangle + \frac{1}{i\hbar} \langle \Psi | A | H \Psi \rangle + \left\langle \Psi | \frac{\partial A}{\partial t} \Psi \right\rangle \quad (78)$$

$$= \frac{1}{i\hbar} \langle \Psi | [A, H] | \Psi \rangle + \left\langle \frac{\partial A}{\partial t} \right\rangle \quad (79)$$

Assuming that the operator A has no implicit time-dependence, the time-evolution of the expectation value of A can be described by

$$i\hbar \frac{d}{dt} \langle A \rangle = \langle \Psi | [A, H] | \Psi \rangle \quad (80)$$

For Hamiltonians of the form $H = p^2/2m + V(q)$, one arrives at the Ehrenfest theorem (with A= q or p):

$$\frac{d}{dt} \langle q \rangle = \frac{\langle p \rangle}{m} \quad (81)$$

$$\frac{d}{dt} \langle p \rangle = \left\langle -\frac{\partial V}{\partial q} \right\rangle \quad (82)$$

The Ehrenfest model is widely used when a decomposition of a given system into a classical and a quantum system is needed, e.g. when the dynamics of electrons is described quantum mechanically whereas the dynamics of the nuclei is described classically. The advantage of this separation is the possibility to describe large systems with many degrees of freedom on a correct level, since for a large number of individual trajectories, the classical expectation values for q and p are in agreement with the quantum expectation values, whereas the electronic part of the system is described by a quantum wave function. In general, quantum effects such as

coherence are not well described by Ehrenfest dynamics, which is related to the loss of phase information after calculating the expectation value.

4.4.1 Ehrenfest Equations of Motion: Wave Function Based Ansatz

To derive the Ehrenfest equations of motion [112] for q , p and the electronic part for a single trajectory, the Hamiltonian of a full quantum system is again

$$\begin{aligned}
 \hat{H} &= -\hbar^2 \sum_J \frac{1}{2M_J} \nabla_J^2 - \hbar^2 \sum_j \frac{1}{2} \nabla_j^2 + \frac{1}{4} \sum_{J < K} \frac{Z_J Z_K}{|Q_J - Q_K|} \\
 &\quad - \frac{1}{4} \sum_{j < k} \frac{1}{|q_j - q_k|} - \frac{1}{4} \sum_{J,j} \frac{Z_J}{|Q_J - q_j|} \\
 &= -\hbar^2 \sum_J \frac{1}{2M_J} \nabla_J^2 - \hbar^2 \sum_j \frac{1}{2} \nabla_j^2 + V_{n-e}(r, R) \\
 &= -\hbar^2 \sum_J \frac{1}{2M_J} \nabla_J^2 + H_{el.}(q, Q)
 \end{aligned} \tag{83}$$

with M_J the mass of the J s nucleus and Z_J is the charge of the J s nucleus (small indices indicate the electronic degree of freedom). Furthermore, the potential V_{n-e} and the electronic Hamiltonian $H_{el.}(q, Q)$ have been defined to contain the electronic contribution. The Born-Oppenheimer approximation is applied and thus the wave function is represented by

$$\begin{aligned}
 \Psi(q, Q, t) &= \varphi_{el.}(q, t; Q) \phi_{nuc.}(Q, t) \\
 \varphi_{el.}(q, t; Q) &= \sum_{i=1}^{\infty} c_i(t) \varphi_i(q, t; Q)
 \end{aligned} \tag{84}$$

where the electronic wave function $\varphi_{el.}$ is represented in the basis of the electronic states i satisfying the condition $\sum_i |c_i(t)|^2 = 1$. Up to now, the nuclear and the electronic subsystem are still coupled. After applying a classical limit procedure to the nuclear part, one will arrive at the Ehrenfest equations of motion:

$$M_J \ddot{Q}_J = -\langle \Psi | \nabla_J H_{el.}(q, Q) | \Psi \rangle \tag{85}$$

$$i\hbar \frac{d}{dt} | \Psi \rangle = H_{el.}(q, Q) | \Psi \rangle \tag{86}$$

These equations can be transformed into a Hamilton-type description using a Hamiltonian function of the form

$$H(q, p) = \sum_J \frac{p_J^2}{2M_J} + \langle \Psi | H_{el.}(q, p) | \Psi \rangle \tag{87}$$

and by fixing a relation of the form

$$p_J = M\dot{q}_J \quad (88)$$

The resulting equations are very similar to the Hamilton's equations

$$\begin{aligned} \frac{dq_J}{dt} &= \frac{p_J}{M_J} \\ \frac{dp_J}{dt} &= -\langle \Psi | \nabla_J H_{el.}(r, q) | \Psi \rangle \\ i\hbar \frac{d}{dt} | \Psi \rangle &= H_{el.} | \Psi \rangle \end{aligned} \quad (89)$$

The equation of motion given in Eqn.89 can be used to study different types of systems with a different number of states as long as the system is a closed system.

4.4.2 Ehrenfest Equations of Motion: Density Matrix Based Ansatz

Instead of using an ansatz with a wave function of the form $\Psi = \sum_i c_i(t)\varphi_i$, a density matrix ansatz can be used [125, 126]. The benefit of a density matrix representation is the fact that it can be easily extended to open systems e.g systems including a dissipative state. In general, the density is defined by

$$\rho = \sum_i |\psi_i\rangle\langle\psi_i| \quad (90)$$

and the EOM's of the coordinate, the momentum and the density are given by

$$\begin{aligned} \frac{dq_J}{dt} &= \frac{p_J}{M} \\ \frac{dp_J}{dt} &= -Tr(\nabla_J H_{el.}\rho) \\ \frac{d\rho}{dt} &= -i[H_{el.}, \rho] \end{aligned} \quad (91)$$

where the square brackets denote the commutator. To introduce dissipative dynamics as one would expect in open quantum systems, an additional dissipative part has to be introduced e.g. an additional non-hermitian Hamiltonian with a uni-direct coupling from a system state to the dissipative state. The time-derivative of the density is now given by

$$\frac{d\rho}{dt} = L_{Sys.}\rho + L_{diss.}\rho \quad (92)$$

with the Liouville superoperator for the system or the dissipative part. $L_{Sys,\rho}$ is equivalent to $-i[H_{el.}, \rho]$ while $L_{diss.}$ only includes the coupling of the system to the dissipative state.

One of the most important aspects of the Ehrenfest dynamics is a very easy implementation of a temperature dependent environment, which can be described e.g. by a Langevin bath [127]. The Langevin bath is a description which introduces dissipation on the one hand but also thermal response (fluctuation) on the other hand. The implementation using the Ehrenfest equations is given by

$$\frac{dp_J}{dt} = -\langle \Psi | \nabla_J H_{el.}(r, q) | \Psi \rangle - \gamma \frac{p_J}{M} + B \quad (93)$$

$$B = \chi \sqrt{\frac{2\gamma m k_B T}{\Delta t}} \quad (94)$$

where the second term in the r.h.s introduces a friction and the third term a temperature dependent fluctuation. χ is a random number from a normal distribution centered around $x_0 = 0$.

In general, the Ehrenfest method is performed by running n independent trajectories and calculating the average of these trajectories, which reduces the computational costs of the Ehrenfest method drastically compared to the full quantum MCTDH method. In theory, a good implementation of the initial condition generation and the propagation of the system will allow a linear scaling with the system size l , since all trajectories can be calculated in parallel because they are independent to each other.

4.4.3 Multiconfigurational Ehrenfest Dynamics

As mentioned above, the wave function is represented by a set of independent trajectories, which can be seen as a set of delta functions. This implies no overlap between the individual trajectories and therefore, coherence effects related to the overlap of the individual trajectories are not described. This aspect can be very important for the dynamics, especially on the short time scale (several tens or hundreds of fs). To overcome this problem, the overlap between the trajectories has to be taken into account by introducing a wave function representation using Gaussian functions. This results in a multiconfigurational type description as described by Shalashilin et al. [128, 129]. In the following, this ansatz will be described briefly.

As demonstrated by Römer et al. in [130], a classical limit wave function according to the 'single-set' formulation of Gaussian-based G-MCTDH can be expressed by

$$|\Psi^{qc}(r, t)\rangle = \sum_{l=1}^L \sum_{n=1}^N B_{nl}(t) \exp\left(\frac{i}{\epsilon} S_l^{cl}(t)\right) g_{\epsilon,l}(r; q_l(t), p_l(t)) |n\rangle \quad (95)$$

$$= \sum_{l=1}^L \sum_{n=1}^N B_{nl} g_l^{cl}(r, t) |n\rangle \quad (96)$$

$$= \sum_{l=1}^L |\Phi_l^{qc}(r, t)\rangle \quad (97)$$

where $|\Phi_l^{qc}\rangle$ refers to an 'Ehrenfest configuration'. In the classical limit, these configurations are found to decouple which allows an evolution of the coefficients and Gaussian wave packet (GWP) parameters according to the classical Ehrenfest ansatz (see Eqn.89). It has to be noted that phase information is implied in this ansatz by the phase factor $\exp(\frac{i}{\epsilon} S_l^{cl}(t))$ which results from the classical-limit G-MCTDH equations (S_l^{cl} refers to the classical action). Since in practice non-scaled, finite-width GWP will be used for the sampling of the initial conditions and the reconstruction of the wave function, norm conservation needs to be guaranteed. Therefore, an additional set of coefficients A_l with each Ehrenfest configuration is introduced [131] and the time evolution of these coefficients to be determined based on the Dirac-Frenkel variational principle. The resulting quantum-classical wave function is given by

$$|\Psi^{qc}(r, t)\rangle = \sum_{l=1}^L A_l(t) |\Phi_l^{qc}(r, t)\rangle \quad (98)$$

$$= \sum_{l=1}^L A_l(t) \left[\sum_{n=1}^N B_{nl}(t) g_l^{cl}(r, t) |n\rangle \right] \quad (99)$$

$$= \sum_{l=1}^L \sum_{n=1}^N A_l B_{nl}(t) \exp\left(\frac{i}{\epsilon} S_l^{cl}(t)\right) g_{\epsilon,l}(r; q_l(t), p_l(t)) |n\rangle \quad (100)$$

with the classical-limit GWP and the B_{nl} coefficients following the classical Ehrenfest EOM while the new set of coefficients A_l are obtained from the Dirac-Frenkel variational principle. The complete set of EOMs for the multiconfigurational Ehrenfest dynamics (MCE) is given by

$$\frac{dq_J}{dt} = \frac{p_J}{M} \quad (101)$$

$$\frac{dp_J}{dt} = -\langle \Psi | \nabla_J H_{el.}(r, q) | \Psi \rangle \quad (102)$$

$$i \frac{dB_l}{dt} = H_{el.} B_l \quad (103)$$

$$iS \frac{dA}{dt} = (\tilde{H} - i\tau) A \quad (104)$$

with the time derivative of the A-coefficients. All matrix elements needed for the calculation of the derivative of A are formulated in the basis of Ehrenfest configurations $|\Phi_l^{qc}\rangle$ and given by

$$\tilde{H}_{lk} = \langle \Phi_l^{qc} | H | \Phi_k^{qc} \rangle \quad (105)$$

$$= \sum_n \sum_{n'} B_{nl}^* B_{n'k} \langle n | g_l^{cl} | H | g_k^{cl} \rangle n' \quad (106)$$

and similarly for the overlap matrix elements S_{lk}

$$S_{lk} = \langle \Phi_l^{qc} | \Phi_k^{qc} \rangle \quad (107)$$

$$= \sum_n \sum_{n'} B_{nl}^* B_{n'k} \langle g_l^{cl} | g_k^{cl} \rangle \langle n | n' \rangle \quad (108)$$

$$= \sum_n B_{nl}^* B_{nk} \langle g_l^{cl} | g_k^{cl} \rangle. \quad (109)$$

Finally, the differential overlap τ is defined by

$$\tau_{lk} = \langle \Phi_l^{qc} | \dot{\Phi}_k^{qc} \rangle \quad (110)$$

$$= \sum_n \sum_{n'} \left(B_{nl}^* \dot{B}_{n'k} \langle g_l^{cl} | g_k^{cl} \rangle \langle n | n' \rangle + B_{nl}^* B_{n'k} \langle g_l^{cl} | \dot{g}_k^{cl} \rangle \langle n | n' \rangle \right) \quad (111)$$

$$= \sum_n B_{nl}^* \dot{B}_{nk} \langle g_l^{cl} | g_k^{cl} \rangle + B_{nl}^* B_{nk} \langle g_l^{cl} | \dot{g}_k^{cl} \rangle. \quad (112)$$

Using normalized frozen Gaussians, the differential GWP overlap can be expressed by

$$\langle g_l^{cl} | \dot{g}_k^{cl} \rangle = \langle g_l^{cl} | \left(\frac{\partial g_k^{cl}}{\partial q_k} \right) \rangle \dot{q}_k + \langle g_l^{cl} | \left(\frac{\partial g_k^{cl}}{\partial p_k} \right) \rangle \dot{p}_k + \langle g_l^{cl} | \left(\frac{\partial g_k^{cl}}{\partial S_k} \right) \rangle \dot{S}_k \quad (113)$$

Using these expressions, the wave function and the corresponding expectation values can be reconstructed. In principle, the described MCE ansatz is similar to a 2-layer MCTDH ansatz and introduces an additional coefficient to describe the evolution of the weighting of the different trajectories (the here formulated expressions are similar to the expressions described by Shalashilin et al. [132]). In principle this ansatz allows an accurate description of the electronic sub-system on a short time scale with the limitation that the inverted overlap matrix S^{-1} is needed. This operation can be very time-consuming for a large number of trajectories.

Results

5 | Results

In this chapter, the results of the main projects of the thesis will be presented. The first two sections concern methodological topics, while the remaining three sections concern applications to ultrafast energy transfer phenomena.

In detail, the projects will be presented in the following order: (i) the implementation of the Ehrenfest method in a Fortran 90 code, (ii) an exact adiabatic-diabatic mapping procedure for polymeric systems, (iii) the *ab initio* characterization and the ultrafast exciton dynamics of representative oligo-thiophene (OT) fragments using high-level *ab initio* methods and the MCTDH method, (iv) the effect of thermal noise and disorder on the exciton dynamics of oligo-*para*-phenylene vinylene studied by MCTDH and the semi-classical Ehrenfest method and (v) the ultrafast, photoinduced vibrational energy transfer in a DTE-BODIPY system studied by time-resolved spectroscopy and theoretical modeling.

5.1 Implementation of the Ehrenfest Dynamics in a FORTRAN 90 Code

The implementation of the Ehrenfest equations presented in Sec. is done using the FORTRAN 90 language. The reason for using FORTRAN is on the one hand the high number of optimized mathematical functions, e.g., using the BLAS and LAPACK routines and on the other hand the very easy and stable possibility to handle large arrays and array operations. Furthermore, FORTRAN is a well established, widely used and very efficient computer language in natural science. In general, the implementation of the Ehrenfest dynamics for a given system is done in three steps: (i) generation of the initial conditions for n trajectories (ii) independent time-propagation of n trajectories and (iii) calculation of the expectation values by taking an ensemble average over the trajectory distribution. In Fig.8, the program scheme of the Ehrenfest dynamics is shown.

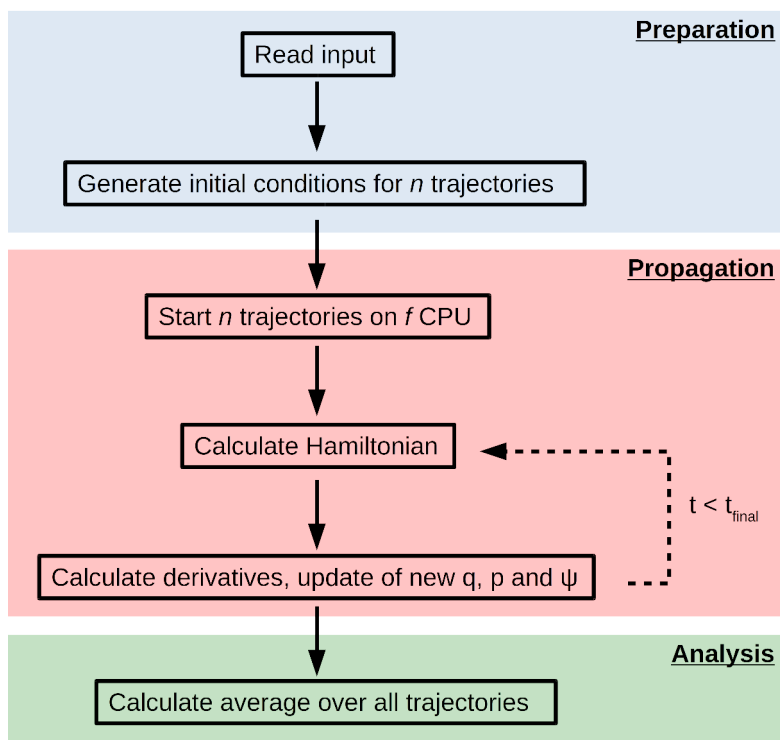


Figure 8: Ehrenfest dynamics program scheme.

We have implemented both the wave function based Ehrenfest equations (Eqn.89 and the density matrix version of Eqn.91). In both schemes, dissipation was added in terms of Langevin forces (Eqn.93) and a dissipative Liouvillian (Eqn.92), respectively. For the initial condition generation of a given system, a Wigner quasi-probability distribution of a harmonic oscillator is obtained from the vibrational ground state wave function [133]. For a pure-state Gaussian, dissipative-free case,

the Wigner quasi-probability distribution $P(q,p)$ for a Gaussian wave function $\Psi(x)$ is given by

$$P(q,p) = \left(\frac{1}{\pi\hbar}\right) \exp\left(-\frac{1}{2\sigma_{qq}^{(0)}}(q - q_0)^2 - \frac{1}{2\sigma_{pp}^{(0)}}(p - p_0)^2\right) \quad (114)$$

centered around q_0 and p_0 and the width

$$\sigma_{qq}^{(0)} = \frac{\hbar}{2m\omega}, \quad \sigma_{pp}^{(0)} = \frac{m\hbar\omega}{2} \quad (115)$$

The numerical values of q and p are generated using an importance sampling procedure. In general, most of the modern computer languages only generate uniformly distributed random numbers. The random number can be transformed to a normal distribution using e.g. the Box-Muller transformation [134] or the Marsaglia polar method [135]. The great advantage of these methods is the fact that for a normal distribution the variance $s = \sqrt{\sigma}$ can be generated from uniformly distributed random numbers with a simple code. Additionally, a temperature dependence variance of the random numbers can be introduced by

$$\Gamma = \frac{\hbar\omega}{2} \coth\left(\frac{\hbar\omega}{2kT}\right) \quad (116)$$

$$\sigma_{qq}^{(0)} = \frac{\Gamma}{m\omega^2}, \quad \sigma_{pp}^{(0)} = m\Gamma \quad (117)$$

This amount to mapping the zero-temperature quantum width of Eqn.115 to a thermal width according to Eqn.116 and 117.

In Fig.9, the effect of temperature on the initial sampling for 3000 trajectories centered around $x_0 = 45^\circ$ is shown. As expected, the width of the Wigner function and therefore the spatial distribution centered around x_0 of the random numbers increases with temperature.

For very low temperatures, a highly local sampling is obtained, whereas for higher temperatures, the sampling gets much broader.

For the propagation part, each trajectory is propagated independently from all other trajectories. This is achieved by starting the propagation n times with the initial conditions of trajectory n generated in step 1. At first, the initial electronic Hamiltonian is calculated using the initial q value for the given trajectory and stored in a matrix. For the time-propagation, whose simplest numerical realization is given by

$$y(t + \Delta t) = y(t) + dy(t)\Delta t \quad (118)$$

where y is a generic quantity (here representing q,p and Ψ), one has to calculate the derivatives of q , p and Ψ . The simplest integration scheme can be realized us-

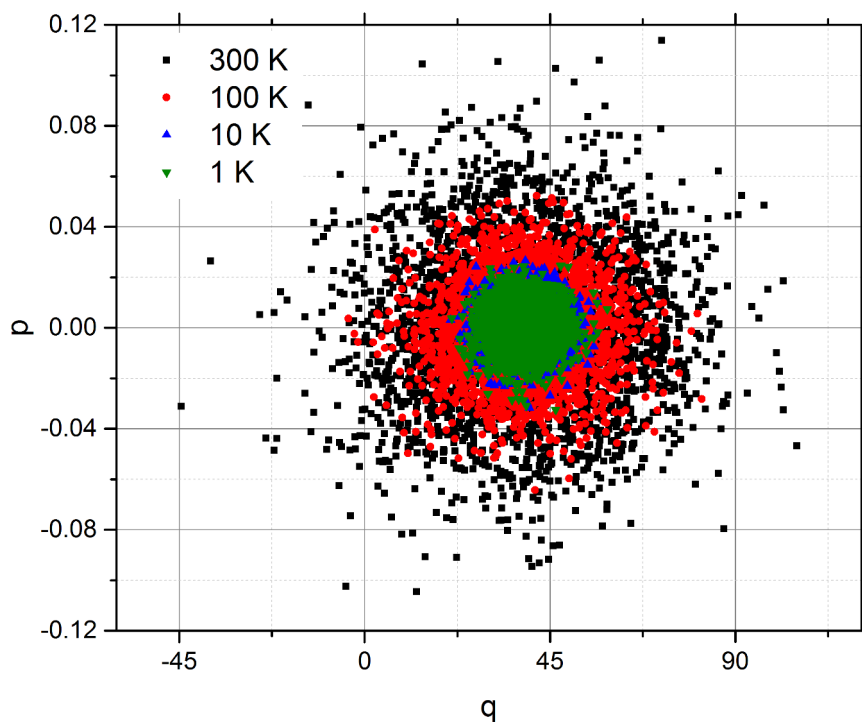


Figure 9: Temperature effect of the initial sampling of a torsional degree θ centered around 40 degrees for 3000 trajectories.

ing an Euler integrator [136, 137] (see Eqn.118). After every integration step, the electronic Hamiltonian is updated using the new q values. In practice, the correct integration can be verified by calculating the norm of the wave function, which should be conserved during the propagation. For the Euler integrator, which is easy to implement, it turns out that the step-size Δt has to be reduced dramatically to be norm-conserving. To use larger step-sizes for each integration step, a higher order integrator has to be used, e.g., Runge-Kutta (RK) [138] 4th/8th order integrator or a different type of integrator such as an Adam-Bashford-Multon (ABM) integrator [137]. In contrast to the RK integration scheme, the ABM integration scheme is a so-called predictor-corrector integration scheme, which uses the information of the previous step to calculate the derivatives for the current step. Furthermore, the step-size is adjusted with respect to a tolerance value. In theory, such an integrator will give very accurate results, but the problem of an adaptive step-size integrator is the tolerance criterion. If this criterion is not fulfilled, the step-size is reduced and the integration step is repeated. For stiff equations, it is possible that the step-size is reduced to very small values and in such a case, the ABM integrator will slow down or in worst case the integration stops. In contrast to the ABM integration scheme, the implemented RK scheme is a fixed step-size scheme (but can be extended to an adaptive step-size scheme with the problems

mentioned before) which guarantees a correct propagation as long as the norm is conserved (norm conservation is used as a convergence criterion). The RK4 and RK8 schemes that we employed are shown in Eqn.119 and Eqn.120 respectively.

$$y(t + \Delta t) = y(t) + \frac{1}{6} (k_1 + 2k_2 + 2k_3 + k_4) \quad (119)$$

with

$$\begin{aligned} k_1 &= \Delta t f(x_n, y_n) \\ k_2 &= \Delta t f\left(x_n + \frac{\Delta t}{2}, y_n + \frac{k_1}{2}\right) \\ k_3 &= \Delta t f\left(x_n + \frac{\Delta t}{2}, y_n + \frac{k_2}{2}\right) \\ k_4 &= \Delta t f(x_n + \Delta t, y_n + \Delta t k_3) \end{aligned}$$

$$y(t + \Delta t) = y(t) + \frac{41k_1}{840} + \frac{34k_6}{105} + \frac{9k_7}{35} + \frac{9k_8}{35} + \frac{9k_9}{280} + \frac{9k_{10}}{280} + \frac{41k_{11}}{840} \quad (120)$$

with

$$\begin{aligned} k_1 &= \Delta t f(x_n, y_n) \\ k_2 &= \Delta t f\left(x_n + \frac{2\Delta t}{27}, y_n + \frac{2\Delta t}{27} k_1\right) \\ k_3 &= \Delta t f\left(x_n + \frac{\Delta t}{9}, y_n + \frac{k_2}{36} (k_1 + 3k_2)\right) \\ k_4 &= \Delta t f\left(x_n + \frac{\Delta t}{6}, y_n + \frac{\Delta t}{24} (k_1 + 3k_3)\right) \\ k_5 &= \Delta t f\left(x_n + \frac{5\Delta t}{12}, y_n + \frac{\Delta t}{48} (20k_1 - 75k_3 + 75k_4)\right) \\ k_6 &= \Delta t f\left(x_n + \frac{\Delta t}{2}, y_n + \frac{\Delta t}{20} (k_1 + 5k_4 + 4k_5)\right) \\ k_7 &= \Delta t f\left(x_n + \frac{5\Delta t}{6}, y_n + \frac{\Delta t}{108} (-25k_1 + 125k_4 - 260k_5 + 250k_6)\right) \\ k_8 &= \Delta t f\left(x_n + \frac{\Delta t}{6}, y_n + \Delta t \left(\frac{31}{300} k_1 + \frac{61}{225} k_5 - \frac{2}{9} k_6 + \frac{13}{900} k_7\right)\right) \\ k_9 &= \Delta t f\left(x_n + \frac{2\Delta t}{3}, y_n + \Delta t \left(2k_1 - \frac{53}{6} k_4 + \frac{704}{45} k_5 - \frac{107}{9} k_6 + \frac{67}{90} k_7 + 3k_8\right)\right) \\ k_{10} &= \Delta t f\left(x_n + \frac{\Delta t}{3}, y_n + \Delta t \left(-\frac{91}{108} k_1 + \frac{23}{108} k_4 - \frac{976}{135} k_5 + \frac{311}{54} k_6 - \frac{19}{60} k_7 + \frac{17}{6} k_8 - \frac{1}{12} k_9\right)\right) \\ k_{11} &= \Delta t f\left(x_n + \Delta t, y_n + \Delta t \left(\frac{2383}{4100} k_1 - \frac{341}{164} k_4 + \frac{4496}{1025} k_5 - \frac{301}{82} k_6 + \frac{2133}{4100} k_7 + \frac{45}{82} k_8 + \frac{45}{164} k_9 + \frac{18}{41} k_{10}\right)\right) \end{aligned}$$

To improve the integration scheme, a mixed RK scheme is used: for the integration of q and p , a RK integrator 4th order is used, whereas a more accurate RK 8th order is used for the integration of the electronic wave function. In Fig.10, the effect of the integrator order on the error of the integration is illustrated. as mentioned above, the advantage of using the fixed step-size scheme is to avoid the reduction of step-size as it is possible in the ABM scheme. Furthermore, the implementation of the Langevin formalism is very simple for fixed step-size while for variable step size the noise term has to be rescaled properly every step.

For the Euler integrator, the calculation of the derivatives is done once, including the calculation of the friction and the noise term. In contrast to the Euler integra-

tor, the RK 4th order scheme will calculate the derivatives four times. Therefore, one has to include this aspect in the fluctuation term, as now explained.

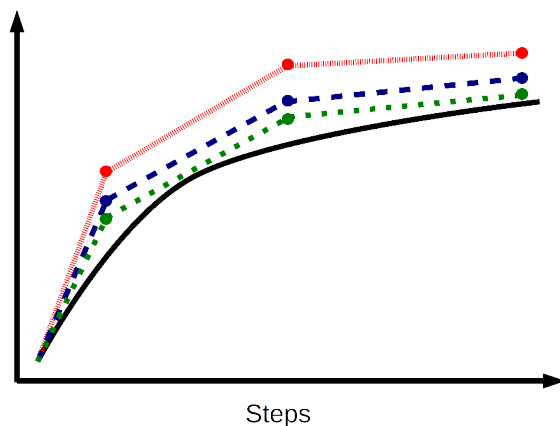


Figure 10: Illustration of the integration order, (red) Euler, (blue) RK 4, (green) RK 8 and (black) analytic function with the fixed step-size h .

The time-step Δt of the fluctuation term corresponds to the time between the sequential calls of the integrator. For a fourth order integration scheme, which calculates the derivatives four times, the time-step between these calls is $\Delta\tau$ and therefore, the original Δt has to be set to $\Delta t = \tau/4$. Using the mixed integration scheme, one can achieve quite good accuracy even for large integration steps (in general, the step-size is limited to the fastest component, which is in the most cases the electronic component). Therefore, the step-size that was typically used is in the range of $\Delta t = 0.1-1.0$ a.u. $\approx 0.0024-0.024$ fs. As mentioned in Sec.5.1, the Ehrenfest dynamics can also be performed using a density matrix approach, e.g., to calculate dissipative dynamics. For a non-dissipative system, the mixed RK scheme is accurate enough, whereas for the dissipative system, the mixed RK is not sufficient any more (at least in theory, the RK scheme should give the exact results for very small step-sizes but this is not practicable anymore). This failure can be explained by the stability of the RK integration scheme, which is not high for dissipative systems [139]. To calculate dissipative dynamics, an asynchronous leap-frog scheme [140] as shown in Eqn.121 is used for the integration of the wave function, which is more stable for dissipative systems than the RK scheme. Nevertheless, the norm-conserving numerical integration of a dissipative open-quantum system is quite challenging.

$$\begin{aligned} \rho(t + \Delta t) &= \rho(t) + \kappa(t) \frac{\Delta t}{2} \\ \kappa &= \kappa + 2 \left(\frac{1}{i\hbar} [H(t), \rho] - \kappa \right) \\ \rho(t + \Delta t) &= \rho(t + \Delta t) + \kappa(t) \frac{\Delta t}{2} \end{aligned} \tag{121}$$

κ has to be initialized in the beginning using $\kappa = \frac{1}{i\hbar}[H(t_0), \rho(t_0)]$.

After the successful propagation of all trajectories, the expectation values of the observables of interest are calculated in a third step. For this purpose, the average of every observable is calculated, which are identical to the quantum expectation values as stated by the Ehrenfest theorem.

One of the biggest advantages of the Ehrenfest dynamics over the full quantum MCTDH method is the computationally cheap propagation of the coordinates and the wave function, which can be used to calculate rather big systems with many degrees of freedom and electronic states. Furthermore, using the independent propagation scheme for each trajectory, many trajectories can be calculated at once on a large computer cluster. Nevertheless, the Ehrenfest dynamics is a semi-classical method, which is not able to reconstruct all properties and observables like in the full quantum picture e.g. information about the electronic coherence is lost.

5.2 Exact Adiabatic-to-Diabatic Transformation

In order to perform quantum dynamics using the Ehrenfest or MCTDH ansatz, an appropriate model with an adequate representation has to be chosen. In principle, the adiabatic or a suitable diabatic representation can be used to describe the phenomena under study. Both representations are equivalent but the interpretation of diabatic results is more intuitive, especially if a site-based representation is chosen. One of the main features of a diabatic representation are the non-zero off-diagonal coupling elements for a given Hamiltonian (see the discussion in Sec.4.2). This aspect is one of the key features for all models of this work and therefore, all models and methods used and developed in this thesis are based on the diabatic representation such that the implementation of non-adiabatic couplings (see Sec.4.2) is avoided. Thus, all potential energy surfaces (PES) have to be expressed in the diabatic basis. The PES obtained from *ab initio* calculations are in fact adiabatic PES and therefore, have to be mapped onto a diabatic representation. One possible and exact adiabatic-to-diabatic mapping procedure has been developed by Binder et al. [32, 141]. The resulting diabatic PES can then be fitted by a suitable functional form and used in the quantum dynamical calculations.

In the following section, a brief description of the adiabatic-diabatic mapping description for polymeric systems will be given. In general, the mapping procedure developed by Binder et al. [141] works for any kind of Hückel-type system with some restrictions. First, a Hamiltonian of the system is needed which is expressed in terms of separated units, which are given by different potentials and in terms of ground and excited states, e.g., a Frenkel type Hamiltonian. Second, an adiabatic PES cut along the coordinate of interest is needed. Third, the correct electronic states have to be identified e.g. the lowest Frenkel excitonic states have to be known.

Assuming a polymeric system with a steric defect centered in the middle of the system, the corresponding potential matrix can be constructed, as illustrated in Fig.11.

Based on this matrix and the adiabatic PES, the diabatic potential matrix can be calculated. In Fig.12, the complete adiabatic-diabatic transformation procedure is illustrated. Starting with two adiabatic states λ_t and λ_s at a specific geometry (typical the Hückel geometry), the adiabatic potential matrix can be constructed. The diabatic states can be seen as eigenvalues of the Frenkel type matrix which can in turn be re-diagonalized. Using these two states and the ground-state information, the Frenkel type matrix can be constructed by mapping the adiabatic

$$V = c_G 1 + \left(\begin{array}{cccccccc|c} d & w_0 & & & & & & & 0 \\ w_0 & d & w_0 & & & & & & \\ & \ddots & \ddots & \ddots & & & & & \\ & & w_0 & d & w_0 & & & & \\ & & & w_0 & \tilde{d} & w & & & \\ & & & & w & \tilde{d} & w_0 & & \\ & & & & & w_0 & d & w_0 & \\ & & & & & & \ddots & \ddots & \ddots \\ & & & & & & & w_0 & d & w_0 \\ & & & & & & & & w_0 & d \\ \hline 0 & & & & & & & & & d_G \end{array} \right)$$

Figure 11: Potential matrix representation of a polymeric system with a structural defect. Note that the diagonal and off diagonal matrix elements located at the defect position (\tilde{d} and w) differ from the remaining values (d and w_0).

potential matrix onto the Frenkel type matrix. A diagonalization of this Frenkel matrix will result in the two input eigenvalues and all other eigenvalues of the system. Applying this procedure to the results of an adiabatic PES, an exact diabatic PES can be obtained. The new diabatic PES can be fitted to a functional form and used for further applications e.g. quantum dynamical calculations.

This procedure has been employed to construct the potential surfaces for the OT and OPV systems under study.

$$\begin{array}{c}
 V_{adiabatic} = \left(\begin{array}{cccccccc|c}
 * & & & & & & & & 0 \\
 & \ddots & & & & & & & \\
 & & * & & & & & & \\
 & & & \boxed{\lambda_t} & & & & & \\
 & & & & * & & & & \\
 & & & & & \ddots & & & \\
 & & & & & & * & & \\
 & & & & & & & \boxed{\lambda_s} & \\
 & & & & & & & & * \\
 & & & & & & & & \ddots \\
 & & & & & & & & & * \\
 0 & & & & & & & & & \lambda_0
 \end{array} \right) \\
 \\
 \downarrow \text{Map} \\
 V = c_G 1 + \left(\begin{array}{cccccccc|c}
 d & w_0 & & & & & & & 0 \\
 w_0 & d & w_0 & & & & & & \\
 & \ddots & \ddots & \ddots & & & & & \\
 & & w_0 & d & w_0 & & & & \\
 & & & w_0 & \tilde{d} & w & & & \\
 & & & & w & \tilde{d} & w_0 & & \\
 & & & & & w_0 & d & w_0 & \\
 & & & & & & \ddots & \ddots & \ddots \\
 & & & & & & & w_0 & d & w_0 \\
 & & & & & & & & w_0 & d \\
 0 & & & & & & & & & d_G
 \end{array} \right) \\
 \\
 \downarrow \text{Diagonalization} \\
 V_{adiabatic} = \left(\begin{array}{cccccccc|c}
 \lambda_n^{pred} & & & & & & & & 0 \\
 & \ddots & & & & & & & \\
 & & \lambda_{t+1}^{pred} & & & & & & \\
 & & & \boxed{\lambda_t} & & & & & \\
 & & & & \lambda_{t-1}^{pred} & & & & \\
 & & & & & \ddots & & & \\
 & & & & & & \lambda_{s+1}^{pred} & & \\
 & & & & & & & \boxed{\lambda_s} & \\
 & & & & & & & & \lambda_{s-1}^{pred} \\
 & & & & & & & & \dots \\
 & & & & & & & & \lambda_1 \\
 0 & & & & & & & & \lambda_0
 \end{array} \right)
 \end{array}$$

Figure 12: Illustration of the adiabatic-diabatic transformation procedure from electronic structure information to a Frenkel type model (adopted from Ref.[141]).

5.3 Exciton Dynamics on a Minimal Oligo-Thiophene Lattice

Polythiophene (PT) and its derivatives like Poly(3-hexylthiophene) (P3HT) are promising materials for the development of new types of organic solar cells, organic light emitting diodes (OLED) or sensors [142–144]. Interestingly, PT is rarely used commercially although it shows some remarkable properties such as fluorescence or semi-conductivity. Depending on the chain length, the macromolecular structure and the doping/substituents, the photochemical properties (fluorescence wavelength or the HOMO-LUMO band-gap) can be tuned [145]. In addition, the manufacturing process of PT is simple and offers a wide range of potential applications. First studies have been done by M. Ree et al. and N. Robertson et al. [87, 146] to demonstrate the applicability of PT as a material for organic photovoltaics or by R. A. J. Janssen et al. [147] using PT as a donor molecule for a bulk heterojunction solar cell in combination with fullerene derivatives as an acceptor material. In order to understand the physical processes in the solar energy conversion for these type of systems, several experimental and theoretical studies have already been performed by a number of groups, to characterize the ultrafast transport processes taking place in these systems [66, 148–150]. In case of donor-acceptor type solar cells, the efficiency of the solar energy conversion correlates with the ratio of donor and acceptor material and the dispersity, which can be controlled during the manufacturing process.

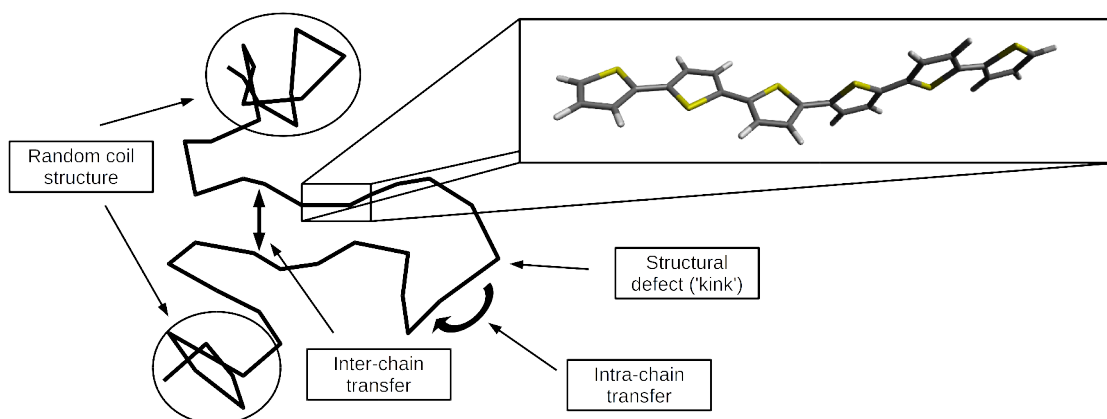


Figure 13: Illustration of a typical PT polymer built from n thiophene monomer units. The black solid line represents the polymer backbone, with different areas (i) random coiled and (ii) linear structure. The intra- and inter-site transfer mechanism are indicated by black arrows.

Of course, the relevant material is the most important parameter for an efficient conversion, and therefore, many materials are used to find the best candidates.

Since polythiophene is one of the very promising materials, a lot of effort is underway, to understand the conversion processes in polythiophene. As mentioned in Sec.3.2, several steps take place in the donor material until a successful charge separation happens. Probably the most difficult step to model is the exciton migration after a FC excitation. Different schemes have been introduced in the last years to describe this process correctly e.g. exciton relaxation followed by a hopping process [13, 151, 152] or a compact exciton packet dynamics [33, 78, 89, 153]. As shown in Fig.13, the observed dynamics strongly depend on the main exciton transfer mechanism: intra-chain (a coherent EET of „surfing“ type) [154, 155] transfer or inter-chain (hopping type) transfer [24, 156, 157].

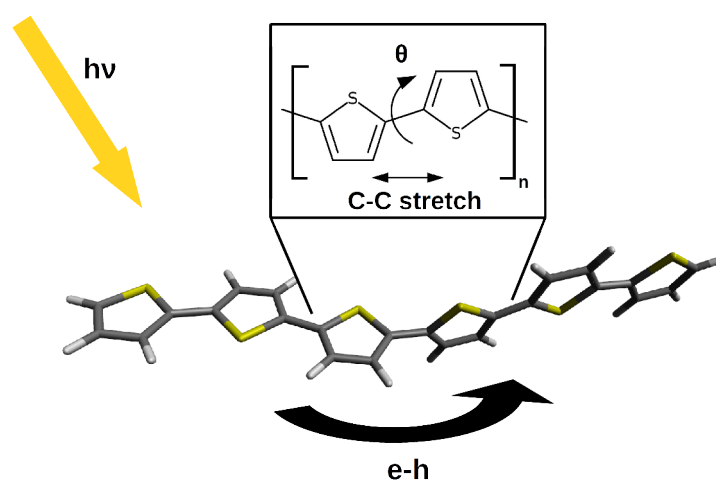


Figure 14: Exciton dynamics on an oligo-thiophene lattice exhibiting a torsional defect after photoexcitation. Important coordinates are shown by arrows in the inset.

The main transfer mechanism is strongly governed by several aspects: the polymer conformation (ordered/disordered), steric aspects (polymeric defects) and the electronic properties of the system [82]. The first two aspects can be controlled in the production process, while the last aspect strongly depends on the type of system. In general, the intra-chain exciton coupling is described as a J -type aggregate and is strongly correlated to the overlap of the conjugated π -system, while an inter-site transfer can be described by a H -type aggregate [155, 158, 159]. A typical intra-chain coupling is on the order of ≈ 0.1 - 1.0 eV while the inter-chain coupling is on the order of ≈ 0.05 - 0.2 eV. In addition, the intra-chain mechanism is influenced by steric defects, which can be 'healed' to some extent, whereas the inter-chain mechanism depends on the distance between the polymer chains. Furthermore, the type of exciton, Frenkel, Wannier-Mott or CT exciton (see Chp.3), plays an important role for a correct description. As shown in Chp.3, it is difficult to find a model to describe all aspects of the transfer and therefore, the aim of this

work was to develop a model Hamiltonian describing the intra-chain Frenkel and CT exciton dynamics in a PT-chain in the presence of a geometric defect. The molecular structure, the geometric defect and the active degrees of freedom of the model are illustrated in Fig.14. The model represents a PT hexamer (or a 20-mer in our most recent calculation), which can be seen as part of a linear PT chain, in either a Frenkel or a Frenkel + CT exciton basis (a detailed description of the model is given in Sec.5.3.1, and 5.3.2). This model describes the exciton dynamics on this chain using a relaxed wave function on a sub-fragment of the system as an initial condition.

The oligomer fragments under consideration can be taken to be examples of J-aggregate systems, which exhibit a head-to-tail arrangement of monomer units. A first characterization of J-aggregates has been given by Jelly et al. [158] and originally describes the self-association of dyes in solution or at a solid-liquid interface resulting in a spectral shift. Depending on the shift – bathochromic or hypsochromic – a definition of J or H type aggregates is given. This shift is a result of coupled transition dipole moments and has been observed for many types of systems [12].

While the J-type aggregate property suggests a delocalization over the whole polymer, in practice delocalization is limited due to structural defects or conjugation breaks. In this context the concept of so-called „spectroscopic units“ has been used which explains that delocalization is restricted to several neighboring monomer units. Typically, the photogenerated exciton is delocalized across 5-15 monomer units. Despite its intuitive appeal, this concept is still much debated to date [43].

5.3.1 Quantum Chemical Method and Model

To describe the exciton dynamics of a reasonable level of theory, an appropriate model with a correct parametrization has to be used. Based on the assumption that the diffusion process after FC excitation is strongly correlated to the overlap of the π -system, the model Hamiltonian used for the dynamics will introduce a torsional and bond-length dependent exciton transfer [160–162]. This assumption is in turn correlated to the flexibility of the polymer backbone which is defined by the torsional angle between two monomer units and the distance of two monomer units. As shown in Fig.15, n -PT is built from n thiophene monomer units, which are linked by a 1-3 carbonyl bond. For steric reasons, the S-C-C'-S' torsional angle is 168° in the electronic ground state and 180° in the first excited state [163–165]. This value is related to the sulfur-sulfur repulsion or to be more precise, to the free electron pair of the sulfur which is localized in very diffuse orbitals. In the

ground state, the system contains a conjugated π -system over the full chain. This π -system is essential for a good conductivity and can be disturbed by a conjugation break (as illustrated in Fig.15 between monomer 3 and 4). As mentioned before, this torsional coordinate has been considered in the model Hamiltonian as an important coordinate for the energy transfer efficiency after photoexcitation, since the overlap of the π -system and the presence of a torsional defect can strongly influence the excitation transfer. To improve the model, the C-C distance coordinate between two monomer units has been chosen as an additional active coordinate. To parametrize the torsional and the C-C distance (also called bond-length alternation (BLA)) coordinates, high level *ab initio* calculations are performed using the MP2 and ADC(2) method as implemented in the TURBOMOLE 6.4 program package. The main advantage of the ADC(2) method over standard TDDFT calculations is the correct description of double-excitations and charge-transfer states, which are often underestimated by TDDFT. An alternative method to ADC(2) with very similar results would be CC2, but CC2 has the disadvantage that the excitation energies are obtained as eigenvalues of a non-hermitian Jacobi matrix in contrast to ADC(2), where the excitation energies are obtained as eigenvalues of a hermitian matrix. To be consistent, MP2 has been used for ground state optimization whereas ADC(2) is used for excited state optimizations and the calculations of the PESs. Nevertheless, the results of ADC(2) and CC2 are very similar, but for both methods, the computational costs are very high and therefore, all calculation were performed using extensive parallelization.

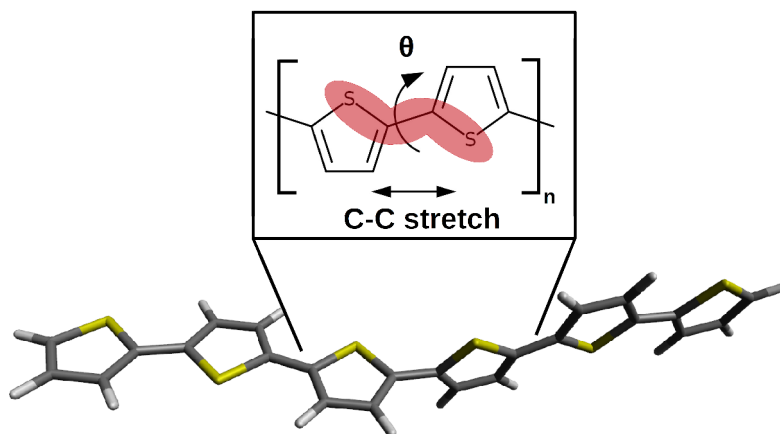


Figure 15: Oligo-thiophene unit described in the quantum dynamics. The site-correlated coordinates (torsional and BLA) are indicated by arrows. The red colored area defines the torsional angle.

Due to the $\approx n^5$ scaling of ADC(2) and MP2 with the number of basis function, the system size for the parametrization of the torsional and the BLA coordinates has been limited to a PT octamer (in order to use the appropriate basis set def2-

TZVP). This system size is already able to describe the excitonic band character of a larger system (see Fig.20). For the coordinates, one-dimensional cuts along the PES have been performed based on the relaxed ground state geometry. The final parametrization has been performed by an exact adiabatic-diabatic transformation of the quantum chemical results according to the procedure described in Sec.5.2.

5.3.2 Model Hamiltonian

For the quantum dynamics, either a Frenkel Hamiltonian is used, or else or a Merrifield type Hamiltonian comprising a full $e-h$ basis [99] (see Chp.3). Each site ξ is defined in terms of a thiophene monomer unit and carries a site-correlated torsional and bond-length coordinate. (I.e., these modes couple simultaneously to two neighboring thiophene units). The basis of a general $e-h$ state is given by $|\nu_e\mu_h\rangle \equiv |\nu\mu\rangle$ where the electron is located at site $\nu_e = \nu$ while the hole is located on site $\mu_h = \mu$. This description can be compared to the valence/conduction band picture, where an electron is created in the conduction band at site ν while a hole is left in the valence band at site μ . All other states remain in their ground state. This will cause a different dynamics for the coordinates. The general form of the vibronic Hamiltonian is given by

$$H = \sum_{\nu\mu} \sum_{\nu'\mu'} H_{\nu\mu,\nu'\mu'} |\nu\mu\rangle \langle \nu'\mu'| \quad (122)$$

with

$$\begin{aligned} H_{\nu\mu,\nu'\mu'} = & \delta_{\nu\nu'} \delta_{\mu\mu'} (H_{\nu\mu,\nu'\mu'}^{\text{intr}} + H_{\nu\mu,\nu'\mu'}^{\text{BLA}} + H_{\nu\mu,\nu'\mu'}^{\text{tors}} + H_{\nu\mu,\nu'\mu'}^{\text{bath}}) \\ & + \delta_{\nu\mu} \delta_{\nu'\mu'} H_{\nu\mu,\nu'\mu'}^{\text{Frenkel}} + H_{\nu\mu,\nu'\mu'}^{\text{CT}} \end{aligned} \quad (123)$$

where all terms can depend on the vibrational coordinates. The first four terms are diagonal in the $e-h$ basis and correspond to (i) the intrinsic electron-hole interaction, (ii+iii) vibronic contributions related to the BLA and the torsional coordinate and (iv) a harmonic oscillator bath acting as a source of dissipation. The terms $H_{\nu\mu,\nu'\mu'}^{\text{Frenkel}}$ and $H_{\nu\mu,\nu'\mu'}^{\text{CT}}$ represent Frenkel type and CT type coupling terms and are off-diagonal. The CT transfer integrals couple CT excitons to Frenkel excitons and among each other.

This Hamiltonian is comparable to a quasi-diabatic vibronic coupling Hamiltonian with a diagonal representation of the nuclear kinetic energy and potential type couplings. As explained in Ref.[32, 141] an exact adiabatic-diabatic transformation of the *ab initio* potentials is performed to map the electronic structure information onto this Hamiltonian (see Sec.5.2). The intrinsic $e-h$ pair interaction is given by

$$H_{\nu\mu,\nu'\mu'}^{\text{intr}} = \delta_{\nu\nu'}\delta_{\mu\mu'}\left(e_0 - \frac{1}{4\pi\epsilon_0\epsilon_r r_{\nu\mu}}\right) \quad (124)$$

where $r_{\nu\mu}$ is the e - h distance as a function of the sites $(\nu\mu)$, $r = |\nu - \mu|r_{ru} + r_0$, with r_{ru} the repeat unit length, and r_0 the intrinsic e - h distance for a Frenkel exciton. The binding energy e_0 for a localized e - h pair is set to zero, such that $H_{\nu\nu,\nu\nu} = 0$. The relative permittivity ϵ_r has been set to 4 (as given in Ref.[145]). The second and the third term of Eqn.123 correspond to the excitonic potentials including the monomer ground (G) and excited (E) states potentials for the site-correlated torsional and the BLA coordinate. For the site-correlated coordinates, the following expression is used

$$H_{\nu\mu,\nu'\mu'}^{\text{vibr}}(z_{\xi,\xi+1}) = \delta_{\nu\nu'}\delta_{\mu\mu'} \sum_{\xi=1}^{N_{\text{sites}}-1} \left[-\frac{1}{2} \frac{\partial^2}{\partial z_{\xi,\xi+1}^2} + V^G(z_{\xi,\xi+1}) + (\delta_{\nu,\xi} + \delta_{\nu,\xi+1}) \left(V^E(z_{\xi,\xi+1}) - V^G(z_{\xi,\xi+1}) \right) \right] \quad (125)$$

where $z_{\xi,\xi+1} \in \{x_{\xi,\xi+1}, \theta_{\xi,\xi+1}\}$, i.e. contributions for the BLA and torsional coordinates will be summed over. N_{sites} corresponds to the number of monomer units, V^G and V^E denote the effective ground/excited state potential that are composed of combinations of ground and excited-state monomer potentials. For a correct description of the finite lattice and to avoid edge effects, an edge potential was added as described in Ref.[166].

In contrast to the site-correlated system coordinates, the bath Hamiltonian is coupled to one torsional coordinate, to minimize the computational effort with a maximum effect. The bath Hamiltonian is adopted from a Caldeira-Leggett model and given by

$$H_{\nu\mu,\nu'\mu'}^{\text{Bath}} = \delta_{\nu\nu'}\delta_{\mu\mu'} \sum_{i=1}^{N_B} \left[-\frac{1}{2} \frac{\partial^2}{\partial x_{B,i}^2} + \frac{1}{2} \omega_{B,i}^2 \left(x_{B,i} - \frac{c_{B,i}}{\omega_{B,i}} \theta \right)^2 \right] \quad (126)$$

where $c_{B,i}$ are the system-bath couplings obtained from an Ohmic spectral density $c_{B,i} = (2\omega\Delta\omega J_{\text{Ohm}}(\omega)/\pi)^{1/2}$ with the discrete frequency interval $\Delta\omega$ determining the Poincaré recurrence time $t_{PC} = 2\pi/\Delta\omega$. The Ohmic spectral density is given by $J_{\text{Ohm}} = 2\gamma\Delta\omega e^{-\omega/\Lambda}$ with the friction coefficient γ and the cut-off frequency Λ . Finally, the site-to-site couplings are defined as next-neighbor couplings depending only on the torsional coordinate. Due to the fact that well localized Frenkel type excitons and delocalized e - h pairs have to be considered, two different types of coupling will be defined. First, the Frenkel type coupling is defined by

$$H_{\nu\mu,\nu'\mu'}^{\text{Frenkel}} = \delta_{\nu\mu}\delta_{\nu'\mu'} (\delta_{\nu',\nu+1} J_{\text{Frenkel}}(\theta) + \delta_{\nu',\nu-1} J_{\text{Frenkel}}(\theta)) \quad (127)$$

whereas the e - h coupling is defined by

$$H_{\nu\mu,\nu'\mu'}^{CT} = \delta_{\nu\nu'}(\delta_{\mu',\mu+1}t_{CT}(\theta) + \delta_{\mu',\mu-1}t_{CT}(\theta)) + \delta_{\mu\mu'}(\delta_{\nu',\nu+1}t_{CT}(\theta) + \delta_{\nu',\nu-1}t_{CT}(\theta)) \quad (128)$$

with the transfer integral $t_{CT} = t_0 \cdot \cos(\theta)$ with $t_0=2.6$ eV [167]. As mentioned above, the parameters needed for this Hamiltonian are obtained by high-level quantum chemical calculations and an exact adiabatic-diabatic transformation. In the following section, the quantum chemical results and the parametrization of the coordinates are presented.

5.3.3 Electronic Structure Calculations

All quantum chemical results presented in this section have been performed with the TURBOMOLE 6.4 program package [168, 169] using the MP2 and ADC(2) method combined with the def2-TZVP basis set [170–173]. This combination is known to give accurate results, especially the results for excited states are known to be more precise than results obtained by TDDFT even though the relevant high-level methods require more computational effort [174].

Before calculating the required PES cuts, a detailed structural analysis of the molecule has been performed including an analysis of the first 10 excited states. To obtain the relaxed ground and excited state geometries, a geometry optimization at the MP2 level has been performed for the ground state.

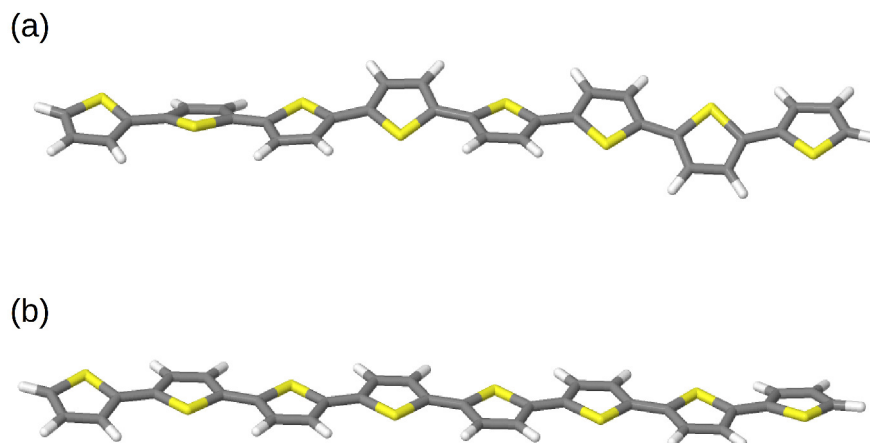
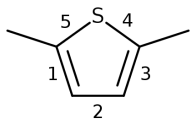


Figure 16: (a) Relaxed ground and (b) excited state structure of the oligo-thiophene studied using *ab initio* methods.

Based on this structure, the relaxed structure of the first excited state is calculated by geometry optimization using ADC(2). In Fig.16, the corresponding structures are shown. As one would expect, both structures are linear with some visible

differences: the relaxed ground state structure shows a twisted polymer chain with a torsional angle of $\approx 160^\circ$ which is in good agreement with experimental results [175–177]. Furthermore, an alternating ‘up-down’ structure of the thiophene rings is observable resulting in an distorted but still symmetric structure. In contrast to this twisted structure, the first excited state structure is almost planar with a S-C-C’-S’ torsional angle of $\approx 180^\circ$. Such a planarization in the excited state after photoexcitation is a well known phenomena of conjugated systems [178]. In Tbl.1, the bond-length of the first four thiophene units is shown for the ground and the first excited state (due to the symmetry of the system and for clarification reasons).

Table 1: Bond length and monomer-monomer distance values of the oligo-thiophene for the first 4 monomer units. The excited state values are given in parenthesis. All values are given in Å.



Bond number	Unit				Distance $\xi, \xi + 1$	
	Unit 1	Unit 2	Unit 3	Unit 4		
1	1.38 (1.38)	1.39 (1.40)	1.39 (1.41)	1.39 (1.42)	1-2	1.442 (1.432)
2	1.42 (1.40)	1.40 (1.39)	1.40 (1.38)	1.40 (1.37)	2-3	1.437 (1.412)
3	1.38 (1.39)	1.39 (1.40)	1.39 (1.41)	1.39 (1.42)	3-4	1.436 (1.397)
4	1.72 (1.73)	1.73 (1.74)	1.73 (1.74)	1.73 (1.75)	4-5	1.436 (1.391)
5	1.72 (1.71)	1.73 (1.73)	1.73 (1.74)	1.73 (1.75)		

The bond-length values given in Tbl.1 clearly show the typical change of single and double bonds character after photoexcitation, which is also observable in quinone-like systems. In general, it is observable that the carbon-sulfur bonds are not strongly affected by the photoexcitation, in contrast to all carbon-carbon bonds, which indicates a contribution of the conjugated π -system. Furthermore, the monomer units located in the middle of the chain are affected much more strongly than the outer ones. By analyzing only the monomer-monomer bond-length for the ground state and the excited state, the typical trapping effect after photoexcitation can be demonstrated. As shown in Fig.17, the relative BLA values for the ground state are less diverging for the different bonds, while in the excited state, a much more pronounced change is observable resulting in a much shorter bond-length centered in the middle of the chain compared to the outer ones.

As demonstrated, this trapping effect of the monomer-monomer bond-length is strongly correlated to the electronic excitation. To analyze the electronic excitations on a monomer resolved level, the transition densities for the first 10 excited singlet states are calculated based on the relaxed excited state geometry. For this analysis, the single-particle transition density matrix in the atomic orbital (AO) representation is used [179]

$$\rho_{nm}^{(k)} = \langle k | \hat{b}_n^\dagger \hat{a}_m | 0 \rangle \quad (129)$$

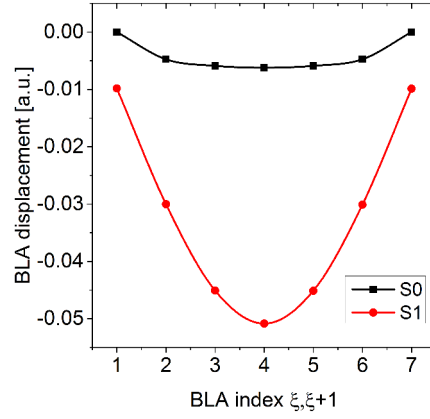


Figure 17: BLA values of the relaxed ground (black) and excited state (red) structure. The BLA index represents the bond between monomer site ξ and $\xi+1$.

with the annihilation operator \hat{a}_m removing an electron from the ground state $|0\rangle$ in the m -th AO and the creation operator \hat{b}_n^\dagger creating an electron in the excited state $\langle k|$ in the n -th AO. The transition density $\Omega_{\nu\mu}^{(k)}$ is obtained by summing components of $\rho_{mn}^{(k)}$ over defined fragments

$$\Omega_{\nu\mu}^{(k)} = \frac{1}{2} \sum_{n \in \nu} \sum_{m \in \mu} (\rho^{(k)} S)_{nm} (S \rho^{(k)})_{nm} \quad (130)$$

with the overlap matrix S in the AO basis. This analysis allows to characterize the excitation in terms of electrons and holes and also to evaluate the spatial distribution σ of the excitation. This is important for the further parametrization, since only Frenkel type excitonic states should be considered in the dynamics. As shown for the so obtained transition density in Fig.18, the excitations show a very systematic pattern.

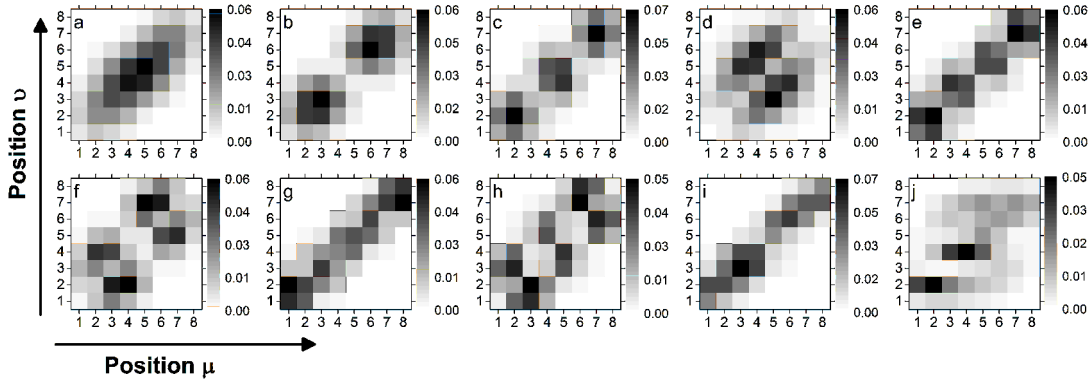


Figure 18: Transition density of the first 10 excited singlet (a - j) states. The x-axis corresponds to the position of the electron μ and y-axis corresponds to the position of the hole ν . The deviation of the spatial distribution for the first three Frenkel excitonic states is $\sigma_{S1} = 1.4$, $\sigma_{S2} = 1.7$ and $\sigma_{S3} = 1.5$.

In general, one can distinguish between well localized excitations, or Frenkel-type excitons, and charge-transfer (CT) excitations by analyzing the electron-hole distribution. For localized excitations e.g. S_1 , a strong on-diagonal transition density is observed, whereas for CT states e.g. S_3 , a strong off-diagonal transition density is observed. Furthermore, the non-CT states show a particle-in-the-box pattern with an increasing number of nodes which is clearly observable for the states S_1 , S_2 , S_3 , S_5 & S_7 . These states seem to belong to the same Frenkel excitonic manifold. The spatial distribution of the first three excited states proves the Frenkel-type character for these states. As explained in the caption of Fig.18, the spatial distribution is in the range of 1.4-1.7, which indicates a very compact excitation typical for Frenkel-type excitons. As shown in Tbl.2, the corresponding oscillator strengths also indicate a non-CT character for these states, whereas the oscillator strength for the CT states is very small or almost zero. Additionally, these numbers also indicate the typical features of a J-aggregate, where the lowest excitonic state of a J-aggregate has a high oscillator strength whereas all other excitonic states belonging to the same manifold only have a very low one.

Table 2: Singlet excitation energies of oligo-thiophene.

State	S_1	S_2	S_3	S_4	S_5
Exc. energy [eV]	3.22	3.57	3.92	4.01	4.24
Oscil. strength	2.81	$5.94 \cdot 10^{-4}$	0.28	$1.21 \cdot 10^{-5}$	$6.48 \cdot 10^{-4}$
State	S_6	S_7	S_8	S_9	S_{10}
Exc. energy [eV]	4.27	4.54	4.59	4.77	4.86
Oscil. strength	$1.60 \cdot 10^{-7}$	0.12	$1.09 \cdot 10^{-4}$	$9.99 \cdot 10^{-3}$	$3.30 \cdot 10^{-2}$

Another indication of the particle-in-the-box behavior of the excited states is given by analyzing the center-of-mass population of the transition density for the lowest excitonic states. The center-of-mass population is defined as

$$\Omega_{\xi}^{CM} = \sum_{\nu, \mu=1} \Omega_{\nu\mu} \Big|_{\nu+\mu=2\xi}. \quad (131)$$

ν and μ describe the position of electron and hole on the polymer lattice, the transition density is given by $\Omega_{\nu\mu}$ and the center-of-mass index ξ defines the center-of-mass position in terms of monomer units.

The resulting center-of-mass distribution $\Omega_{\nu\mu}^{CM}$ is shown in Fig.19. As expected, a node-less distribution is found for the lowest excited state, whereas the second and the third state show one or two nodes, respectively. For these excited states, the center-of-mass distribution is almost symmetric, which is related to the symmetric

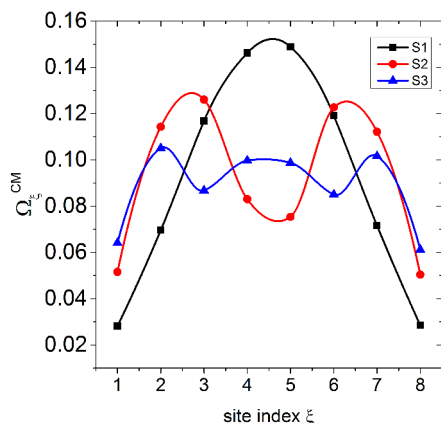


Figure 19: *Ab initio* center of mass population of oligo-thiophene for the first three Frenkel-type excited states.

structure of the oligo-thiophene fragment. To verify whether the oligomer is able to represent a polymeric system or if the chosen system is too small, the excitation energies for different chain lengths are calculated. In theory, a decrease of the excitation energy with increasing number of monomer units should be observed, resulting in a band-type structure of semi-conducting systems. As shown in Fig.20 for the first five electronic states, the described decrease of excitation energy with increasing system size is indeed observable.

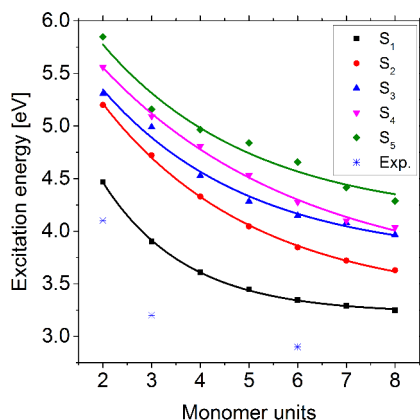


Figure 20: Dependency of the excitation energy on the chain length. The experimental values for selected chain lengths are given by blue stars [180–182].

Especially the lowest electronic state shows the typical trend towards a stationary state for large systems. All other states show a similar but less pronounced trend. In general, all excitation energies are decreased by at least 1 eV starting from the dimeric system. Furthermore, the agreement between calculated and experimental excitation energies for the first excited state for the different systems is quite good, even though the difference between theory and experiment is ≈ 0.5 eV. For other

types of systems, similar or even better agreements have been reported for ADC(2) [183, 184].

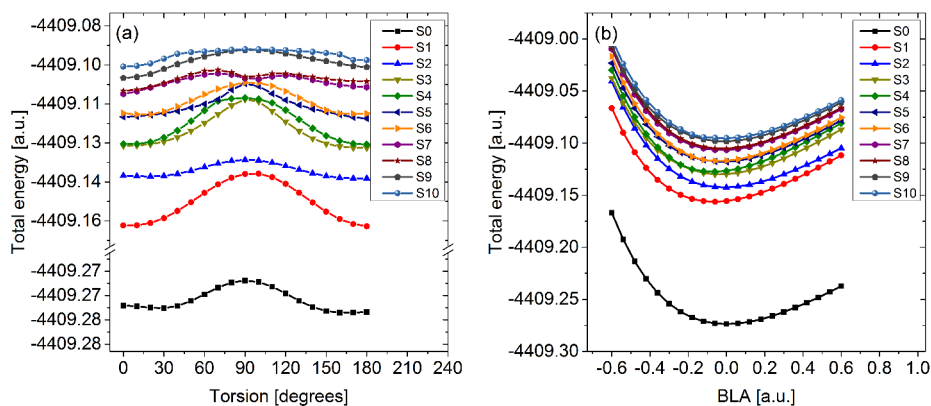


Figure 21: Total energies of the (a) torsional and (b) BLA coordinate for the ground state and the first 10 singlet excited states.

The results for the structure and the electronic properties discussed so far lead to the conclusion that the combination of MP2 and ADC(2) is a reliable method to describe oligo-thiophene and to calculate the 1D PES required for the parametrization. In order to parametrize the model Hamiltonian, PES cuts for the coordinates of interest have to be obtained. Therefore, a rigid scan along the torsional and BLA coordinate (as defined in Fig.15) starting from the relaxed ground state structure has been performed. In Fig.21, the total energies of the ground state and the first 10 excited states for the torsional and the BLA PES are shown. For the ground state, the torsional coordinate shows 2 minima, one at $\approx 30^\circ$ and one global minimum at $\approx 160^\circ$, whereas the minima of the excited states are at $0^\circ/180^\circ$. All states have their global maximum at 90° , while the barrier height at this point differs.

For the excited states, it is observable that at this point, an avoided crossing of states exists, e.g., for states 4 and 5. This avoided crossing also explains the fact, that the description of the four highest states is not perfect, since the wave functions for these states are not stable any more, especially in the area of the avoided crossing. Nevertheless, the results are still reliable, since only the two lowest Frenkel states are of interest for the further analysis. For the BLA PES, one minimum is observed for all states, which is shifted to negative values compared to the ground state value centered at 0.0. The general curvature of the PES is Morse-type showing that all states are well separated for larger BLA values, while for negative BLA values, curve crossings are observable e.g. state 7 and 8.

These adiabatic PES have been transformed to a diabatic representation using the transformation routine as described in Chp.3 and the information about the two

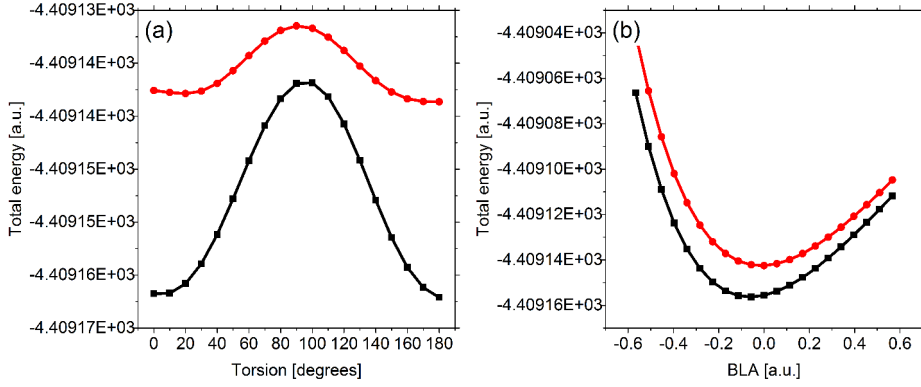


Figure 22: Results of the adiabatic-diabatic transformation (a) torsional coordinate and (b) BLA coordinate. The dots correspond to the adiabatic states, whereas the solid lines correspond to the transformed diabatic states (black= S_1 , red= S_2).

lowest excitonic states (S_1/S_2) obtained from the transition density analysis. As shown in Fig.22 for the excitonic states of the torsional and the BLA PES, the adiabatic-diabatic transformation results in the same potentials as stated by the theory (the diabatic ground state is obtained directly from the adiabatic ground state potential). Finally, these potentials have been fitted to a functional form, as shown in Fig.23.

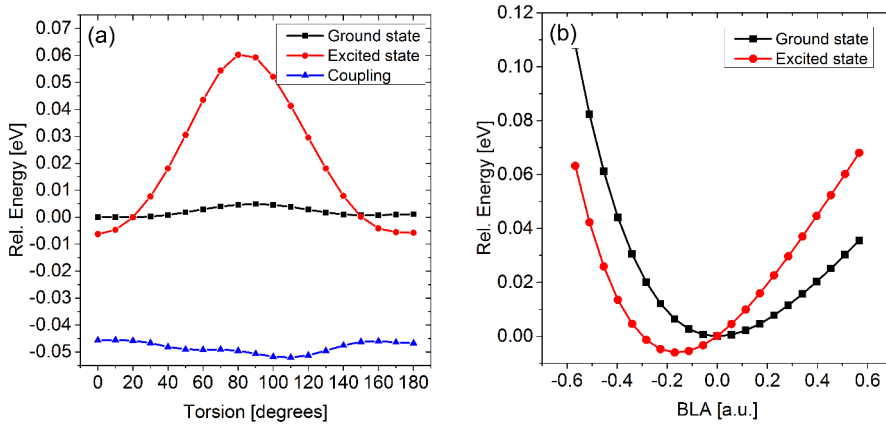


Figure 23: Transformed diabatic potentials (dots) and fitted diabatic potentials (line) represented by a functional form to the resulting points of the ground state (black), the excited state (red) and the coupling (blue) for (a) the torsional coordinate and (b) the BLA coordinate.

The functional form of the torsional PES is described by a cosine Fourier series as shown in Eqn.132

$$V^S(\theta) = a_0 + \sum_{k=1}^N (a_k \cdot \cos(k \cdot (\theta - \theta_0)) - a_k) \quad (132)$$

with S= ground state or excited state (G/E). The BLA potentials are fitted to a Morse-type functional form

$$V^S(\xi) = E_0 + a \cdot (1 - e^{-b(\xi-\xi_0)})^2 \quad (133)$$

For both coordinates, a good agreement of the diabatic potentials and the fitted functional form is observable. This good agreement is necessary for quantum dynamical calculations, since the results of the quantum dynamics are only such as good as the used potentials. The parameters of the torsional and the BLA functional form are given in Tbl.3 and 4, respectively.

Table 3: Parameters of the functional form of the PT torsional coordinate. If not specified, all parameters are given in a.u.

	a_0	a_1	a_2	a_3	a_4
Ground state	$6.7 \cdot 10^{-5}$	$-2.8 \cdot 10^{-4}$	$2.2 \cdot 10^{-3}$	$-2.2 \cdot 10^{-4}$	$7.1 \cdot 10^{-4}$
Excited state	$-6.3 \cdot 10^{-3}$	$4.4 \cdot 10^{-3}$	$-3.3 \cdot 10^{-2}$	$-4.7 \cdot 10^{-3}$	$4.1 \cdot 10^{-3}$
Coupling	$-4.6 \cdot 10^{-2}$	$3.8 \cdot 10^{-4}$	$2.7 \cdot 10^{-3}$	$-5.1 \cdot 10^{-4}$	$9.5 \cdot 10^{-5}$
	a_5	a_6	a_7	a_8	θ_0
Ground state	$-1.8 \cdot 10^{-5}$	$7.7 \cdot 10^{-5}$	$7.9 \cdot 10^{-6}$	$9.0 \cdot 10^{-6}$	160°
Excited state	$6.1 \cdot 10^{-4}$	$-2.4 \cdot 10^{-5}$	$-5.1 \cdot 10^{-4}$	$1.7 \cdot 10^{-4}$	180.0°
Coupling	$8.3 \cdot 10^{-4}$	$-5.1 \cdot 10^{-4}$	$-1.6 \cdot 10^{-4}$	$-1.4 \cdot 10^{-4}$	

Table 4: Parameters of the functional form of the PT BLA coordinate. If not specified, all parameters are given in a.u.

	E_0	a	b	ξ_0
Ground state	0.0	$1.9 \cdot 10^{-1}$	$9.9 \cdot 10^{-1}$	$-4.73 \cdot 10^{-4}$
Excited state	$-6.1 \cdot 10^{-3}$	$2.8 \cdot 10^{-1}$	$9.9 \cdot 10^{-1}$	$-1.7 \cdot 10^{-1}$

5.3.4 Exciton Dynamics on a Minimal Lattice

Based on the *ab initio* calculations and the parametrization presented in the previous section, quantum dynamical calculations for a PT hexamer system have been performed using the Heidelberg MCTDH package. The aim of the simulation was to describe the exciton dynamics of the PT hexamer in the presence of a torsional defect (structure distorted by 60° with respect to the ground state torsional angle) centered in the middle of the polymer chain in a Frenkel or a full *e-h* basis. The total number of electronic states of the Hamiltonian is $N=6$ for the Frenkel and $N^2=36$ for the full *e-h* model with a total number of DOF $k=13$ (1 torsional DOF, 5 BLA DOF and 7 harmonic oscillator bath coordinates). In case of the Frenkel model, a multi-set formalism is used for the description of the SPF's while a single-set formalism is used for the full *e-h* model. The active coordinates are represented by SPFs (at least 5 SPFs per coordinate), whereas two BLA modes have been combined into one SPF to reduce the computational effort. The SPFs are expanded in a primitive grid basis, which is described by a discrete variable representation. A harmonic oscillator representation is used with 1024 grid points for the torsional DOF, 80 grid points for the BLA DOF and 50 grid points for the harmonic oscillator bath. The reason for the large number of grid points of the torsional coordinate is the large expected change of the coordinate, whereas the expected change of the BLA and the bath coordinates is rather small. The total number of configurations of the Frenkel model is $N_{config}=2370480$, whereas the total number of configurations for the full *e-h* model is $N_{config}=640744$. The overall accuracy is given by analyzing the population of the highest populated SPF and the population of the primitive grid at the end and the beginning. For a fully converged calculation, the population of the highest SPF should be less than 0.1% and the population at the ends of the grid almost zero. For the pure Frenkel case, this convergence is achieved, whereas for the full *e-h* model, the SPF convergence is not achieved completely (which is related to the large number of degrees of freedom). Nevertheless, the results of the CT model are in agreement with the Frenkel type model.

As an initial condition, a FC excitation on a sub-fragment (left or right) is assumed. Such a fragment is often called *spectroscopic unit* and described by various experiments. This initial condition is prepared by relaxing an arbitrary initial wave function on the sub-fragment lattice. The resulting wave function can be seen as the lowest eigenstate of a particle-in-a-box system, which is defined by the sub-lattice. The so relaxed wave function is used for the propagation of the system.

In Figs.24-26, the results for the Frenkel excitonic system are shown.

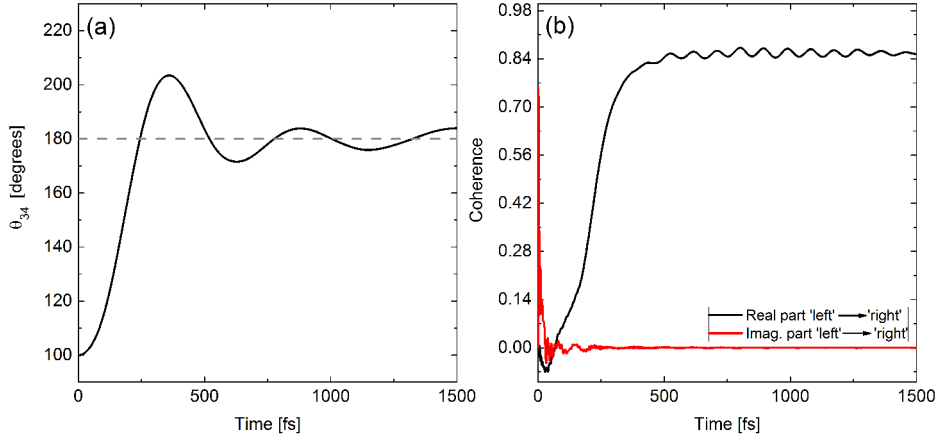


Figure 24: (a) Time evolution of the dynamics of the torsional coordinate θ_{34} and (b) the electronic coherence from the 'left' to the 'right' fragment of the PT hexamer up to 1.5 ps.

For the torsional degree of freedom, a planarization to 180° , starting from the initial value of 100° , is observable within 1.5 ps. During the first 500 fs, a step increase in the torsional angle is observable with slower oscillations around the minimum value $\theta_0=180^\circ$ afterwards.

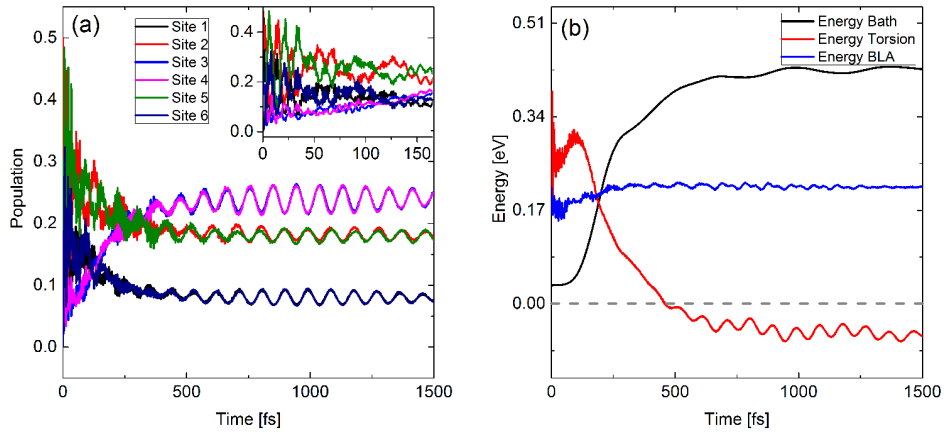


Figure 25: (a) 1D representation of the Frenkel exciton dynamics. The initial population is located on site 1-3 with the maximum on site 2 (population on site 2 = 0.5). The inlay focuses on the first 150 fs. (b) Time evolution of the total energy of the torsional coordinate θ_{34} , the BLA coordinate and the harmonic oscillator bath.

This planarization is the result of the coupling of the torsional coordinate to the harmonic oscillator bath and the exciton dynamics. Analyzing the Frenkel state population dynamics, a direct correlation between the torsional DOF and the state populations is observable. As shown in Fig.25, the initial population is strictly

located on states 1-3 (as prepared by the relaxation process) and a rapid transfer to states 4-6 is observable within the first 100 fs with a strong oscillating pattern. After ≈ 500 fs, a quasi-stationary state centered in the middle of the lattice is formed, which is observable up to the maximum simulation time. This quasi-stationary state, also called *local excitonic ground state* (LEGS), can be described by the lowest particle-in-a-box state (for a different perspective, see Fig.26b) for the overall lattice, whereas the oscillatory dynamics of the population on the longer time scale is related to energy fluctuations induced by the BLA coordinates.

Analyzing the total energy of the coordinates, it is observable that the harmonic oscillator bath efficiently absorbs the energy of the torsional DOF resulting in a similar quasi-stationary state, whereas the total energy of the BLA coordinates shows only minor changes. The formation of the new LEGS is also observable in the BLA dynamics. As shown in the left panel of Fig.26, the BLA coordinates end up in a mirrored dynamics of the Frenkel state population (right panel of Fig.26). Such trapping effects of coordinates are known for many types of systems after photoexcitation e.g. carotene type systems but is also described theoretically by Barford et al. for PPV type systems [96, 185].

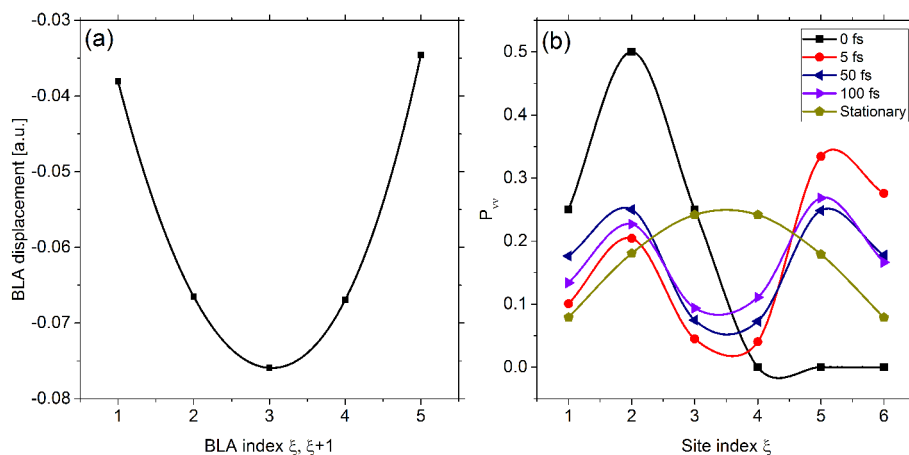


Figure 26: (a) BLA displacement for the stationary state. The BLA values of the stationary state are calculated by averaging the last 100 fs of the simulation. (b) Frenkel population dynamics for selected times. The population of the stationary state is calculated by averaging the last 100 fs of the simulation.

To evaluate if the observed Frenkel exciton dynamics is a coherent or a non-coherent process, the real and imaginary part of the coherence from the 'left' to the 'right' fragment is calculated. In general, the imaginary part of the coherence can be seen as a measure if a transfer process is coherent or non-coherent and how long a coherent transfer process takes place. (More specifically, the imaginary part of the coherence is related to the transient population flux.) As shown in

the right panel of Fig.24, the life-time of the imaginary part of the coherence is $\approx 150\text{-}200$ fs, which is quite long for such a fast exciton dynamics. The real part of the coherence also shows the formation of a quasi-stationary state and the time scale of this process is in good agreement with the time scale observed for the torsional DOF and the Frenkel exciton dynamics. To improve the Frenkel model and to include delocalized states such as CT states, the same setup is used for a model Hamiltonian in the full $e\text{-}h$ basis. Due to the high computational effort for the high number of configurations, the number of SPFs is reduced to at least 3 per DOF and therefore, the number of configurations is smaller compared to the Frenkel case (the higher number of configurations strongly correlates with the number of electronic states).

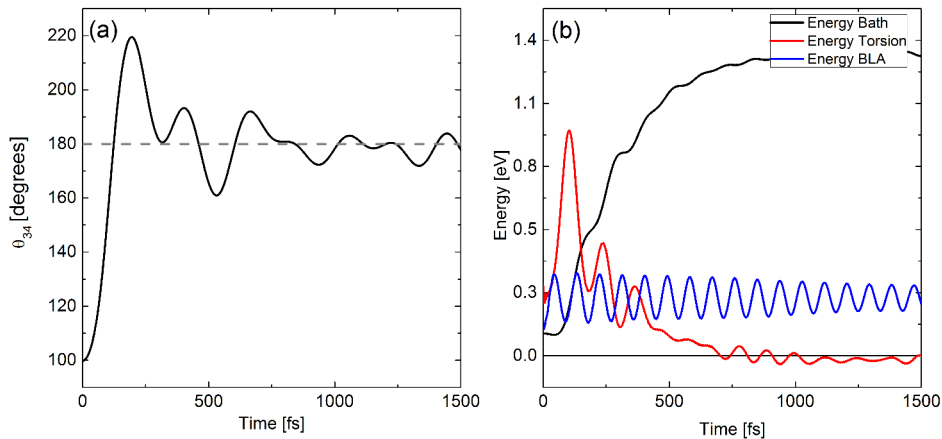


Figure 27: (a) Time evolution of the dynamics of the torsional coordinate θ_{34} for the full $e\text{-}h$ model and (b) the total energy of the torsional, the BLA and the harmonic oscillator bath coordinates.

Nevertheless, these results are reliable and the accuracy is acceptable but the small number of configurations can be a reason for some unexpected observations, since the calculation is not fully converged. The effect of this not fully converged calculation is observable in the torsional dynamics as shown in Fig.27a. As expected, a fast dynamics takes place during the first 250 fs towards a planar structure, however, the dynamics of the torsional mode is not as clear as in the pure Frenkel case. This is directly related to a not fully converged calculation. Nevertheless, it is clearly shown that the torsional angle planarizes, which is also indicated by the energy dynamics shown in Fig.27b.

Here a clear dissipative dynamics for the torsional DOF is observable, resulting in a quasi-stationary state. As in the Frenkel case, the total energy of the BLA DOF is almost constant for the overall simulation time. Due to the high number of states resulting from the full $e\text{-}h$ model, a *center-of-mass* (P_{ξ}^{CM}) population

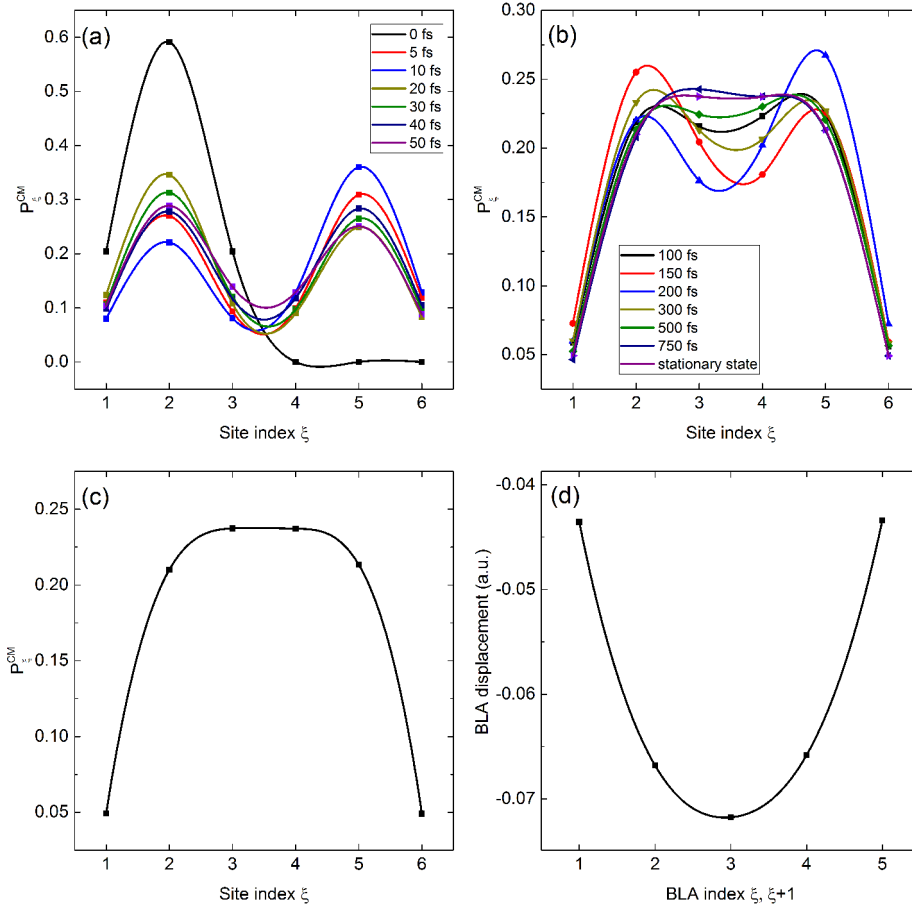


Figure 28: (a) and (b) Center-of-mass distribution P_{ξ}^{CM} for selected times (c) Center-of-mass distribution in the quasi-stationary state and (d) BLA displacement in the quasi-stationary state.

is defined, which is a more intuitive description of the population. The P_{ξ}^{CM} is defined as

$$P_{\xi}^{CM}(t) = \sum_{\nu, \mu=1}^{N_{site}} P_{\nu\mu} \quad |_{\nu+\mu=2\xi} \quad (134)$$

In Fig.28a and b, 1D representations of the P_{ξ}^{CM} for selected times are shown, indicating that the population transfer is again an ultrafast transfer from the 'left' to the 'right' fragment (for comparison to the pure Frenkel model, see Fig.26b) starting from the LEGS on the sub-lattice to the new LEGS on the overall lattice. The formation of LEGS is clearly observable for longer time scales and again, a trapping effect of the BLA coordinates can be seen. A different representation is shown in Fig.29. Here, the dynamics is described in the full $e-h$ basis. The formation of the LEGS takes place on a time scale of ≈ 500 fs, which is on the same order as in the pure Frenkel model. The population dynamics starts to spread over the full lattice from its initial position and an oscillatory dynamics is

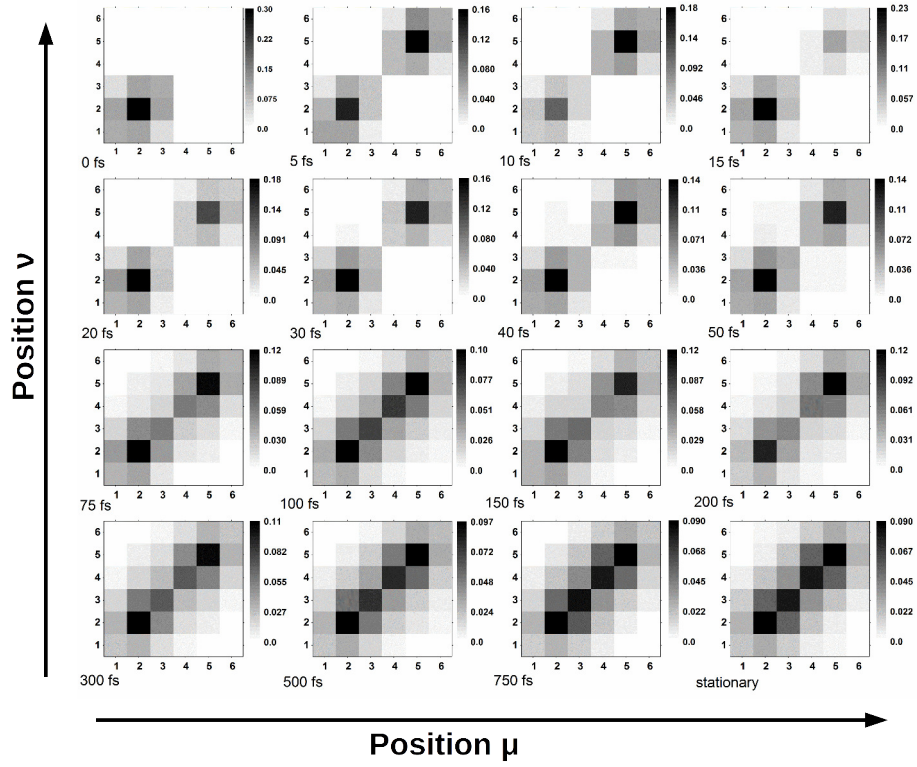


Figure 29: Time-evolution of the e - h dynamics on the hexamer lattice for selected times complementary to Fig.28a and b. The x-axis corresponds to the position of the electron and the y-axis corresponds to the position of the hole. The distribution is plotted in grayscale; the scale is not identical for all plots.

observable up to 500 fs. The advantage of the full e - h model is the possibility to describe the dynamics in a 2D context, which allows to calculate properties such as standard deviations of distributions. Furthermore, the results can be compared to the transition densities calculated by *ab initio* methods. The analysis of the standard deviation of the coherence size distribution, the individual coherence size components and the general electronic coherence from the 'left' to the 'right' fragment are shown in Fig.30. As shown, the standard deviation of the coherence size increases immediately from ≈ 0.95 to ≈ 1.25 which is very similar to the value of $\Omega_{S_1} = 1.4$ calculated for the *ab initio* transition densities. This is also apparent from the e - h distribution for the stationary time, which is very similar to the transition density of the lowest single excited state of the PT octamer shown in Fig.18.

In contrast to the Frenkel model, the electronic coherence of the energy transfer from the 'left' to the 'right' fragment does not show such a clear dynamics as in the Frenkel case. In the full e - h model, the real part of the electronic coherence is less strong but also indicates the formation of a stationary state, while the imaginary

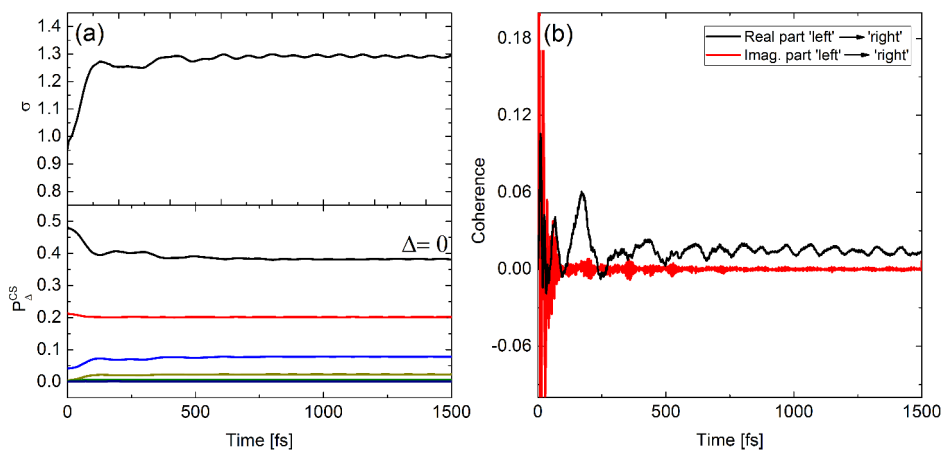


Figure 30: (a) Time evolution of the standard deviation σ of the coherence size distribution (upper panel) and individual coherence size components $P_{\Delta}^{CS} = \sum_{\nu, \mu=1; \nu-\mu=\Delta}^{N_{Site}} P_{\nu, \mu}(t)$ for $\Delta = 0, \pm 1, \dots$ (lower panel) (b) Time-evolution of the electronic coherences from the initial 'left' fragment to the 'right' fragment. Red= real part, black= imaginary part. Only the Frenkel type coherences are considered.

part decays on the same time scale as in the Frenkel model. The different time-evolution of the real part coherence can be related to the not fully converged calculation but can also be an effect of the generalized $e-h$ model.

5.3.5 Exciton Dynamics on a Large Lattice

Up to now, the system size is small as compared to real systems even though representative exciton dynamics can already be described as detailed above. To describe exciton dynamics for larger systems, which can capture exciton migration, the Hamiltonian is extended to a PT 20-mer in combination with the ML-MCTDH method.

By a systematic variation of the initial conditions, the role of low- and high-frequency coordinates in the exciton transfer dynamics and the concept of spectroscopic units [43] can be evaluated.

In Fig.31, the results for different setups and initial conditions are shown. For a fixed torsional coordinate (Fig.31a), a confined is observable. For the first few hundred fs most of the initial wave packet remains on the initial fragment and shows some minor oscillations, while only a few percent of the population are transferred to the other sub-lattice on this time scale. After ≈ 600 fs, most of the population is transferred to the upper sub-lattice and forms a new LEGS. This new LEGS is stable for ≈ 200 fs and is then re-transferred to the lower sub-lattice.

The impact of the torsional motion on this dynamics is shown in Fig.31b. By describing the torsional coordinate as an active degree of freedom coupled to a dissipative bath, the formation of a new local excitonic ground state centered in the middle of the overall lattice can be observed. This new LEGS is formed after ≈ 300 fs, but already after ≈ 100 fs, a significant population transfer to the upper sub-lattice is observable. On this time scale, the torsional angle reaches the regime of the ground state value.

Interestingly, the exciton dynamics described for these two initial conditions shows high-frequency fluctuations during the overall simulation time. These fluctuations are due to both electronic Rabi-type oscillations and BLA vibrations.

By reducing the coupling to the dissipative bath (Fig.31c), a more delocalized exciton dynamics on the overall lattice is observed. The formation of a stable LEGS is now observable after ≈ 1.0 ps which is much slower than the dynamics described before. In contrast to this slow formation, the formation of the LEGS for a planar system as shown in Fig.31d takes place on a time scale of ≈ 100 fs, which is much shorter compared to a twisted initial condition. Furthermore, very strong fluctuations in the first 200 fs can be observed.

By removing the dissipative bath (as shown in Fig.31e), no formation of a LEGS is observable but the exciton dynamics takes place on the overall lattice. Again, the exciton dynamics is observable on the overall lattice after 200-300 fs but no formation of a LEGS for longer times is observable. In contrast to the dynamics described in Fig.31(a)-(d), no planarization of the torsional coordinate is observed.

In general, it can be observed that a rapid change in the population dynamics is observable for torsional angles close to the ground state value or a planar value. For these structures, a compact exciton centered in the middle of the lattice can be found if dissipation is present. By contrast for the case without a dissipative bath, a spread-out dynamics on the overall lattice is observable.

These results lead to the conclusion that the dynamics of the torsional coordinate, especially the planarization of the system, is essential for the exciton dynamics on the overall lattice and the formation of a LEGS centered in the middle of the lattice. However, LEGS formation also depends on the BLA coordinate which is responsible for the exciton trapping. Interestingly, the exciton dynamics shows a very fast transition between the left and right sub-lattice for all setups. One reason for this fast, apparently electronic dynamics could be the fact that Hamiltonian includes only correlated modes which favor electronic resonance effects. By adding a site-local high-frequency coordinate on each monomer, this resonance effect can be reduced. These coordinates can be compared to local ring vibrations, which

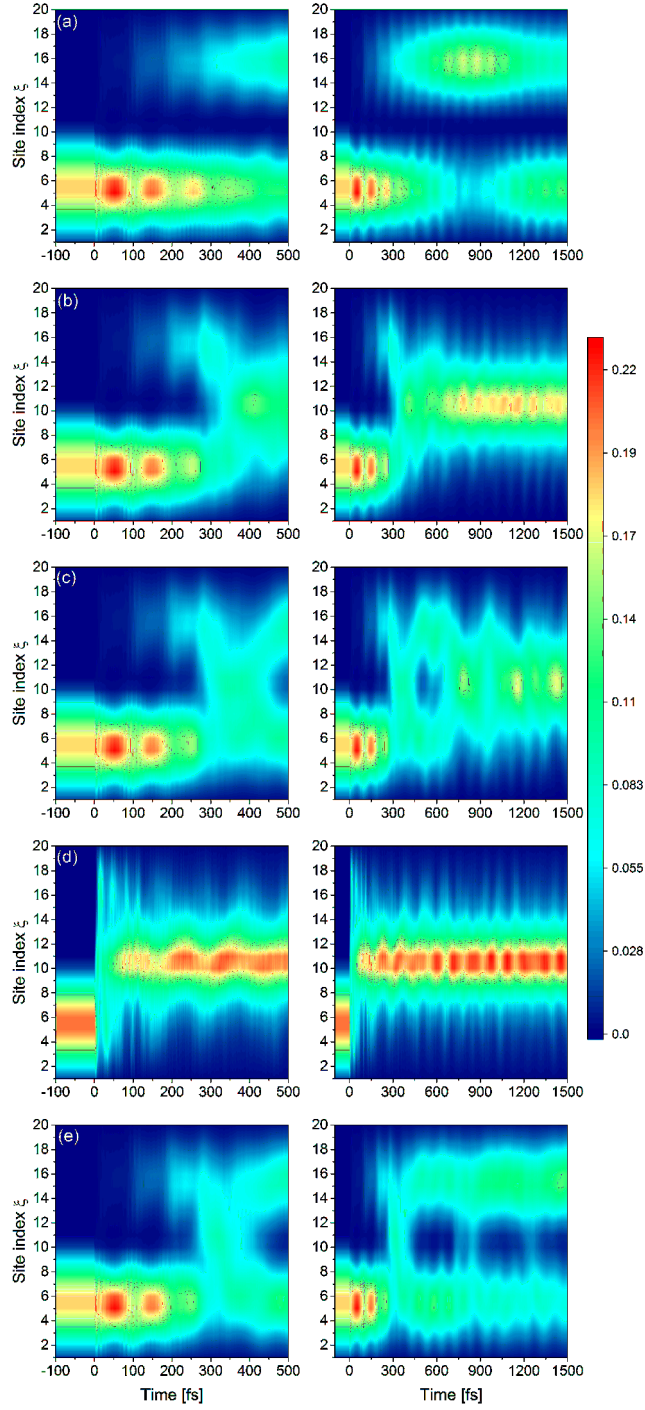


Figure 31: Analysis of the exciton dynamics and the exciton self-trapping effect for different initial conditions for a PT 20-mer using the full quantum ML-MCTDH method. The initial wave function is always located on sites 1-10. (a) Fixed torsional coordinate $\theta=100^\circ$, (b) active torsional coordinate $\theta=100^\circ$, (c) active torsional coordinate $\theta=100^\circ$ with a very low damping factor, (d) active torsional coordinate $\theta=180^\circ$ and (e) active torsional coordinate $\theta=100^\circ$ without coupled bath. The color scaling is identical for all plots and given by the color bar. For all plots, the right panels show the overall dynamics whereas the left panels show only the dynamics up to 500 fs.

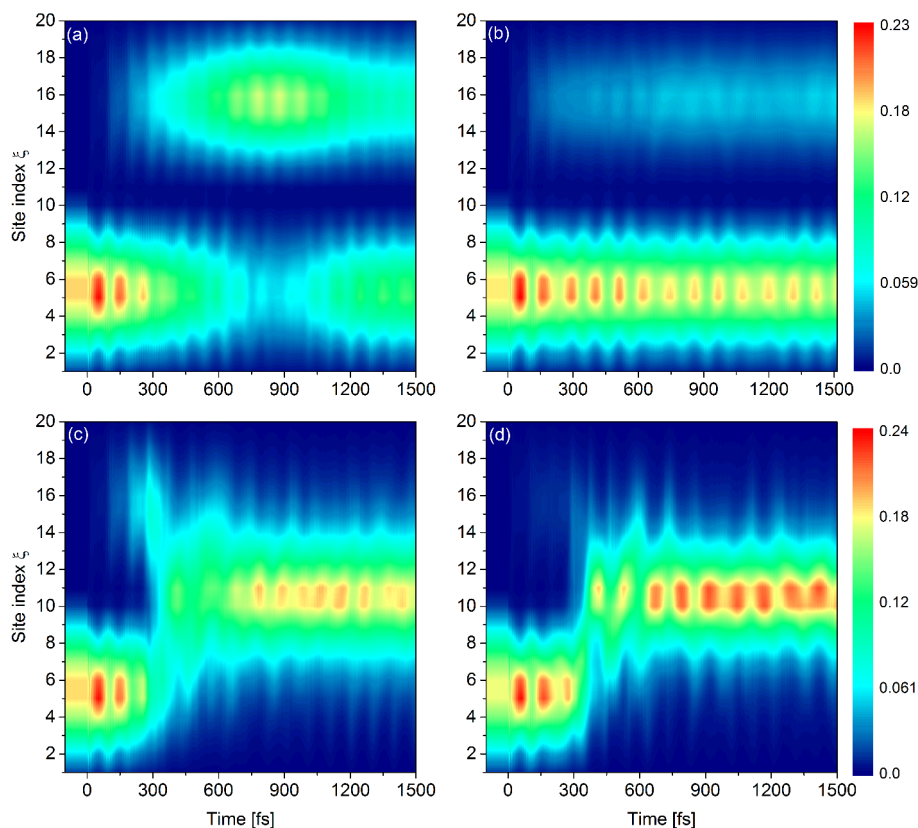


Figure 32: Analysis of the exciton dynamics and the exciton self-trapping effect for different initial conditions for a PT 20-mer using the full quantum ML-MCTDH method with and without additional site-local coordinates. The initial wave function is always located on sites 1-10. (a) Fixed torsional coordinate $\theta=100^\circ$, (b) Fix torsional coordinate $\theta=100^\circ$ with additional site-local coordinates, (c) Active torsional coordinate $\theta=100^\circ$ and (d) Active torsional coordinate $\theta=100^\circ$ with additional site-local coordinates. The color scheme of panel (a) and (b) is given next to panel (b), the color bar of panel (c) and (d) is given next to panel (d).

have been observed e.g. by Bragg et al. [186]. In Fig.32, the comparison of this augmented model to the original model is shown for $\theta_{init.}=100^\circ$. As shown in Fig.32a and b, the effect of the additional site-local coordinates is quite remarkable. As postulated, these coordinates induce a de-tuning of the resonant electronic system which results in a smoother dynamics. For a fixed torsional coordinate, most of the initial population remains on the initial sub-system and forms a new LEGS. Only a minor friction of the population is transferred to the upper sublattice and forms a LEGS on this lattice. By describing the torsional coordinate as an active coordinate (as shown in Fig.32c and d), the fast dynamics after ≈ 100 fs is decreased and also the fluctuations in the population are decreased. This indicates that the previously described dynamics is a result of the highly correlated site-site coordinates of the model Hamiltonian. By introducing uncorrelated site-local

coordinates, the site energies became more off-resonant. This de-tuning results in a more smooth exciton dynamics and should better capture the dynamics in the real system.

5.3.6 Conclusion

Using a small hexamer model system and a larger 20-mer system, we were able to describe two typical situations: first, the spreading of an exciton across a torsional defect, from an initial condition located close to the defect. Second, the torsion-induced migration of an exciton which is initially trapped on a sub-lattice. Both phenomena are ultrafast and coherent. Interestingly, the second case exhibits a coherent hopping type dynamics.

Based on the results presented for the Frenkel type model and the full $e-h$ model, the minimal lattice used in the simulation is already able to describe the exciton dynamics properly. The results of the full $e-h$ model are very close to the results of the simplified Frenkel type model, with the drawback that the computational effort is much higher due to the high number of electronic states. Therefore, the full $e-h$ representation is not necessarily needed to describe intra-chain dynamics. This allows the dynamical description of energy transfer on a full quantum level, using a Frenkel model.

Furthermore, it was shown that the time scale of the energy transfer process is in the sub-ps range, which is indeed a very fast process. Additionally, it has been demonstrated that the exciton dynamics is affected by structural defects. A „healing“ of the defects favors the exciton migration on the overall lattice. Also the observed time scale for the EET agrees with the observations of previous simulations on similar systems [166, 187].

By describing the exciton dynamics on a larger lattice, we arrive at observations that are consistent with the spectroscopic unit concept. In particular, (i) the exciton is found to be spatially confined due to geometric defects, (ii) exciton migration occurs as a consequence of planarization of the central torsional coordinate, (iii) if the torsional coordinate is damped, immediate formation of a new LEGS occurs in the middle of the lattice. By including uncorrelated site-local coordinates, the electronic transfer dynamics is detuned such that extremely rapid Rabi-type oscillations disappear. A description including both correlated and uncorrelated modes should provide a realistic setting.

Finally, the theoretical results obtained by the quantum dynamical calculations are in agreement with results for similar types of systems. As described by Barford and others [152, 185, 188, 189] the formation of LEGS is observable. However,

the present results are the first quantum dynamical investigation of the exciton migration mechanism, leading to an interesting „coherent hopping“ type picture. In the following section, we will use more approximate mixed quantum-classical methods to move toward longer time scales and include thermal effects.

5.4 Exciton Dynamics on a Minimal Oligo-*p*-Phenylene Vinylene Lattice studied by MCTDH and Ehrenfest Dynamics

Another very promising material for the development of organic photovoltaics is poly-*para*-phenylene vinylene (PPV). This material is not widely used commercially for organic photovoltaic devices but in contrast to PT, devices based on PPV with a sufficient large efficiency (up to 9%) have been developed. The problem of these devices is the sensitivity to environmental effects such as water or very low temperatures [190, 191]. Up to now, these environmental effects destroy the semi-conducting polymer-layer on a very short time scale (several month) [192, 193]. However, for photovoltaic devices it is necessary that they are robust and stable for daily use, e.g., on roofs. Furthermore, the conversion mechanism from solar energy to electric energy and the role of different external effects such as temperature are not well studied yet. Various experimental and theoretical approaches to study the initial energy transfer dynamics in PPV have been carried out [20, 71, 83, 194, 195]. Several groups developed different theoretical models to describe the energy transfer on a sub-ps time scale. As for PT, the full quantum MCTDH method in combination with *ab initio* parameters was used by Burghardt et al. to study the EET in the presence of a torsional defect[23]. These results show an energy transfer within the polymer chain on a sub-ps time scale. Their model and the parametrization has been improved by Binder et al. including a dissipative bath [166]. Another approach was introduced by Barford et al. describing the EET as a two step process: (i) an ultra-fast relaxation on a sub-ps time scale followed [185, 188] by (ii) a random hopping process [96]. First time-resolved experiments using spectroscopic techniques were performed by Scholes et al., describing the EET as a surfing-type process [13]. This surfing-type EET is also described by Stafstrøm et al. using an electron lattice dynamical description, to simulate the EET in a PPV wire [34]. They used the Ehrenfest dynamics for the description of vibrational DOF and electronic states. Their work is focused on the dynamics in ordered/disordered systems in the presence of an external electric field. Using the Ehrenfest approach and a simple model Hamiltonian, they were able to describe the EET for systems up to 300 sites also including steric effects such as torsional coordinates (such a large system including so many electronic states can not be described by the full-quantum MCTDH method. For these systems, the ML-MCTDH approach could be useful).

Thus, a lot of research has focused on steric effects or order/disorder and most of the models neglect the effect of temperature. Some models include temperature effects implicitly, e.g., a harmonic oscillator bath can include a temperature dependent sampling, but models including temperature as an explicit parameter for EET have been restricted to kinetic treatments. Therefore, the focus of this project is on the effect of temperature on the intra-molecular EET in a PPV wire. To include temperature explicitly, the Langevin description of a heat bath is used combined with the Ehrenfest dynamics. In order to evaluate the Ehrenfest method, benchmark calculations are performed using the MCTDH method for a small PPV system. This benchmark is important since so far, no comparisons of the semi-classical Ehrenfest method and full quantum methods for EET in these types of systems have been performed. For other areas of research, only a few benchmark calculations have been carried out, indicating some discrepancies between Ehrenfest and exact methods [196, 197].

5.4.1 Model System and Model Hamiltonian

To study the temperature effect on the EET process in PPV in the presence of a torsional defect, an appropriate model is needed. The model used for the *ab initio* calculations and the quantum dynamics is very similar to the model used for the description of PT. As shown in Fig.33, the system is constructed from n *p*-phenylene vinylene monomer units resulting in a linear chain. EET depends on the overlap of the conjugated π -system and therefore, the torsional coordinate between the ethenyl bridge and the benzene ring plays an important role in these processes [198, 199]. This coordinate will be included explicitly in the quantum dynamical simulations. In addition, the high-frequency BLA coordinate illustrated in the inset of Fig.33 is also included in the model to study self-trapping effects after photoexcitation. We expect that the interplay of torsional and BLA modes captures the main features of the vibronic dynamics. The parametrization of these coordinates is performed using the exact adiabatic-diabatic transformation of *ab initio* data as described in Chp.5.2.

The *ab initio* calculations were performed by Panda et al. [29] using the MP2 and ADC(2) method with the SV(P) basis set [200] as implemented in the TURBOMOLE program package [169]. To represent the band character of the semi-conducting system, a PPV octamer was used in the *ab initio* calculations. One-dimensional cuts along the coordinate of interest were performed based on the relaxed ground state structure.

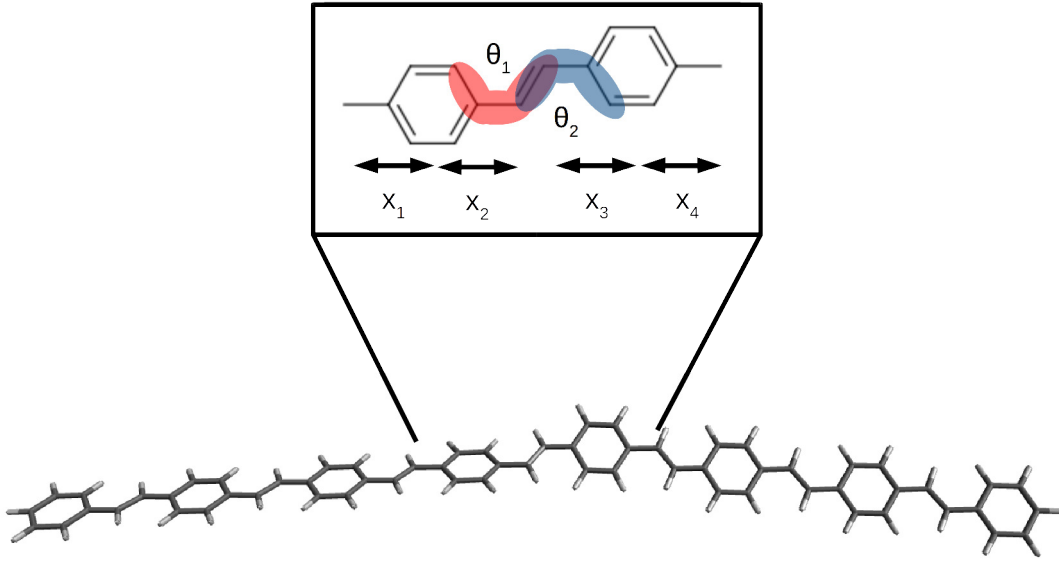


Figure 33: Model system for the *ab initio* calculation of the PPV oligomer. The site-local BLA coordinates x_i are indicated by arrows, the site-local torsional coordinate θ_i is indicated by the red and blue area.

For the quantum dynamical calculations, a Frenkel-type basis is used to represent the model Hamiltonian. The advantage of this basis is the description of excitonic states in terms of monomer units. The general form of the model Hamiltonian is similar to the PT case, except that site-local instead of site-correlated modes are defined. The Hamiltonian is given as follows

$$H = \sum_{\nu\mu} \sum_{\nu'\mu'} H_{\nu\mu,\nu'\mu'} |\nu\mu\rangle \langle \nu'\mu'| \quad (135)$$

with

$$\begin{aligned} H_{\nu\mu,\nu'\mu'} = & \delta_{\nu\nu'} \delta_{\mu\mu'} (H_{\nu\mu,\nu'\mu'}^{\text{intr}} + H_{\nu\mu,\nu'\mu'}^{\text{BLA}} + H_{\nu\mu,\nu'\mu'}^{\text{tors}} + H_{\nu\mu,\nu'\mu'}^{\text{bath}}) \\ & + \delta_{\nu\mu} \delta_{\nu'\mu'} H_{\nu\mu,\nu'\mu'}^{\text{Frenkel}} + H_{\nu\mu,\nu'\mu'}^{\text{CT}} \end{aligned} \quad (136)$$

All terms of Eqn.136 can depend on vibrational coordinates. The first term on the r.h.s describes the intrinsic *e-h* pair interactions H^{intr} and is diagonal in the *e-h* basis. The second and the third term describe the vibronic contributions related to the BLA and the torsional coordinate. The fourth term corresponds to a harmonic oscillator bath, acting as a source of dissipation. The last two terms describe the Frenkel or charge-transfer type couplings and contain off-diagonal elements. This model can be reduced from the full *e-h* basis to the Frenkel basis by discarding all terms including CT states. The resulting Frenkel Hamiltonian is given by

$$H_{\text{Frenkel}} = \sum_{\nu} \sum_{\nu'} H_{\nu\nu,\nu'\nu'} |\nu\nu\rangle \langle \nu'\nu'| \quad (137)$$

with

$$H_{\nu\nu,\nu'\nu'} = \delta_{\nu\nu'} (H_{\nu\nu,\nu'\nu'}^{\text{intr}} + H_{\nu\nu,\nu'\nu'}^{\text{BLA}} + H_{\nu\nu,\nu'\nu'}^{\text{tors}} + H_{\nu\nu,\nu'\nu'}^{\text{bath}}) + H_{\nu\nu,\nu'\nu'}^{\text{Frenkel}} \quad (138)$$

The terms of Eqn.138 are identical to the terms described in Eqn.136. Similar to the PT Hamiltonian, the intrinsic interaction term is given by

$$H_{\nu\mu,\nu'\mu'}^{\text{intr}} = \delta_{\nu\nu'} \delta_{\mu\mu'} \left(e_0 - \frac{1}{4\pi\epsilon_0\epsilon_r r_{\nu\mu}} \right) \quad (139)$$

with the e - h distance $r_{\nu\mu}$ as a function of the sites $(\nu\mu)$. $r_{\nu\mu}$ is defined by $r_{\nu\mu} = |\nu - \mu| r_{ru} + r_0$, with r_{ru} the repeat unit length, and r_0 the intrinsic e - h distance of a Frenkel exciton. The relative permittivity is set to 1, e_0 is the exciton binding energy and defined in this way that for a localized e - h pair $H_{\nu\mu,\nu'\mu'}^{\text{intr}} = 0$. The vibronic elements of Eqn.136 correspond to contributions of the torsional coordinate θ_i and the BLA coordinate χ_i for the ground and excited state. For a vibronic term H^{tors} or H^{BLA} is given by

$$H_{\nu\mu,\nu'\mu'}^{\text{vibronic}}(x_\xi) = \delta_{\nu\nu'} \delta_{\mu\mu'} \sum_{\xi=1}^{N_{\text{sites}}} \left(-\frac{1}{2} \frac{\partial^2}{\partial x_{\xi_i}^2} + v_i^G(x_{\xi_i})(1 - \delta_{\nu\xi}) + v_i^E(x_{\xi_i})\delta_{\nu\xi} \right) \quad (140)$$

where the site-local coordinates θ and χ are represented by x_{ξ_i} , v_i^S denotes the ground and excited state monomer potential (S=G/E) and N_{site} is the number of monomer units. Each monomer consists of two site-local torsional and two site-local BLA coordinates, whereby only the two torsional coordinates centered in the middle of the chain are treated as active coordinates. The location of the electron $\nu_e = \nu$ defines the participation of an excited-state monomer potential.

The bath Hamiltonian H^{bath} is taken to act on the torsional coordinates only. This description of a dissipative environment will reduce the computational effort with a maximum effect. For the quantum dynamical calculations using the MCTDH ansatz, a Caldeira-Leggett description of the bath is used given by

$$H_{\nu\mu,\nu'\mu'}^{\text{Bath}} = \delta_{\nu\nu'} \delta_{\mu\mu'} \sum_{i=1}^{N_B} \left[-\frac{1}{2} \frac{\partial^2}{\partial x_{B,i}^2} + \frac{1}{2} \omega_{B,i}^2 \left(x_{B,i} - \frac{c_{B,i}}{\omega_{B,i}^2} \theta \right)^2 \right]. \quad (141)$$

Here, an Ohmic spectral density given by $J_{\text{Ohm}} = 2\gamma\Delta\omega e^{-\omega/\Lambda}$ is used. The coupling coefficients c_i are calculated by $c_{B,i} = (2\omega\Delta\omega J_{\text{Ohm}}(\omega)/\pi)^{1/2}$ with the discrete sampling interval $\Delta\omega$ defining the Poincaré recurrence time $t_{PC} = 2\pi/\Delta\omega$.

Finally, the Frenkel-type couplings are given by

$$H_{\nu\mu,\nu'\mu'}^{\text{Frenkel}} = \delta_{\nu\mu} \delta_{\nu'\mu'} (\delta_{\nu',\nu+1} J_{\text{Frenkel}} \left(\frac{1}{2} (\theta_\nu^R - \theta_{\nu'}^L) \right) \left(\frac{1}{2} (\chi_{\xi_\nu}^R - \chi_{\xi_{\nu'}}^L) \right) + \delta_{\nu',\nu-1} J_{\text{Frenkel}} \left(\frac{1}{2} (\theta_\nu^R - \theta_{\nu'}^L) \right) \left(\frac{1}{2} (\chi_{\xi_\nu}^R - \chi_{\xi_{\nu'}}^L) \right)) \quad (142)$$

with the Frenkel-type coupling $J_{Frenkel}$. The Frenkel-type couplings are described in terms of a difference torsional angle $\theta_{\nu'\nu}^{diff} = 1/2(\theta_{\nu'}^R - \theta_{\nu}^L)$ and a difference BLA coordinate $\chi_{\nu'\nu}^{diff} = 1/2(\chi_{\nu'}^R - \chi_{\nu}^L)$. The terms for the torsional, the BLA and the coupling are fitted to a functional form representing the diabatic PES.

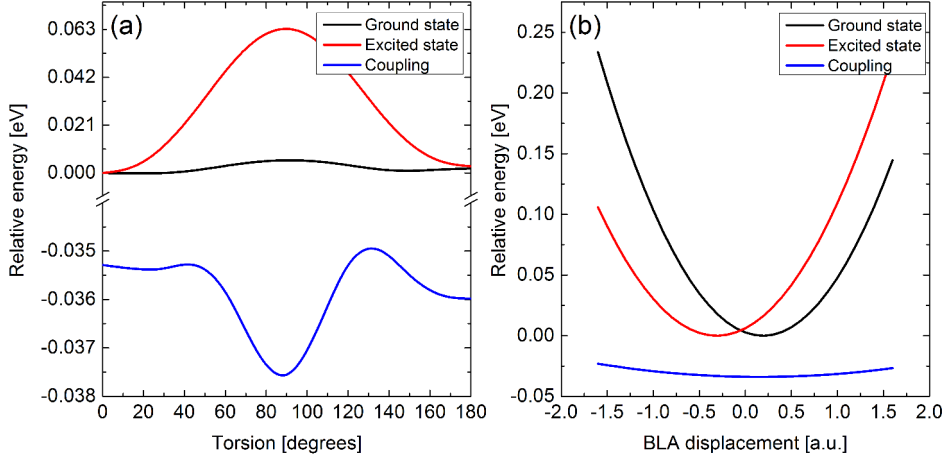


Figure 34: Diabatic potential energy surfaces of the first two Frenkel excitonic states and the coordinate dependent coupling of the PPV octamer obtained after an exact adiabatic-diabatic transformation (a) PES of the site-local torsional coordinate and (b) PES of the site-local BLA coordinate.

The diabatic torsional and BLA potential for the ground and the excited state are shown in Fig.34. The ground state potential of the torsional coordinate indicates two minima, one located around 30° and one located around 150° , whereas the excited state potential has minima at 0° and 180° . Both potentials have their maximum at 90° . In contrast, the form of the BLA potentials is similar for the ground and excited state, only a shift in the excited state to negative values is observable. The torsional potential is fitted to a truncated Fourier series defined by

$$V^S(\theta) = a_0 + \sum_{j=1}^N (a_j \cdot \cos(j \cdot (\theta - \theta_0)) - a_j) \quad (143)$$

The BLA potential is fitted to a harmonic oscillator-type form

$$V^S(x) = E_0 + \frac{1}{2} a_S (\chi - \chi_0)^2 \quad (144)$$

The coupling is defined as a two-dimensional function depending on θ and the BLA coordinate χ_i and is defined by

$$J(\theta, \chi) = \left(a_0 + \sum_{j=1}^N \left(a_j \cdot \cos\left(j \cdot \frac{1}{2} \cdot (\theta^R - \theta^L)\right) - a_j \right) \right) \cdot \left(E_0 + \frac{1}{2} \cdot a \cdot \left(\frac{1}{2} (\chi^R - \chi^L) - \chi_0 \right)^2 \right) \cdot \varrho \quad (145)$$

The parameter ρ guarantees that the product of this 2-D function is always smaller or equal to the value at the maximum of the functions. All parameters of the functional forms are given in Tbl.5-6.

Table 5: Parameters of the functional form of the PPV torsional coordinate. All parameters are given in a.u.

	a_0	a_1	a_2	a_3
Ground state	0.0	$-6.60 \cdot 10^{-4}$	$-2.46 \cdot 10^{-3}$	$-2.30 \cdot 10^{-4}$
Excited state	0.0	$-7.53 \cdot 10^{-4}$	$-3.12 \cdot 10^{-2}$	$-6.95 \cdot 10^{-4}$
Coupling	$-3.52 \cdot 10^{-2}$	$6.19 \cdot 10^{-5}$	$6.87 \cdot 10^{-4}$	$3.01 \cdot 10^{-4}$
	a_4	a_5	a_6	θ_0
Ground state	$9.35 \cdot 10^{-4}$	$-9.58 \cdot 10^{-5}$	$1.57 \cdot 10^{-4}$	30.0°
Excited state	$2.60 \cdot 10^{-3}$	$-1.83 \cdot 10^{-5}$	$2.98 \cdot 10^{-4}$	0.0°
Coupling	$-7.29 \cdot 10^{-4}$	$-1.58 \cdot 10^{-5}$	$2.70 \cdot 10^{-4}$	

Table 6: Parameters of the functional form of the PPV BLA coordinate. All parameters are given in a.u.

	E_0	a	x_0
Ground state	0.0	$1.46 \cdot 10^{-1}$	$1.91 \cdot 10^{-1}$
Excited state	0.0	$1.27 \cdot 10^{-1}$	$-3.11 \cdot 10^{-1}$
Coupling	$-3.40 \cdot 10^{-2}$	$7.06 \cdot 10^{-3}$	$1.59 \cdot 10^{-1}$

5.4.2 Quantum Dynamics

Using the model Hamiltonian and the parametrization of the PPV octamer described in the previous section, full quantum dynamical and semi-classical simulations are performed. As for PT, two different main transfer pathways of the EET are possible: inter-chain and intra-chain. As illustrated in Fig.35, the polymer chain is built from n monomer units resulting in a random but partially ordered structure. This structure contains disordered areas (random coils) and ordered chains. Small fragments of these ordered areas are often described in terms of spectroscopic units as discussed in Sec.5.3. The concept of spectroscopic units allows to explain experimentally and theoretically spectroscopic observations or dynamical processes[201–203]. The dynamics simulated in the following will focus on the intra-chain EET in the presence of a structural defect for a PPV hexamer. The hexamer system-size can be seen as a combination of two minimal spectroscopic units separated by a structural defect.

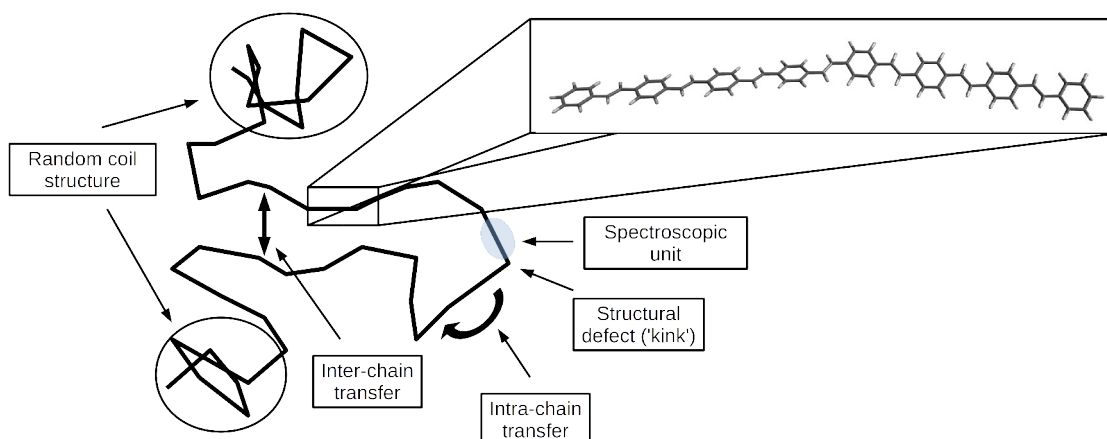


Figure 35: Schematic representation of a PPV polymer with different transfer pathways and areas.

In order to validate the semi-classical Ehrenfest method, a benchmark study for the PPV hexamer using the Frenkel model in combination with the MCTDH approach is performed. Based on this benchmark study, calculations for larger systems including an explicit description of temperature are performed using the semi-classical Ehrenfest method. These studies will focus on the effect of structural disorder and thermal noise on the EET in PPV.

The model contains 6 monomer Frenkel states, 2 site-local torsional coordinates centered in the middle of the chain and 12 site-local BLA coordinates. For the dissipative environment, a set of 2×7 harmonic oscillators sampled from an Ohmic spectral density and coupled to the torsional coordinates θ_i is used. The initial value of the torsional coordinates is $\pm 45^\circ$, resulting in a difference torsional angle

$\theta^{diff.} = 90^\circ$ between two monomer units. These torsional coordinates are fixed for the preparation of the initial wave function. All other torsional coordinates are implicitly described by a fixed value of $\approx 20^\circ$. The initial value of the BLA coordinates is set to the ground state minimum. These coordinates are considered as active coordinates in the preparation of the initial wave function. This ansatz for the preparation of the initial wave function guarantees that the high-frequency BLA modes are relaxed while the torsional coordinates describing the structural defect are kept at their initial value $\theta_i = \pm 45^\circ$. Furthermore, the electronic wave function can be relaxed on the sub-fragment.

The number of SPFs is 7 for the torsional coordinates, 3 for the BLA coordinates and 3 for the bath coordinates. The SPFs are described using a primitive grid basis representation. For the primitive grid, a so-called discrete variable representation (DVR) is used. Here, 256 functions are used for the description of the torsional coordinate, 30 for the BLA and 20-50 functions for the bath coordinates. The total number of configurations of the MCTDH wave function is $1.49 \cdot 10^6$. At a later stage, calculations using the ML-MCTDH were carried out.

The initial condition of the system is prepared in the following way: an arbitrary wave function is relaxed on a sub-lattice of the system e.g. on monomers 1-3 ('left' fragment). This is done by relaxing the initial wave function in negative imaginary time. The so prepared initial state is used as a starting point for the propagation of the system in real time.

5.4.2.1 Convergence of the Ehrenfest Method

In theory, the convergence of the MCTDH approach scales with the number of SPFs and the primitive-grid size. The convergence of a MCTDH calculation is checked by analyzing the population of the primitive grid and the population of the highest occupied SPF. This analysis indicates an appropriate convergence of the MCTDH reference calculations.

In contrast to the MCTDH ansatz, the convergence of the Ehrenfest approach correlates with the sampling of the initial conditions and the reconstruction of the corresponding Wigner distribution. An improved sampling is achieved by an importance sampling procedure and therefore, the convergence of the Ehrenfest approach strongly correlates with the number of trajectories and the used integrator step-size. As already mentioned in Sec.5.1, a mixed RK integrator scheme with a fixed step-size is used for the integration of the trajectories. A similar integrator ansatz is used by Barford et al. [185] resulting in fast but still accurate results. In theory, the Ehrenfest approach is a norm-conserving approach and therefore, the

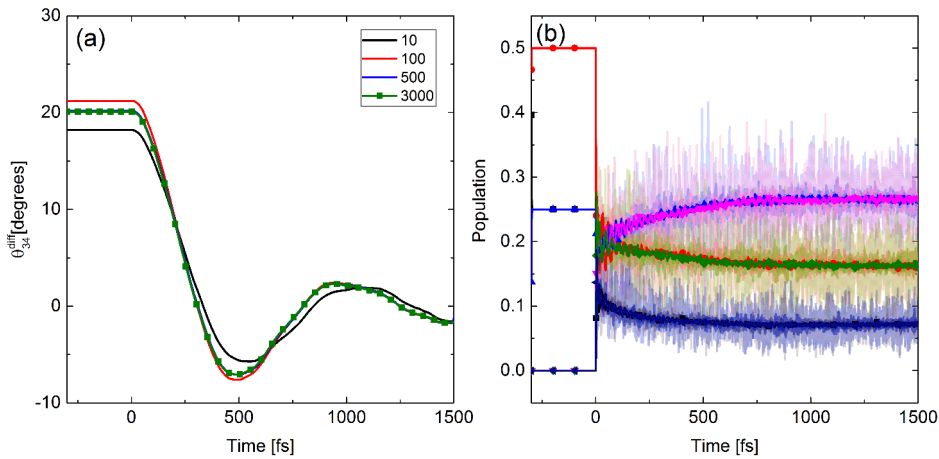


Figure 36: Convergence of the Ehrenfest approach for different number of trajectories (a) dynamics of the torsional coordinate and (b) Frenkel state dynamics. Very light colors represent the average of 10, light colors the average of 100, dark colors the average of 500 and symbols 3000 trajectories.

norm is used as a measure of quality of the calculation. For integrator step-sizes in the range of $\Delta t \geq 2.0$ a.u., no norm-conservation is observed for the overall simulation time. Reducing the step-size to $\Delta t \leq 2.0$ a.u., norm-conservation is achieved. Therefore, the typical integrator step-size is around 1.0 a.u. (or ≈ 0.025 fs). This step-size is in the same order as the MCTDH step-size using the ABM integrator. In Fig.36, the results for the torsional coordinate and the state population are shown for a different number of trajectories (with $\theta_{34}^{diff} = 20^\circ$). For the torsional coordinate, it turns out that the initial sampling for a small number of trajectories is already quite accurate and differs only by about $\approx 1.0^\circ$ compared to the sampling using more trajectories. Increasing the number of trajectories to 500 leads to a very good initial sampling. The dynamics of the torsional coordinate for a small number of trajectories is as expected but does not show a smooth dynamics. Using a total number of 3000 trajectories, a very good initial sampling of the torsional coordinate and a smooth torsional dynamics is achieved. For the Frenkel state population shown in Fig.36b, a more drastic dependency on the number of trajectories is observable. For 10 trajectories, a very noisy state population is noticeable. This noise is significantly reduced for a higher number of trajectories. For 3000 trajectories, a very smooth population dynamics with only minor statistical fluctuations is observed. Nevertheless, already a small number (e.g. 500) of trajectories reproduce the correct Frenkel state dynamics on a long time scale. Based on these results, it is assumed that 3000 trajectories are sufficient for converged Ehrenfest results. Therefore, the benchmark of the hexamer-type system is based on 3000 independent Ehrenfest trajectories using an integrator step-size of 1.0 a.u.

5.4.2.2 Benchmark Calculation for a PPV hexamer

The results of the benchmark calculations for the PPV hexamer are shown in Fig.37-39. All parameters and initial conditions are identical for the Ehrenfest and the MCTDH setup, except the fact that a Langevin type description is used for the dissipative environment in the Ehrenfest approach. Here, the friction coefficient is chosen to be identical to the MCTDH calculations, while thermal fluctuations are neglected ($T=0$ K). As shown in Fig.37a-d, the dynamics of the active coordinates and the state populations are almost the same.

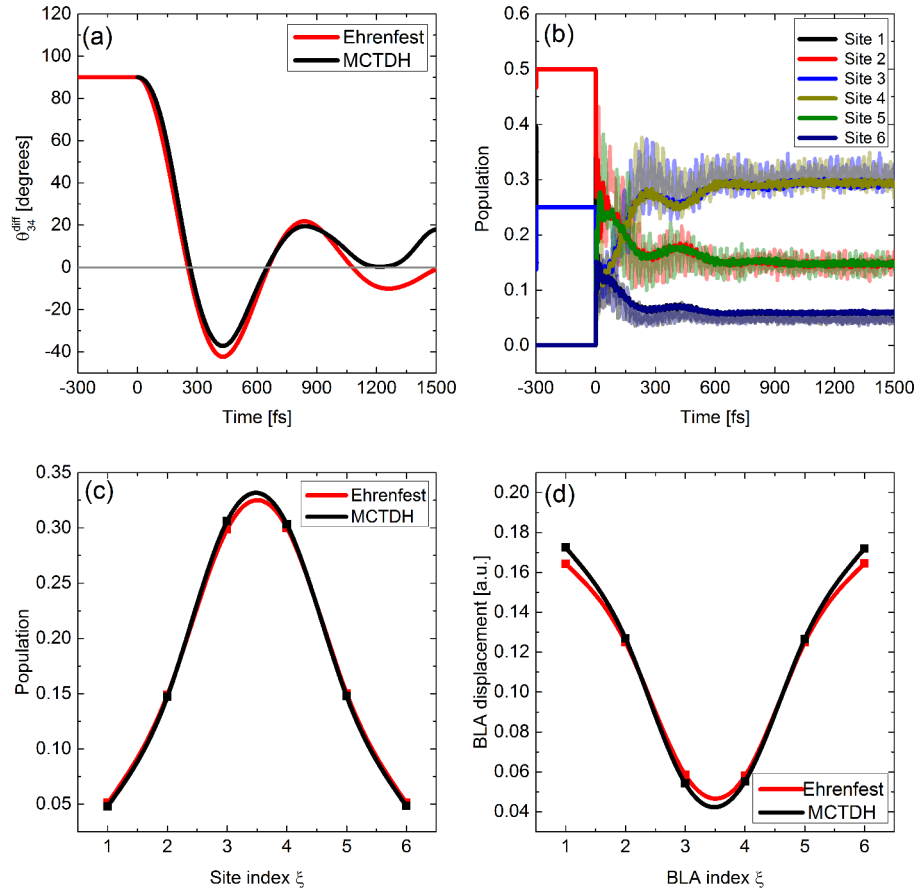


Figure 37: Expectation values of the MCTDH and Ehrenfest results for (a) the torsional coordinate θ_{34}^{diff} (b) the time-evolution of the Frenkel state population (c) the Frenkel state population for the stationary state and (d) the BLA displacement for the stationary state (for symmetric reasons, two BLA coordinates on one monomer unit are shown as one averaged BLA coordinate). The Ehrenfest results are coloured red (Fig.a,c,d) while in Fig.b, the light colors correspond to the MCTDH results.

For the torsional coordinate θ_{34}^{diff} a very good agreement up to ≈ 1000 fs is observable. The torsional coordinate θ^{diff} shows a damped dynamics towards the excited state minimum values of 0° . The dynamics of the Ehrenfest method differs

from the MCTDH results for times greater than 1000 fs. In general, the discrepancy of the torsional coordinate is very small and especially for longer times, the Ehrenfest results seem to be more reliable, since the expected damped dynamics are smoother for these times. Comparing the Frenkel state population shown in Fig.37b, a very good agreement of both methods is observable. The dynamics of the Frenkel states show a very fast oscillatory signature within the first 300 fs, followed by a slower formation of a stationary state within ≈ 900 fs (also called local excitonic ground state (LEGS)). In contrast to the Ehrenfest Frenkel state populations, the MCTDH state populations seem to oscillate in a more coherent fashion.

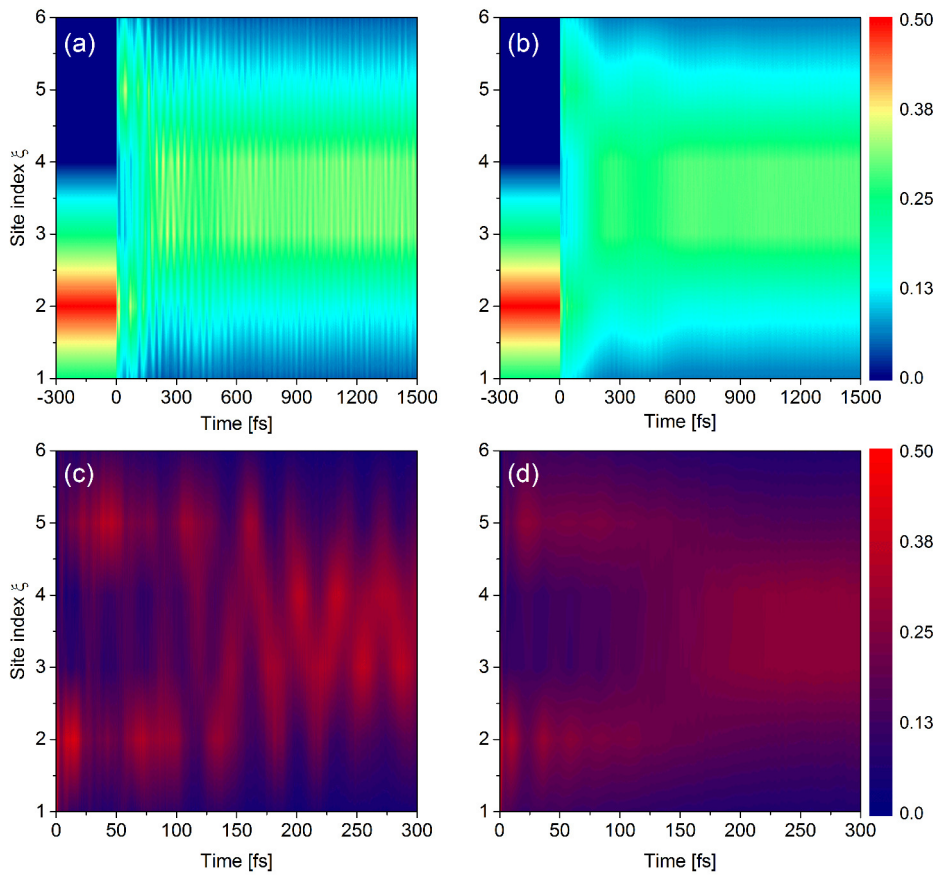


Figure 38: Site- and time-resolved Frenkel state population of the PPV hexamer. (a) Results of the MCTDH method up to 1500 fs, (b) results of the Ehrenfest method up to 1500 fs, (c) results of the MCTDH method up to 300 fs and (d) results of the Ehrenfest method up to 300 fs. For a more improved visualization of the state population, a different color-coding is used for panel c and d. The absolute scale of the population does not change.

Nevertheless, the absolute value of the Frenkel state populations for the LEGS shown in Fig.37d shows a very good agreement between both methods. Also, the trapping effect of the BLA coordinates is well described by both methods for the

stationary state. Analyzing the Frenkel state population on different time scales, a large discrepancy can be found for the first 300 fs. As shown in a 3-D representation in Fig.38a and b, a clear trapping of the Frenkel state population centered in the middle of the lattice is observable by both methods within 1.5 ps. Comparing the first 300 fs shown in Fig.38c and d, it turns out that the state populations given by the MCTDH method show an ultrafast, compact and well localized population transfer from one end of the lattice to the other end of the lattice. Up to 150 fs, well separated population spots are observable and the formation of the LEGS begins after this time. In contrast to these results, the Ehrenfest results of the EET on this time scale do not show this well defined dynamics.

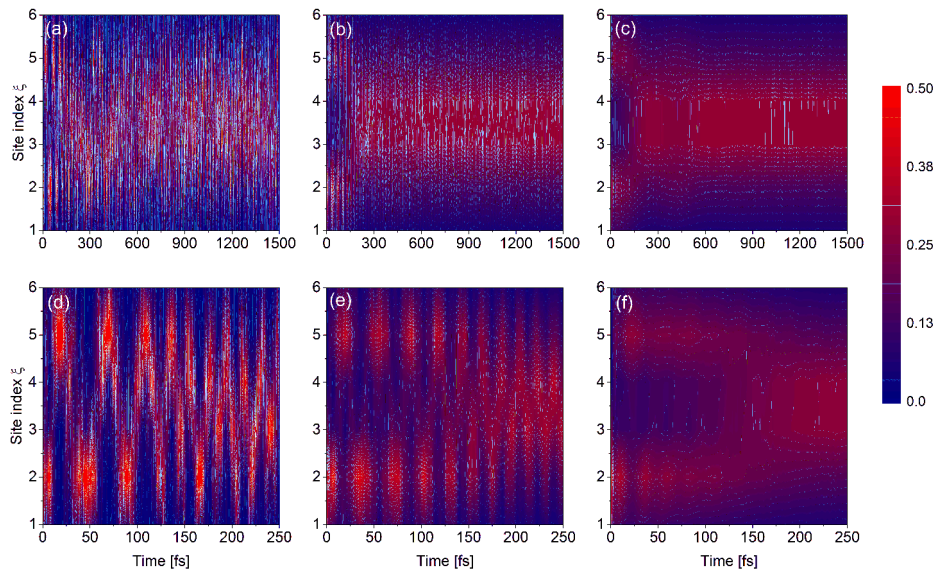


Figure 39: Comparison of the Frenkel state population for the TDH, MCTDH and Ehrenfest method. (a + d) TDH results, (b + e) MCTDH results and (c + f) Ehrenfest results. The scale and the color bar are identical for all data.

For the Ehrenfest approach, certain traces of this compact EET transfer from one end of the lattice to the other end are recognizable but the details of the oscillatory transfer can only be assumed. Indeed, it is possible to identify the compact Frenkel population at certain times on the lattice but in general, the Frenkel state population seem to be more blurred. Nevertheless, the clear formation of the stationary state can be observed on the same time scale as for MCTDH. To verify this result, an additional comparison of the Frenkel state population using the Time-Dependent Hartree (TDH) method is performed. As shown in Fig.39, the overall agreement between the TDH method and the MCTDH method shows a strong mismatch, whereas the agreement between Ehrenfest and MCTDH is very good. Interestingly, the TDH method describes the ultrafast and well localized

Frenkel population transfer from one end of the lattice to the other end on the short time scale very well but fails for the description of the formation of the LEGS [188]. Clearly, the TDH approach captures electronic-nuclear correlation that lead to LEGS formation less well than the Ehrenfest approach. These results allow the conclusion that the semi-classical Ehrenfest approach is able to reproduce the results of the full-quantum MCTDH approach, for classical coordinates and electronic DOF, with the limitation that the first 150-300 fs of the electronic populations are not perfectly reproduced. The blurred electronic population could be an artifact of the averaging procedure, which is needed to calculate the expectation values. Nevertheless, the great advantage of the Ehrenfest method is the explicit description of temperature at limited computational expense and the thereby associated possibility to study the effect of temperature on the energy transfer dynamics. Furthermore, the Ehrenfest method and the Langevin-type description do not underlie the restriction of a Poincaré recurrence time, which allows the simulation of longer time scales. Using the Caldeira-Leggett model, a longer simulation time can only be achieved by using a smaller frequency spacing $\Delta\omega$ of the bath modes. This will result in a less accurate description of the dissipative dynamics using the same number of bath modes and can only be compensated by using more bath coordinates (which will result in a much increased computational effort). Finally, comparing the computational effort of the calculations, a converged Ehrenfest calculation costs much less compared to the MCTDH method. In theory, the independent Ehrenfest trajectories allow a linear scaling with the number of trajectories, since all trajectories can be calculated at once. The computational time of one trajectory for the PPV hexamer is in the range of 1-5 minutes for a propagation of 1.5 ps (depending on the integrator step-size). In practice, this scaling is limited by the computational resources, but on large HPC clusters, a massive speed up in the total computational time can be achieved. In practice, the total time of the Ehrenfest calculation is about 1 hour (or less) for 3000 trajectories, whereas the ML-MCTDH method takes about 19 hours (the normal MCTDH method takes ≈ 127 hours).

5.4.2.3 Density Matrix Description of an Irreversible Transfer Dynamics using the Ehrenfest Method

All results shown so far are based on a wave function type description. This description has the disadvantage that only pure states can be described by the electronic wave function. To overcome this drawback, a density based formulation can be used. This ansatz allows the description of pure and mixed states. As explained in Chp.3, the Liouville-von Neumann equation is used to describe the time evolution of the density. Another advantage of the density-type description is the possibility to describe the dynamics of irreversible transfer processes given by a non-Hermitian Hamiltonian.

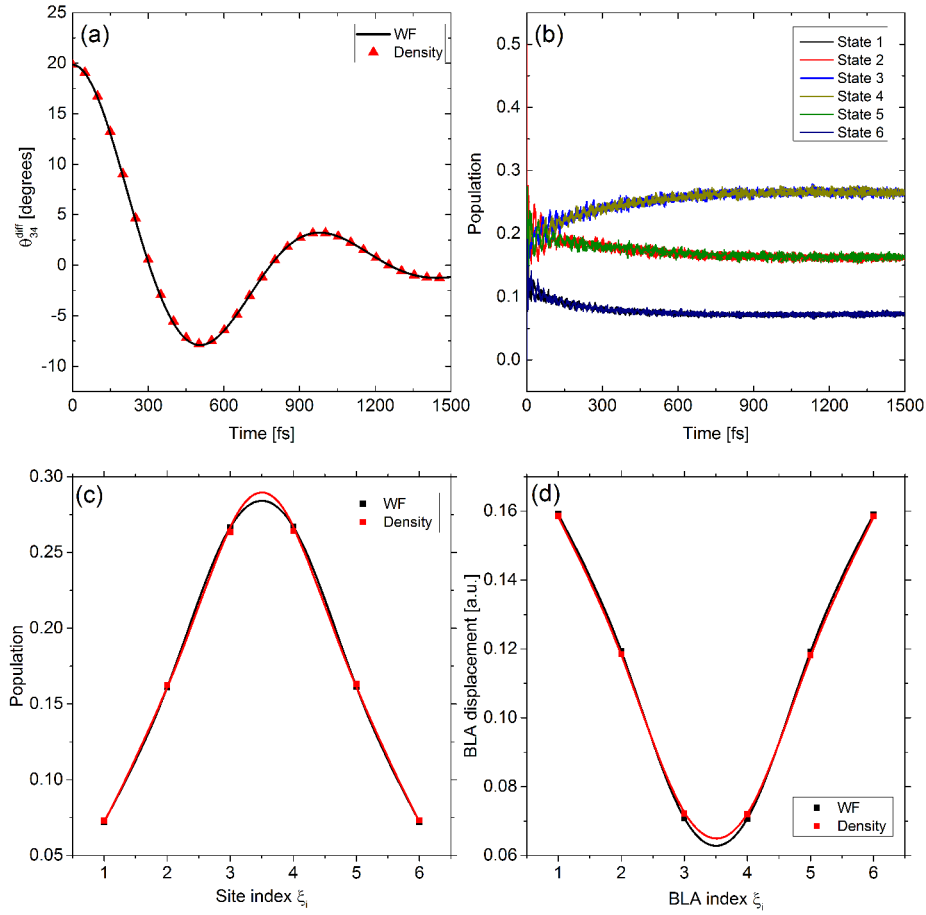


Figure 40: Comparison of the wave function based Ehrenfest results to the density based results. (a) torsional coordinate θ_{34}^{diff} , (b) Frenkel state populations, (c) BLA displacement for the quasi-stationary state (for symmetric reasons, two BLA coordinates on one monomer unit are shown as one averaged BLA coordinate) and (d) Frenkel state population for the quasi-stationary state.

In the following, the density matrix ansatz of the Ehrenfest method will be compared to the wave function based Ehrenfest approach in the absence of an irre-

versible transfer. As shown in Fig.40, the overall agreement of the torsional and the BLA coordinates is very good. Also for longer times, the discrepancy of both methods for the coordinates is almost zero. Further, the Frenkel state dynamics is almost identical. Comparing the results for the new LEGS, small discrepancies of the Frenkel state population and the BLA values can be observed. Nevertheless, these discrepancies are very small and could be related to the different type of integrator used for the density matrix ansatz (see the following paragraph for an explanation).

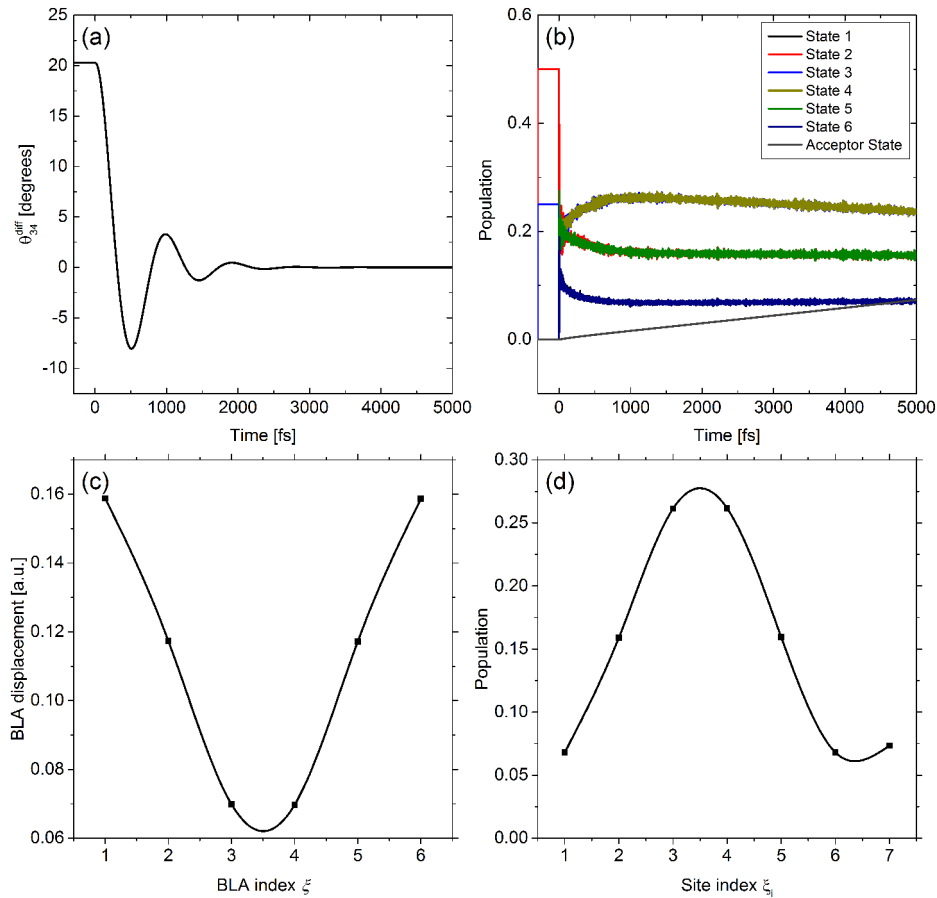


Figure 41: Dissipative dynamics on a PPV hexamer type lattice linearly and irreversibly coupled to a trapping state with $\Upsilon=0.000005$ a.u.. (a) Dynamics of the torsional coordinate θ_{34}^{diff} (b) Frenkel and acceptor state population dynamics (c) Displacement of the BLA coordinate ξ (for symmetric reasons, two BLA coordinates on one monomer unit are shown as one averaged BLA coordinate) for the stationary state and (d) State population for the stationary state.

As a proof of principle, the irreversible energy transfer dynamics in a PPV hexamer connected to a trapping state is calculated. In the current setup, the last state of the PPV hexamer system is linearly coupled to an absorbing state. This state can

be understood as a trapping state of the system e.g. a state describing the final $e-h$ separation at an interface in terms of an irreversible dissipative process.

Using a non-hermitian Hamiltonian, the numerical stability of the integration routine becomes very challenging: to be norm-preserving, a small integrator step-size is needed. Also the numerical integration only works for very low coupling values. The solution to this problem is to perform the integration using an asynchronous leap frog algorithm (this algorithm has a larger area of stability) [140]. As a proof-of-concept the irreversible coupling value is set to $\Upsilon=0.000005$ a.u. (0.136056 meV). As shown in Fig.41, the overall dynamics up to 5.0 ps is very similar to the dynamics described above in the absence of an irreversible coupling. The torsional dynamics shown in Fig.41a illustrates the expected damped dynamics resulting in a planar structure within 1.5 ps. Again, two different time scales can be observed: a rapid dynamics within the first 500 fs followed by a slower dynamics resulting in the planar structure. A trapping event on the lattice is again observable via the state population or the BLA displacement shown in Fig.41b-d. In addition to the Frenkel population, the population of the trapped state (site index 7) is shown in Fig.41b and d. The dynamics of this state indicates the expected linear but weak increase resulting in an overall population of ≈ 0.075 after 5.0 ps. Simultaneously to the increasing trapping state population, the overall Frenkel state population is decreasing.

Due to these reasons, preference is given to the wave function based Ehrenfest implementation.

5.4.2.4 Effect of Noise and Disorder on EET

As explained in Chp.3, the implementation of the environment and temperature is done via a Langevin type description. This description contains the temperature dependent random fluctuation term which is calculated using a norm-distributed random number centered around 0.0. For the implementation in the source code and the calculation of Ehrenfest trajectories, two different ways are possible: (i) use the same set of random numbers for all trajectories or (ii) use different sets of random numbers.

This apparently minor difference is very important for the obtained results. Especially the EET dynamics is strongly affected by the type of implementation. In the following, the effect of the implementation on the EET dynamics and the general effect of temperature and disorder on the EET dynamics will be analyzed. In order to illustrate the EET dynamics more realistically, the system size is increased to a PPV 20-mer. Additionally, all torsional and BLA coordinates are

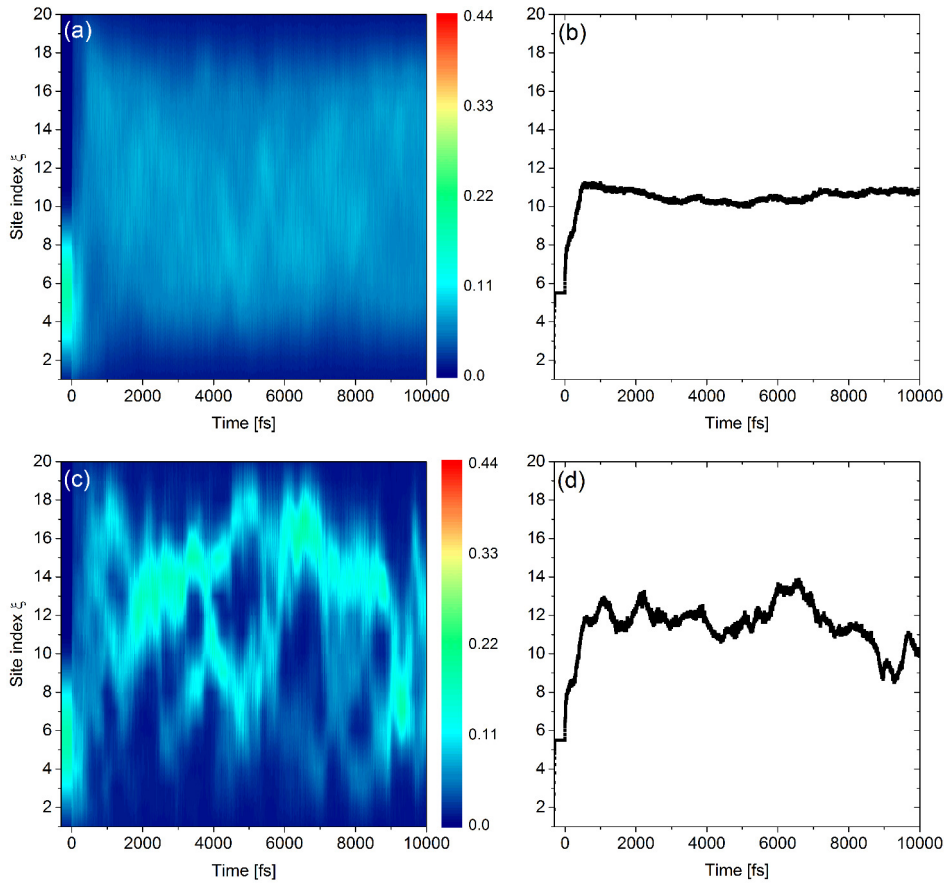


Figure 42: Analysis of the Langevin implementation on the EET transfer dynamics in the PPV 20-mer using a temperature of $T=100$ K. (a) Frenkel state population up to 10.0 ps using different random numbers for every trajectory (b) Mean Frenkel state population for different random numbers (c) Frenkel state population using the same set of random numbers and (d) the corresponding mean Frenkel state population.

described as active coordinates. Again, a kink centered in the middle of the lattice is implemented described by a torsional angle $\theta_{1011}^{diff}=90^\circ$ while all other torsional angles are set to their ground state values. The initial wave function is prepared by relaxing an arbitrary wave function on the left site of the kink (state 1- 10) via negative imaginary time propagation. The so generated LEGS is used as an initial condition for the propagation.

In Fig.42, the effect of different implementations on the EET dynamics on the PPV 20-mer lattice is shown. The dynamics of the Frenkel states shows a very strong discrepancy depending on the different noise setups. For the implementation using the same random numbers (and thus the same bath realization) for all trajectories, a well defined and compact exciton dynamics on the overall lattice is observable starting from the prepared initial state as shown in Fig.42c. For the first ≈ 800 -1000 fs, the exciton dynamics looks blurred but after this time, a com-

compact exciton is formed. This compact exciton randomly moves on the lattice and at certain times, a splitting of the exciton is observable e.g. after 3.0 ps. The two exciton packets move independently from each other until they recombine after ≈ 7.0 ps. An additional evidence for the transfer dynamics on the overall lattice is shown in Fig.42d. Here, the mean Frenkel state population is shown. This mean value indicates that the population moves rapidly from its initial position centered between monomer 5 and 6 to the center of the lattice. After this rapid dynamics from the initial position, a strong fluctuating dynamics centered in the middle of the lattice is observable. In contrast to these observations, the EET dynamics using different random numbers shows a different picture. As shown in Fig.42a, no compact exciton dynamics is observable. For this implementation, it is also observable that the whole lattice is populated but in contrast to the dynamics described for the same random number, only a blurred population is observable. This is also indicated by the mean Frenkel population shown in Fig.42b. The dynamics of the mean Frenkel state population show the same initial rapid dynamics from its initial position to the center of the lattice but in contrast to the dynamics described before, the mean population stays in the center of the lattice without the fluctuation described before.

The different observations depending on the random number generation can be explained by the following theory: the random fluctuation generated by the same bath for all trajectories shown in Fig.42c and d can be seen as a more quantum mechanical type description of a dissipative environment comparable to a Caldeira-Leggett type description. This type of implementation can be understood such that each single trajectory interacts with the same bath. This description is similar to a single-molecule experiment and therefore, this type of EET dynamics should be observed in a single-molecule experiment and agrees with the MCTDH results presented before. In contrast, using a different bath for every trajectory as shown in Fig.42a and b, each trajectory interacts with the environment in a different way and therefore, no compact exciton propagation is observable. This type of description is comparable to an experiment on a statistical ensemble and therefore, the observed exciton dynamics is a mean value of the overall ensemble. This interpretation of the different implementation of the Langevin bath allows the explanation of the very different EET dynamics.

In order to clarify the effect of thermal noise and structural disorder on the EET using the quantum like description of the Langevin bath, a systematic evaluation of the temperature and the torsional coordinates using the Ehrenfest approach is done. All torsional and BLA coordinates are described as active DOFs and the

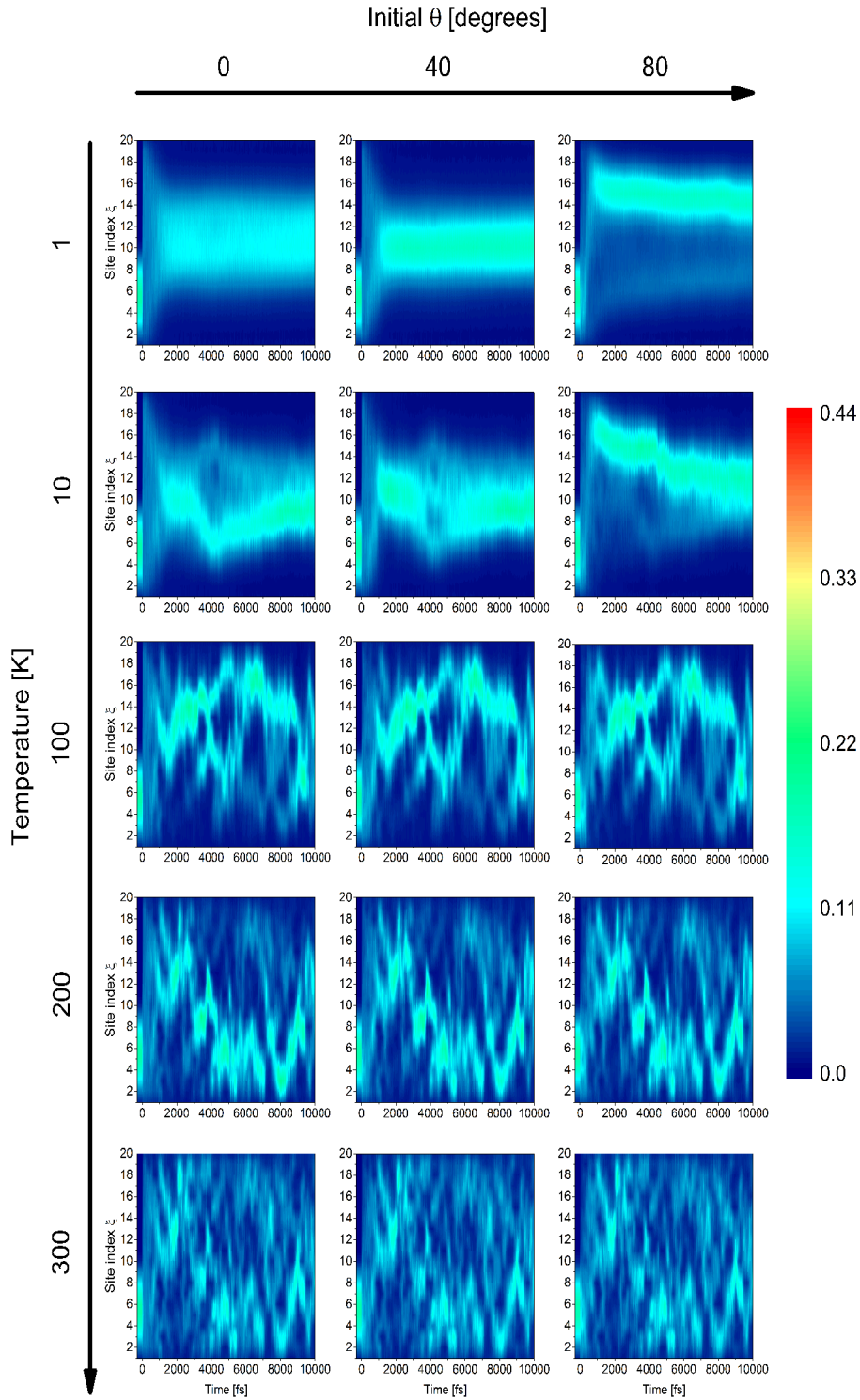


Figure 43: Effect of thermal noise and structural disorder on the EET dynamics. Each row corresponds to one temperature and each column to one initial θ value. Starting from the first row, the temperatures correspond to $T=1$ K, 10 K, 100 K, 200 K and 300 K and the initial θ values to $\theta^{diff}=0^\circ$, 40° , 80° . The absolute scale is identical for all plots and indicated by the color bar on the right side.

number of trajectories is always 3000. The focus of the analysis will be on the EET. In Fig.43, the results of the systematic scan are shown. The results show a clear correlation between the temperature and the observed EET dynamics.

For low temperatures, the exciton dynamics show a very pronounced trapping effect of the exciton. For $\theta^{diff} = 0^\circ$ and 20° , a trapping centered in the middle of the lattice with 1.2 ps is observable resulting in a new quasi-stationary state. In contrast, for $\theta^{diff} = 80^\circ$, a rapid shift of the exciton packet within 1.2 ps from one end of the lattice to the other end is observable. The exciton then forms a compact packet and slowly relaxes towards the middle of the lattice. Increasing the temperature to 10 K, a slightly different dynamics is observable: for all initial θ^{diff} values, the overall dynamics is similar to the 1 K case but the previously observed compact exciton seems to be more blurred and broadened. For temperatures higher than 10 K, a completely different EET dynamics is observed. Now, a very fast initial exciton dynamics on the overall lattice within the first 1.0-1.5 ps resulting in a new compact exciton wave packet is observed. This compact exciton then starts moving on the overall lattice. At certain times, an exciton splitting into two separate exciton wave packets is observable which recombines at a later time. The effect of a higher thermal noise is nicely observable for 200 K and 300 K: for 200 K, a compact exciton packet is observable up to 10.0 ps. In contrast, the compact exciton is still observable at 300 K at certain times but the exciton is splitted into more individual exciton packets, which recombines or splits again. The overall exciton population seems to be more spread out on the overall lattice compared to the dynamics at 200 K (or 100 K). In general, the influence of the initial θ^{diff} value and the associated disorder is not as high as one would expect. An effect can be seen for low temperatures (1 K and 10 K) but for a higher disorder, the effect of the thermal noise is much stronger.

5.4.2.5 Exciton Trapping

The systematic analysis of the structural disorder and the effect of thermal noise indicate a strong correlation between the observed exciton dynamics and these parameters. Furthermore, the effect of different descriptions of the environments has been shown. Until now, it is still unknown why this compact exciton packet is observed, why the effect of temperature can be so drastic and what is the role of the BLA and torsional coordinate for the compact dynamics. To answer this question, the population dynamics and the corresponding total energy of each monomer site is analyzed for the PPV 20-mer model system. The initial θ^{diff} value is 40° and the initial wave function is prepared as explained in the previous

sections. To distinguish the contributions of both coordinates, the torsional or the BLA coordinate are not included in the propagation (fixed coordinates) and a reference calculation with all active coordinates is done. To exclude sampling effects, all initial conditions for a given temperature are identical for the three different setups. In Fig.44, the results for $T=1$ K are shown.

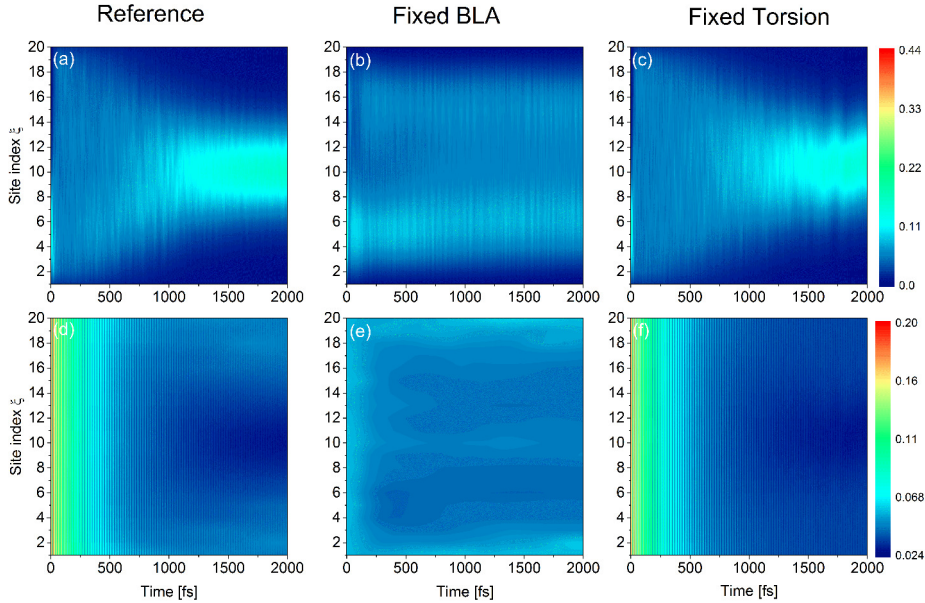


Figure 44: Analysis of the exciton dynamics and the exciton self-trapping effect at $T=1$ K. Upper row: exciton dynamics for (a) reference calculation (b) fixed BLA coordinates and (c) fixed torsional coordinates. Lower row: total site energy for (a) reference calculation (b) fixed BLA coordinates and (c) fixed torsional coordinates. For the upper row, the population is indicated by a color-bar, which is identical for all graphs and given on the right. For the lower panel, the site energy is color scaled with a maximum value of 0.2 eV for all graphs. Please note that for a better illustration, the minimum value of the color-bar changes.

The population dynamics shown in the upper row indicates a clear trapping effect centered in the middle of the chain for the reference calculation and the system with fixed torsional coordinates. For fixed BLA coordinates, only a less pronounced exciton trapping effect centered on the initial sub-fragment is observable. In this case, the overall lattice is populated, whereas for fixed torsional coordinates, a compact exciton is observed. Nevertheless, a clear difference between the exciton dynamics shown in Fig.44a and c is depicted: the dynamics shown in Fig.44c includes much stronger fluctuations. These observations strongly correlate with the total site energy of the lattice. As shown in the lower row of Fig.44, a minimum in total energy centered in the middle of the lattice is observable for the reference calculation. A similar minimum can be found for fixed torsional coordinates, whereas for fixed BLA coordinates, no minimum is found.

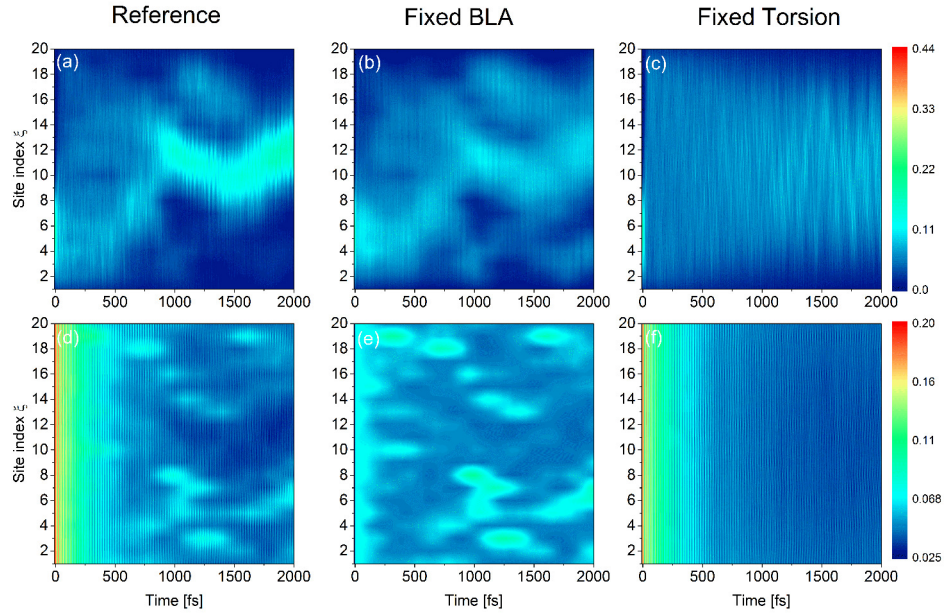


Figure 45: Analysis of the exciton dynamics and the exciton self-trapping effect at $T=100$ K. Upper row: exciton dynamics for (a) reference calculation (b) fixed BLA coordinates and (c) fixed torsional coordinates. Lower row: total site energy for (a) reference calculation (b) fixed BLA coordinates and (c) fixed torsional coordinates. For the upper row, the population is indicated by a color-bar, which is identical for all graphs and given on the right. For the lower panel, the site energy is color scaled with a maximum value of 0.2 eV for all graphs. Note that for better illustration, the minimum value of the color-bar changes.

Performing the same analysis for $T=100$ K, a different result is obtained. As shown in Fig.45, the exciton dynamics of the reference calculation indicates a clear and compact exciton propagation over the overall lattice. By fixing the BLA coordinates, a still compact exciton propagation is formed but the absolute population values are less than in the reference system. Also the exciton packet itself seems to be more blurred. A completely different dynamics is observed for fixed torsional coordinates. In this case, no compact, well defined exciton packet is observable and no clear exciton dynamics is observable. The initial population is spread over the whole lattice and does not indicate any trapping behavior. Analyzing the total site energy as it is shown in Fig.45d-f, an explanation for the different observations can be found. In the case of the reference system, a minimum path is found but also local energy maxima. The observed exciton dynamics is directly linked to this energy map and follows the minimum energy path. In case of fixed BLA coordinates, a similar energy map is shown, which correlates to the exciton dynamics. For fixed torsional coordinates, no energetic minimum pathway is observed. This observation is in agreement with the exciton dynamics for fixed torsional coordi-

nates. These observations lead to the conclusion that both types of coordinates, the low frequency torsional coordinate and the high-frequency BLA coordinate are important for the observed exciton dynamics. In general, the BLA coordinates are essential for the formation of a compact exciton as shown in Fig.44c for the low-temperature case. In contrast, the torsional coordinate is essential for the formation of a minimum energy pathway as illustrated in Fig.45e for higher temperatures. The large change in energy and the formation of local maxima and minima is related to the strong changes in the torsional coordinate and the corresponding potential energy induced by thermal noise. It is also observable that the exciton dynamics is not as compact as in the reference calculation. Therefore, it can be stated that for a compact exciton dynamics, both coordinates are essential, the BLA coordinate for the compact exciton formation and the torsional coordinate for the propagation on the lattice. These findings also explain the observed dynamics in a high temperature regime: for high temperatures (e.g. 300 K as shown in Fig.43), the thermal noise induces very strong structural disorder and fluctuations. Especially the stronger fluctuations in the torsional coordinate create a 'hot' energy surface with no clear minimum energy pathway. This 'hot' energy surface avoids the formation and propagation of a compact exciton.

5.4.3 Conclusion

The data presented for the exciton dynamics on a PPV lattice using the MCTDH and the semi-classical Ehrenfest approach show some remarkable results. On the one hand, it is shown that the semi-classical Ehrenfest method is able to reproduce the results obtained by the full quantum MCTDH method very accurately. This is remarkable, since for other type of systems, the semi-classical Ehrenfest method fails [197, 204, 205]. Interestingly, the nuclear motion is reproduced at a very accurate level for all time scales while the dynamics of the electronic sub-system is described very accurately for longer times but shows discrepancies on a shorter time scale. On the short time scale, the semi-classical Ehrenfest method has a lower temporal and spatial resolution which results in a more blurred dynamics of the electronic sub-system. One approach to overcome this problem is to use more configurations by using a multiconfigurational Ehrenfest ansatz (as described by Shalashilin et al. [128, 129, 206] or Römer et al. [130]). This approach allows to consider coherence effects on the short time scale and eventually describes the electronic dynamics on this time scale correctly. Ensuing from the very good agreement (especially on a longer time scale), the Ehrenfest method allows the description of larger systems which need a high computational effort using MCTDH

(it is also possible that the number of configurations is too large to be handled by MCTDH). On the other hand, using the Langevin description in combination with the Ehrenfest approach, explicit temperature effects on the EET can be studied. It is shown that the effect of thermal noise is necessary for the observed exciton dynamics. The thermal noise scales the structural disorder of the system and especially the torsional disorder is essential for a compact exciton propagation. In combination with the high-frequency BLA coordinates, a minimum energy path is formed. For very low temperatures, this minimum energy path is located in the middle of the lattice and does not show a strong response on thermal noise. This dynamics of the minimum energy path leads to the formation of a new LEGS on a longer time scale. In contrast, the dynamics for higher temperatures shows a very strong response to thermal noise. As already mentioned, the thermal noise induces high changes in the monomer total energy. These changes allow a compact exciton dynamics on the overall lattice whereas for very high temperatures, the compact dynamics is not observable due to the chaotic torsional dynamics. This observation is in disagreement with the theory of Stafstrøm et al. that the exciton propagation shows a strong dependency on the initial structure (as described in Chp. 8 in Ref.[199]). In contrast to Stafstrøm, temperature and structural disorder are described as explicit and independent parameters.

Furthermore, in a proof-of-principle study the extension of the wave function based Ehrenfest method to a density matrix representation including irreversible dissipative dynamics has been demonstrated. This extension allows the description of irreversible processes and also points out the problem of numerical integration of these type of systems.

5.5 Photoinduced Vibrational Energy Transfer in a DTE-BODIPY System

As shown in the last two sections, photochemistry plays an important role in developments related to organic photovoltaics. Another important aspect of photochemistry is the control of photoreactions by light. Using light as a trigger in an appropriate system, a photoreaction can be induced in a controlled way, e.g., as exemplified by the photoisomerization of azobenzene. The system we want to study in this chapter is a dithienylethene (DTE) molecule linked by a rigid bridge to a boron-dipyrromethene (BODIPY) molecule [42]. DTE is a widely used photoswitch with a well defined absorption range for the isomerization process [207–209]. In turn, BODIPY is a well known fluorescent dye [210]. In the molecule under study, DTE acts as a donor-type moiety whereas BODIPY acts as an acceptor-type moiety. Both molecules are electronically decoupled and have a well defined excitation wavelength. The general idea is to develop a new type of material with the following properties: (i) a well defined 'ON' or 'OFF' state defined via structural changes and (ii) a state-dependent energy transfer or fluorescence. This concept is illustrated in Fig. 46.

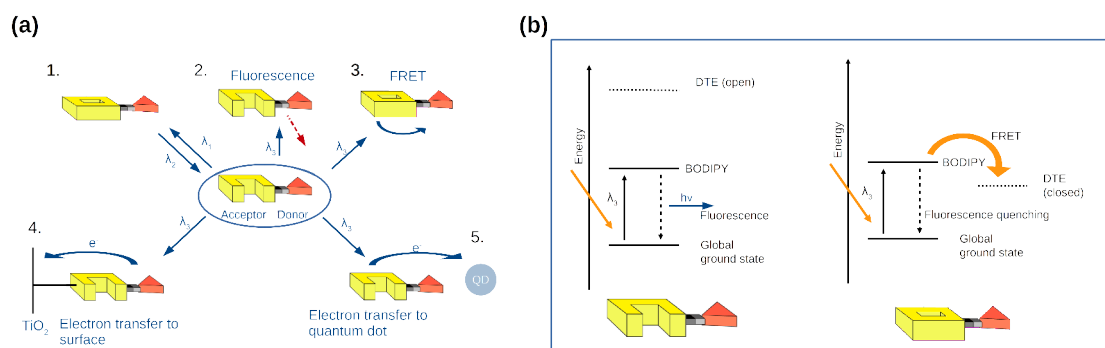


Figure 46: Concept of the DTE-BODIPY system for the application as a state sensitive molecule. (a) Possible wavelength and state-dependent pathways of the DTE-BODIPY dyad and (b) Energetic representation of the fluorescence quenching mechanism for the open and closed DTE molecule after photoexcitation of the BODIPY moiety.

As sketched in Fig. 46a, a variety of different reactions can take place depending on the wavelength of the light and the structural state of the molecule. As shown, the DTE molecule can be switched between an open/closed form using the wavelength λ_1 or λ_2 (1). This photoreaction is an ultrafast process with a high quantum yield and takes place on a sub-ps time scale. Applying a third wavelength on the BODIPY molecule while the DTE is in the open form, fluorescence of the BODIPY can be observed (2). Exciting the closed DTE form, a FRET process

from the BODIPY to the DTE is observed (3). The explanation for the different reactions is given in Fig.46b: in the open DTE form, the lowest excited state of the DTE molecule is above the lowest excited state of the BODIPY molecule whereas in the closed DTE form, the lowest excited state of the DTE is below the lowest excited state of the BODIPY. In the second case, the lower DTE state will act as a quenching state of the fluorescence and a FRET process from the DTE to the BODIPY takes place, while in the first case, a fluorescence of the BODIPY moiety is observed. This property can be used to either induce an electron transfer to a surface or to a quantum dot and has been proposed by various groups for different applications, e.g. a new type of storage system. The idea of using light, both as a trigger and as a photoswitch, has been developed by K. Rück-Braun et al. [11]. The group of Rück-Braun developed several types of molecules all containing a DTE molecule as a wavelength-dependent photoswitch and a BODIPY as an acceptor. For a better understanding of the state-dependent quenching process, time-resolved measurements of the ring-opening reaction of the DTE molecule in the full DTE-BODIPY dyad, as illustrated in Fig.47 have been performed by Schweighöfer et al. [42].

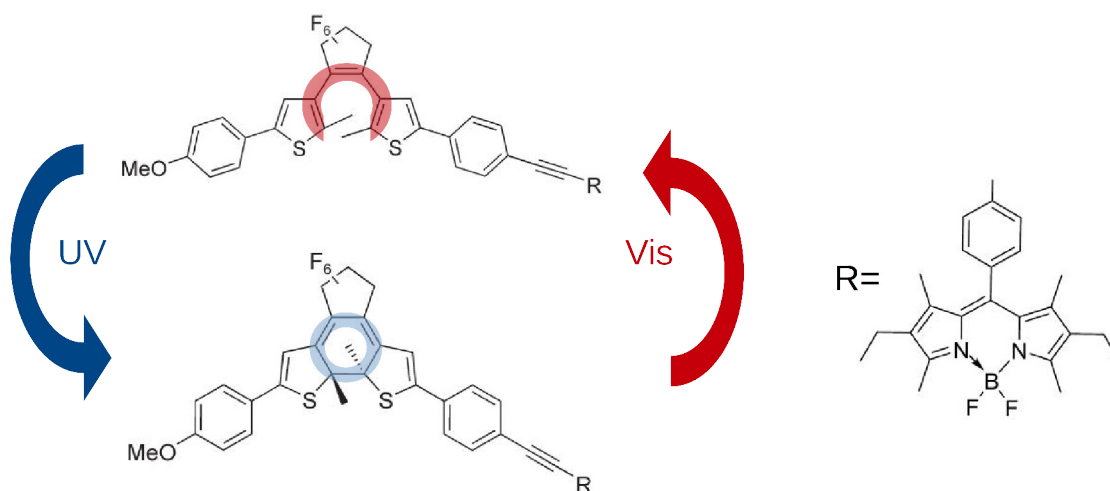


Figure 47: Wavelength-dependent ring-opening/closing reaction of the DTE moiety.

The results of the time-resolved UV/Vis measurements are shown in Fig.48. Interestingly, the measurements show an oscillatory signal at a probe wavelength of 530 nm after photoexcitation of the DTE molecule using a wavelength of 600 nm. An extensive analysis of the signal at this specific wavelength using a Fourier transformation indicates that two dominant vibrational frequencies are related to the observed oscillatory dynamics: one frequency centered around $\approx 80 \text{ cm}^{-1}$ and one frequency centered around $\approx 146 \text{ cm}^{-1}$. Surprisingly, the absorption spectrum of the open form and the photo-stationary state indicate that these signals are

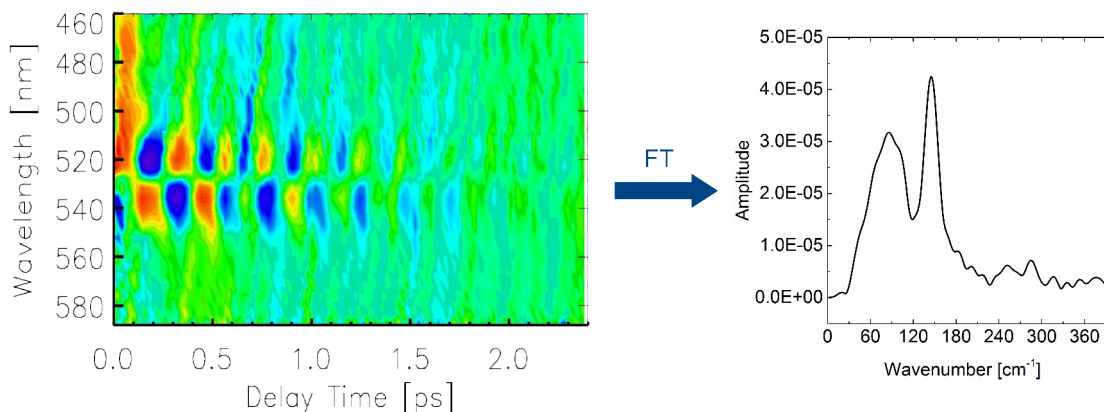


Figure 48: Experimental results of the fs time-resolved UV/Vis measurements of the ring opening reaction of the DTE-BODIPY dyad and the FT transformation of these data. The results of the Fourier transformation are shown for the probe wavelength of 539 nm. Blue indicates a negative signal, red a positive signal.

related to a BODIPY vibration and not to the DTE, which is unexpected, since the DTE was excited specifically and both molecules are electronically decoupled. To clarify why the BODIPY signal is observed, electronic structure calculations on the DTE-BODIPY dyad were performed to identify vibrational modes of interest in this spectral range. Furthermore, a model is developed to simulate the energy transfer using quantum dynamical calculations in terms of the competition of intra- and inter-molecular interactions.

5.5.1 Electronic Structure Calculations

The *ab initio* calculations were performed using the TDDFT method as implemented in the TURBOMOLE 6.4 program package [169] (the BHLYP functional [211–215] in combination with the 6-31G* [216, 217] basis set was used. This functional is known to give reliable results as shown in Ref.[218]).

The relaxed structure of the first excited state was obtained based on the relaxed ground state structure and is shown in Fig.49a.

The results of the geometry optimization indicate that in the ground state (grey), the DTE is twisted by $\approx 24^\circ$ with respect to the phenyl ring of the bridge, which is almost perpendicular to the BODIPY molecule. In the first excited state, a planarization of the DTE and the bridge is observed, whereas the changes of the BODIPY geometry are negligible. The perpendicular structure of the BODIPY and the bridge already indicate an electronically decoupled system, since the conjugated π -system is interrupted by this perpendicular structure. As shown in Fig.49b and c, the calculated electronic transitions are located either on the DTE moiety

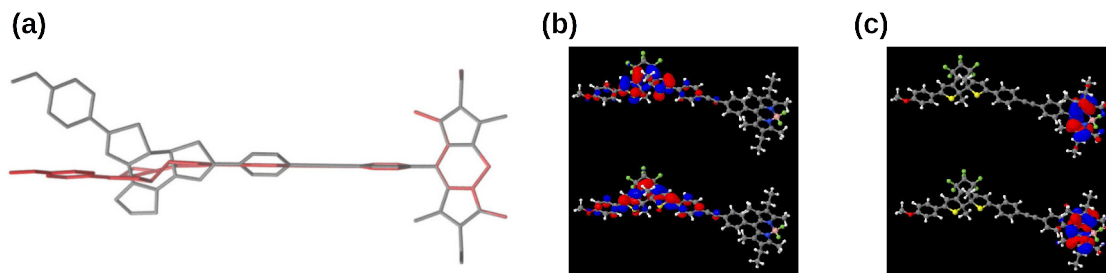


Figure 49: (a) Ground (grey) and excited state (red) structure of the DTE-BODIPY dyad. For clarification, the structures are overlaid on the BODIPY system and hydrogen atoms are not shown. (b) S_0 to S_1 excitation ($E_{exc.}=2.47$ eV) and (c) S_0 to S_2 excitation ($E_{exc.}=3.02$ eV).

(S1) or the BODIPY moiety (S2). This observation is in good agreement with the experimentally observed electronically decoupled states. The absolute values of the excitation energy differ from experiment by ≈ 1.0 eV, which is acceptable (no solvent effects are considered in the quantum chemical calculations), since the calculations did not focus on optimizing the excitation energy but rather on the effect of the vibrations on the excitation.

To identify and characterize the experimentally observed oscillations, the effect of each excited state normal mode on the S_1 to S_2 excitation energy is calculated (see Fig.50a for illustration; all frequencies were scaled by a factor of 0.945, which is the mean value of the standard HF and BLYP scaling factor [219]). Using a shifted harmonic oscillator model for the excited states, each vibrational mode i is shifted by a value x_i . The x_i value for the frequency i is obtained by applying the normalized displacement vector x_{norm}^i with a scaling factor a_i on the relaxed excited state structure x_0 . The scaling factor a_i is calculated using a harmonic potential such that

$$a_i = \frac{1}{x_{norm}^i} \sqrt{\frac{2E_{excess}}{k_i}} \quad (146)$$

with the excess energy E_{excess} describing the difference between the energy at the FC point and the minimum energy of the S_1 state. k_i is the force constant of the frequency i . This approach is directly comparable to the experimentally observed shift ΔE for the excitation wavelength. All parameters were extracted from the TDDFT calculations. Based on these shifted structures, the change in transition energy ΔE_i , as defined in Fig.50a, is calculated. The results of this procedure are shown in Fig.50b and demonstrate that at least three vibrational modes have a strong effect on the energy shift ΔE_i . Two of these frequencies are in very good agreement with the experimental observed frequencies (147.0 cm^{-1} and 97.0 cm^{-1}). To characterize these frequencies, the displacement of each frequency

is analyzed. As shown in Fig.51, the displacement of the lower frequency combines the displacement of the DTE and the bridge and an additional displacement of the phenyl rings of the bridge.

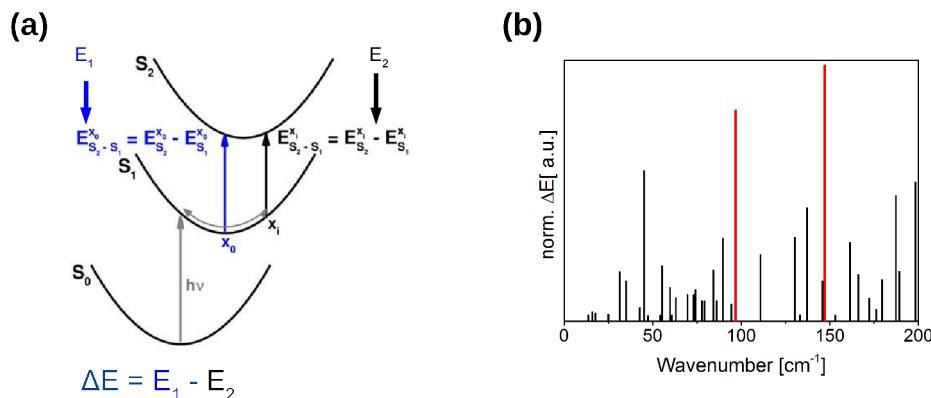


Figure 50: (a) Harmonic oscillator model to calculate the experimental observed energy shift ΔE_i for each normal mode i . (b) Calculated ΔE_i values for the molecular normal modes.

The frequency centered around 147.0 cm^{-1} also combines DTE and bridge planarization but also includes a strong displacement of the phenyl rings of the bridge towards the BODIPY.

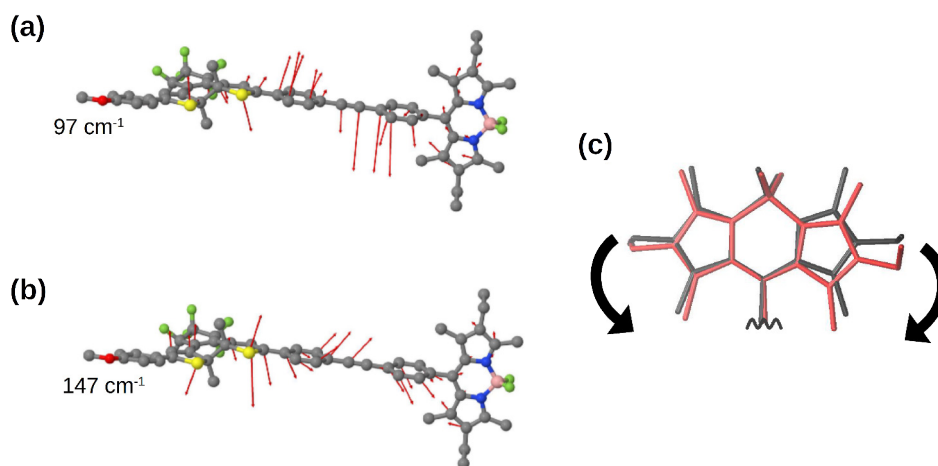


Figure 51: Displacement vectors of the modes at 97.0 cm^{-1} (a) and 147.0 cm^{-1} (b) which show a strong shift of the electronic excitation energy of the DTE-BODIPY dyad. (c) Displacement of the BODIPY system for the 147.0 cm^{-1} normal mode, illustrating a transfer of momentum to the BODIPY via the bridge. Red illustrates the displaced structure, grey the relaxed structure.

This displacement can be seen as an transfer of momentum via the rigid bridge from the DTE to the BODIPY, which is a completely unexpected result. Interestingly, a similar oscillatory dynamics has been experimentally observed for a different type

of molecule, which is also a photoswitch [220]. Here, the theoretical investigations have not only been used to identify the relevant normal mode but also to explain the effect of this vibration on a photoinduced ring-opening reaction.

Based on the theoretical investigation of the experimentally observed oscillatory signals presented up to here, only the origin of the observed oscillatory signal could be explained. No information about the competing dynamics of DTE local molecular relaxation processes or the coupling of the DTE to the BODIPY was considered. Therefore, a model for the description of the intramolecular vibrational energy redistribution (IVR) after photoexcitation from DTE to BODIPY is developed and studied in the context of the competition between the molecular relaxation process, the intra-molecular energy transfer and the inter-molecular interactions to e.g. a dissipative environment.

5.5.2 Model System

To describe the IVR process taking place in the DTE-BODIPY dyad after photoexcitation, an appropriate model has to be used. On the one hand, this model should describe the molecular geometry and the IVR of the DTE-BODIPY dyad under study sufficiently well, on the other hand, it should be small enough to be suitable for a quantum dynamical description. The challenge is to map the existing structure to such a model. In Fig.52, the mapping of the molecular structure to a model is illustrated.

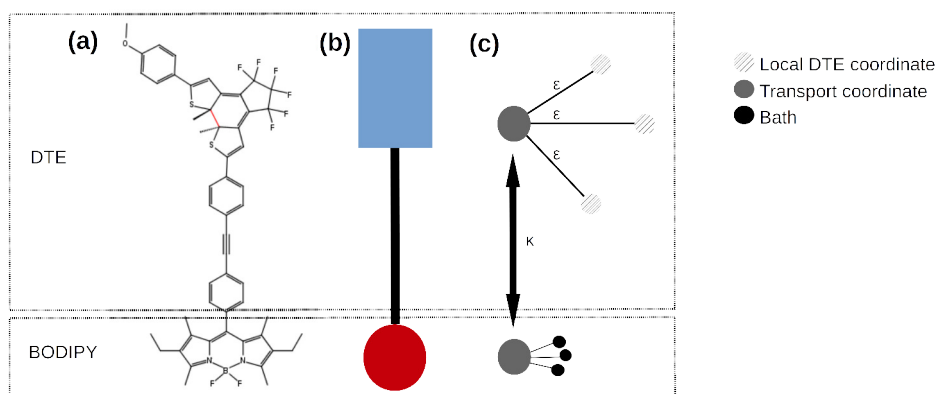


Figure 52: Mapping of the the DTE-BODIPY structure to a model for a quantum dynamical simulation. (a) Molecular structure of the DTE-BODIPY dyad. The red bond indicates the bond broken in the photoreaction. (b) Schematic representation of the DTE and the BODIPY fragment. (c) Schematic representation in terms of local vibrations described by coupled harmonic oscillators.

As a simple representation, the molecule is divided into two fragments: a DTE and a BODIPY fragment. Both fragments exhibit one main coordinate that plays the role of a transport mode, the two transport modes are linearly coupled. Furthermore, to include molecular relaxation processes taking place after photoexcitation, the DTE fragment contains a set of DTE local modes linearly coupled to the DTE transport coordinate. To include dissipation, the BODIPY transport coordinate is coupled to a harmonic oscillator bath. In general, all modes are represented by shifted harmonic oscillators. A similar model describing the IVR process in molecular chains has been used by, e.g., P. Hamm and M. Schade [37, 39, 40]. The mass-frequency weighted Hamiltonian is given by

$$H_{total} = H_{DTE} + H_{BODIPY} + H_{lin.coupl.} + H_{bath} \quad (147)$$

$$H_{DTE} = \sum_{i=1}^N T_i + \sum_{i=1}^N \frac{1}{2} \omega_i (x - x_0)^2 + \sum_{i=2}^N \epsilon x_1 x_i \quad (148)$$

$$H_{BODIPY} = T + \frac{1}{2} \omega (x - x_0)^2 \quad (149)$$

$$H_{lin.coupl.} = \frac{1}{2} \kappa (x_{DTE,1} - x_{BODIPY})^2 \quad (150)$$

$$H_{bath} = \sum_{j=1}^M T_j + \sum_{j=1}^M \frac{1}{2} \omega_j \left(x_j - \frac{c_j x_{BODIPY}}{\omega_j^2} \right) \quad (151)$$

with the kinetic energy operator T , the frequency ω and the DTE local coupling ϵ . N defines the total number of DTE local modes, whereas $i=1$ is the DTE transport coordinate and M defines the total number of bath modes. The Hamiltonian is parametrized using TDDFT results and spectral densities obtained from these calculations. The parametrization of the harmonic oscillator bath is performed using a discrete Ohmic spectral density $J_{Ohm} = 2\gamma\Delta\omega e^{-\omega/\Lambda}$. As illustrated in Fig.52, a local mode representation is used for the local DTE and BODIPY modes. To obtain these local modes, frequency calculations for the whole system with fixed atoms for the DTE or the BODIPY moiety are performed using the GAUSSIAN09 program package at the same TDDFT level of theory as described for the calculation of the excited states energies (this task can be performed in GAUSSIAN09 [221] by defining sub-fragments of the system and calculating the frequencies of the sub-fragments. In contrast, such a procedure is not possible using the TURBOMOLE program package). The advantage of this procedure is the fact that the complete system is calculated, but only local modes on the DTE or BODIPY moiety are considered. These modes can be directly mapped to the transport or local modes of the DTE and BODIPY moiety. The total number of DTE local modes is $N=51$; 1 transport coordinate and 50 local coordinates acting as a heat bath,

representing a hot excited state after FC excitation, whereby the local modes are represented by a discrete sampling of the spectral density obtained for the DTE fragment.

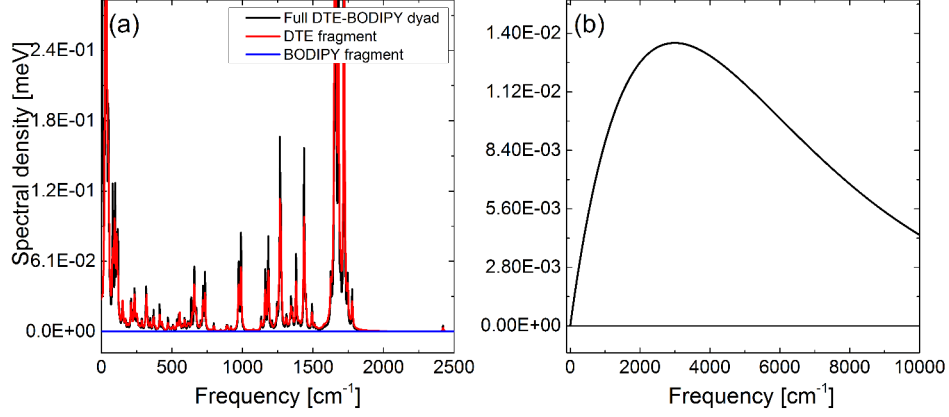


Figure 53: (a) Spectral density for the DTE (red) and BODIPY (blue) fragment for the first excited state. The spectral density of the overall system for the same state is shown in black. (b) Ohmic spectral density of the harmonic oscillator bath $J_{Ohm} = 2\gamma\Delta\omega e^{-\omega/\Lambda}$.

The discrete sampling defines the Poincaré recurrence time T_{PC} and is defined in such a way that the same T_{PC} is achieved as for the discrete sampling of the bath modes. The fragment based spectral densities calculated for the first excited state are shown in Fig.53 and illustrate on the one hand, the strong contribution of low frequency normal modes (spectral range between 0-500 cm^{-1}) and high frequency normal modes (spectral range between 1200-2000 cm^{-1}) and on the other hand, the lack of participation of the BODIPY modes which is due to the electronically decoupled nature of the DTE and BODIPY fragments. This is indicated by the almost zero contribution of the BODIPY spectral density for the whole spectral range in the first excited state. The local transport coordinates are represented as a linear combination of two fragment normal modes identified by inspection of the calculated normal modes. The linear combination of the two fragment based normal modes results in a reliable description of the experimental and theoretical observed normal mode centered around 147.0 cm^{-1} . As shown in Fig.54, the two fragment normal modes, centered around 150.0 cm^{-1} and 164.0 cm^{-1} , represent the normal mode of the full system quite accurately.

The mathematical description of this procedure is given by

$$\vec{v}_{Global} = c_1\vec{v}_{L1} + c_2\vec{v}_{L2} \quad (152)$$

with the displacement \vec{v} for the global and the local normal ($L_{1/2}$) modes. Additionally, the coupling value κ of the transport modes can be calculated using this

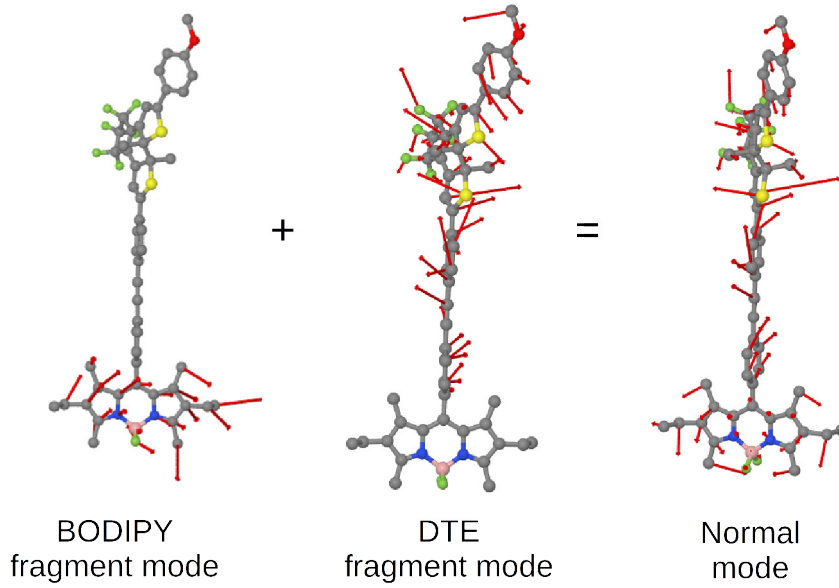


Figure 54: Representation of the theoretical and experimentally observed normal mode by linear combination of two fragment normal modes. The red arrows indicate the displacement vectors of the normal modes.

ansatz. This ansatz is similar to the ansatz of Reiher et al. [222–224], describing a transformation from uncoupled normal modes to coupled local modes. The general expression for this ansatz is

$$H_{Local} = U^T H_{Global} U \quad (153)$$

with the transformation/rotation matrix U and the diagonal matrix H_{Global} with $H_{ii} = \omega_{Global_i}$. The matrix H_{Local} contains the local mode frequencies and couplings with $H_{ii} = \omega_{Local_i}$ and $H_{ij} = \kappa$. This ansatz is used to calculate the coupling κ based on the coefficients c and the frequencies ω for the known local and global normal mode

$$H_{Global} = U H_{Local} U^T \quad (154)$$

or in a matrix type representation

$$\begin{pmatrix} \omega_1 & 0 \\ 0 & \omega_2 \end{pmatrix} = \begin{pmatrix} c_1 & c_2 \\ c_3 & c_4 \end{pmatrix} \begin{pmatrix} \omega_{L_1} & \kappa \\ \kappa & \omega_{L_2} \end{pmatrix} \begin{pmatrix} c_1 & c_3 \\ c_2 & c_4 \end{pmatrix} \quad (155)$$

From Eqn.155, κ can be calculated analytically. The coupling value ϵ of the local DTE modes to the DTE transport coordinate is calculated using the ansatz of Reiher et al. with the focus on the coupling value ϵ_i between the local modes and not on a good mode localization, since already well localized normal modes are

used as input parameter. From the obtained ϵ_i values, the averaged value of ϵ is calculated. In Tbl.7, all frequencies and coupling values are shown.

Table 7: Parameters of the DTE-BODIPY model Hamiltonian. If not specified, all parameters are given in cm^{-1} .

ω_{DTE}	ω_{BODIPY}	$\Delta\omega_{local}$	ϵ	κ
150.6	164.6	23.0	15.0	313.0
		T_{PC} [ps]	γ [fs^{-1}]	$\Delta\omega_{bath}$ [a.u.]
		1.4	300.0/500.0/750.0	$1.02 \cdot 10^{-4}$

Although the described procedure for the parametrization of the model Hamiltonian may seem unintuitive, it is the best method to calculate all needed parameters based on *ab initio* results. Furthermore, recent experimental results on different types of systems show that the numerical values of the calculated coupling values κ and ϵ are reliable [225].

5.5.3 Quantum Dynamics

The quantum dynamical calculations for the evaluation of the energy transfer process in the DTE-BODIPY dyad have been performed using the Heidelberg MCTDH package [123]. In order to simulate the FC excitation of the system and the following IVR process properly, an appropriate initial condition has to be used. Therefore, the system is assumed to be in the electronic ground state, which is defined via the harmonic oscillators in their global minimum. This is achieved by relaxing the initial MCTDH wave function of the overall system to the global ground state with $x_0=0.0$ for all coordinates. Due to the fact that the FC excitation is a DTE local event and that the excited state potentials are not identical to the ground state potential (here it is assumed that the frequency remains the same but the minimum of the excited state surface is shifted), only the DTE local coordinates have to be shifted by $x_0 \neq 0$. This shift is calculated using the spectral density of the DTE fragment and is directly coupled to the vibronic coupling κ_{vib} of an harmonic oscillator.

$$V_{harm.} = \frac{\omega}{2}(x - x_0)^2 \quad (156)$$

$$= \frac{\omega}{2}x^2 - \underbrace{\omega x_0}_{=\kappa_{vib.}} x + \frac{\omega}{2}x_0^2 \quad (157)$$

The vibronic coupling can be defined via the spectral density by

$$\kappa_i = \sqrt{2\omega_i \Delta\omega J(\omega)} \quad (158)$$

with the frequency ω_i , the discrete frequency interval $\Delta\omega$ and the spectral density $J(\omega)$. Finally, the shift x_0 is calculated by

$$x_0 = -\frac{\kappa_i}{\omega_i} \quad (159)$$

with the κ_i values obtained from the calculated spectral densities. Using these new x_0 values for the DTE local coordinates and $x_0=0$ for the BODIPY local coordinates, the FC excitation can be represented in a correct way.

The focus of the quantum dynamics is on the competition between the different parameters that can influence the IVR process and therefore, the following issues are addressed:

- What is the effect of the fragment-local, fragment-fragment and the dissipative coupling on the transfer dynamics?
- What is the contribution of the fragment-local modes to the energy transfer?
- Does the model system reproduce the experimental data?

To answer these questions, systematic variations of the different parameters are performed. In Fig.55a, the effect of a systematic variation of the site-local coupling values ϵ by a factor of 1.0, 0.5 and 0.1 is shown with respect to the initial energy of the DTE transport coordinate. The site-local DTE coordinates can be seen as a local heat bath created by the FC excitation.

As shown in Fig.55a, the scaled total energy of the DTE transport coordinate for a coupling value of $\epsilon=15\text{ cm}^{-1}$ increases drastically within the first ≈ 100 fs and reaches a maximum after ≈ 250 fs. This rapid increase in energy is followed by a damped oscillatory dynamics with ≈ 1.2 ps. An analysis of the total fragment energy of the DTE and the BODIPY moiety indicates the formation of a relaxed system within ≈ 1.2 ps after FC excitation, which is observable by the formation of a quasi-stationary state. The total energies shown in Fig.55b indicate a similar oscillatory dynamics as observed for the total energy of the DTE transport coordinate: a rapid increase of the total energy of the BODIPY fragment followed by a damped dynamics resulting in a quasi-stationary state, whereas the total energy of the DTE fragment is almost a mirror image of the BODIPY dynamics. As shown for lower ϵ values (7.5 and 0.15 cm^{-1}), the increase of scaled total energy of the DTE transport coordinate is much less compared to the normal coupling case and

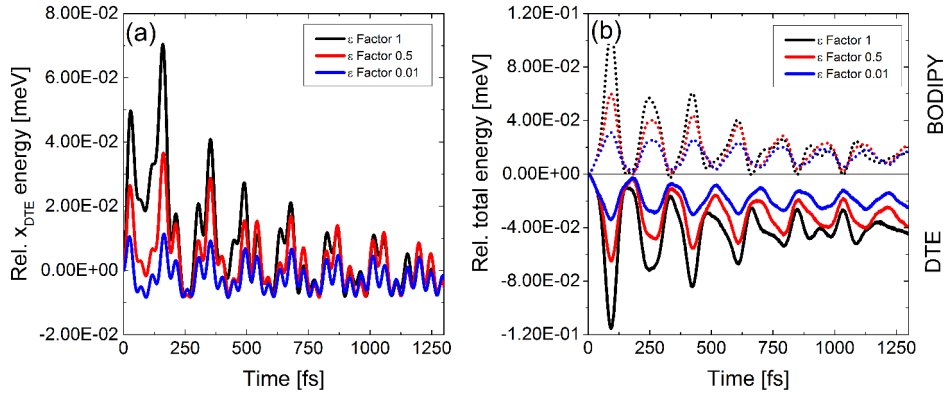


Figure 55: Effect of the fragment local coupling parameter ϵ on the energy transfer with $\kappa=313.0 \text{ cm}^{-1}$ and $\gamma=500.0 \text{ fs}^{-1}$. The variable $\epsilon=15.0 \text{ cm}^{-1}$ is scaled by a factor of 0.5 or 0.1. A positive signal indicates an increase in energy, whereas a negative signal indicates a decrease in energy. (a) Total energy of the DTE local transport mode and (b) Total energy of DTE and BODIPY fragment. The solid line indicates the total DTE energy, the dotted line the total BODIPY energy. The energies are scaled with respect to the initial energy at $t=0$.

also observable in the total energy of the DTE fragment. Nevertheless, for all values, the formation of a quasi-stationary state is observable within 1.2 ps while the effect of the low coupling is indirectly observable only in the decreased total energy of the BODIPY fragment transferred from the DTE for the first 250 fs. This dynamics indicates that the total energy transferred to the BODIPY fragment is strongly correlated to local coupling effects of the DTE fragment.

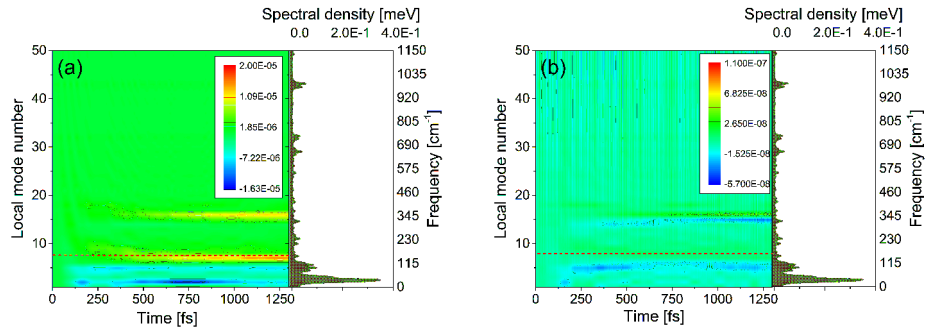


Figure 56: Total energy of DTE local modes. A positive signal indicates an increase in energy, whereas a negative signal indicates a decrease in energy. (a) $\epsilon=15.0 \text{ cm}^{-1}$ and (b) $\epsilon=0.15 \text{ cm}^{-1}$. The red line indicates the frequencies of the DTE and BODIPY transport coordinate. The color bar indicates a positive or negative energy change with respect to the initial total energy of coordinate i . The energies are scaled with respect to the initial energy at $t=0$.

In order to clarify if all DTE-local coordinates are involved in the transfer process in the same way, the total energies of the site-local coordinates are analyzed as

shown in Fig.56. For the normal coupling case shown in Fig.56a, it is observable that the local coordinates below 80 cm^{-1} and in resonance (or with the doubled frequency of the DTE transport coordinate) with the DTE-transport coordinate centered around 164 cm^{-1} are strongly involved in the transport dynamics. The scaled total energy of the low frequency coordinate clearly shows a strong decrease within 1.2 ps, whereas the total energy of the coordinate in resonance and $2.0 \cdot \omega_{DTE}$ show a strong increase in total energy. The change in total energy of all other modes is almost zero for the overall simulation time, indicating no or only minor contributions.

In the low coupling case shown in Fig.56b, the contribution of all modes is almost zero. Only the in-resonance coordinates show a small positive amplitude.

This observation leads to the conclusion that on the one hand, only a few local coordinates are really involved in the transfer process and on the other hand, the energy of the local modes is funneled to the DTE transport coordinate.

To study the effect of the intra-molecular coupling parameter κ , this parameter has also been varied systematically by the factor 0.5 and 0.1.

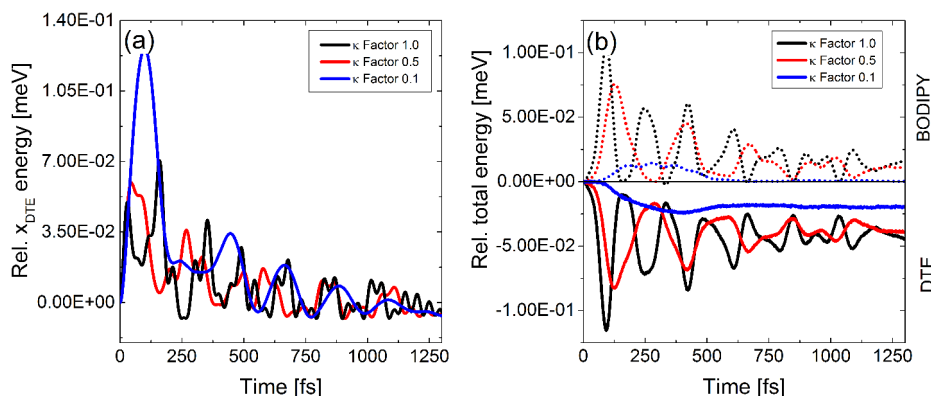


Figure 57: Effect of the fragment-fragment coupling parameter κ on the energy transfer with $\epsilon=15.0 \text{ cm}^{-1}$ and $\gamma=500.0 \text{ fs}^{-1}$. The variable $\kappa=313.0 \text{ cm}^{-1}$ is scaled by a factor of 0.5 or 0.1. A positive signal indicates an increase in energy, whereas a negative signal indicates a decrease in energy. (a) Total energy of the DTE local transport mode and (b) Total energy of DTE and BODIPY fragment. The solid line indicates the total DTE energy, the dotted line the total BODIPY energy. The energies are scaled with respect to the initial energy at $t=0$.

As shown in Fig.57a, the site-site coupling parameter κ has a drastic effect on the scaled total energy of the DTE transport coordinate. As shown for the effect of varying ϵ , a similar oscillatory pattern is observable. Comparing the dynamics for the different κ values, it is observable that the total energy of the DTE transport coordinate increases with decreasing coupling strength. Nevertheless, a fast increase followed by a damping of the total energy is observable on the same time

scale as shown for the DTE local coupling parameter ϵ . The analysis of the total energies of both fragments approve the drastic effect of the variation of the site-site coupling parameter κ . As shown in Fig.57b, the total energy of the BODIPY fragment decreases rapidly with decreasing coupling value. For coupling values between $150\text{-}313\text{ cm}^{-1}$, an efficient energy transfer from the DTE to the BODIPY is observable resulting in a quasi-stationary state as reported before. A noticeable difference can be found in the frequency of the energy transfer but not in the amplitude. In contrast, for a very small coupling value of $\approx 31\text{ cm}^{-1}$, only a small amount of transferred energy to the BODIPY is observable within 300 fs, which decreases to almost zero after $\approx 500\text{ fs}$ due to the coupling to the phenomenological bath. These results show that on the one hand, the coupling parameter κ is essential for an energy transfer from the DTE to the BODIPY fragment but on the other hand, does not influence the absolute value for the transferred energy. Only for very small coupling values, an effect on the absolute value of the total energy is observable, which is related to the coupling to a phenomenological environment. To evaluate the effect of this environment coupled to the BODIPY fragment, this coupling has been changed systematically representing a low, medium and strong coupled environment.

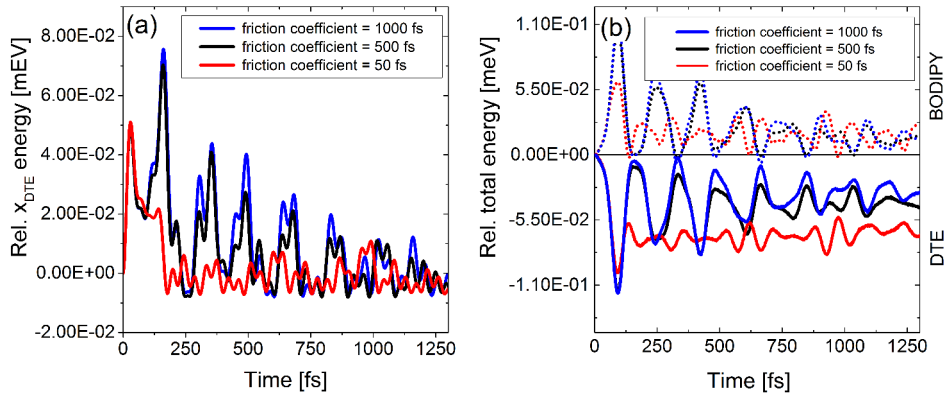


Figure 58: Effect of the dissipative environment coupling parameter γ on the energy transfer with $\epsilon=15.0\text{ cm}^{-1}$ and $\kappa=313.0\text{ cm}^{-1}$. A positive signal indicates an increase in energy, whereas a negative signal indicates a decrease in energy. (a) Total energy of the DTE local transport mode and (b) Total energy of DTE and BODIPY fragment. The solid line indicates the total DTE energy, the dotted line the total BODIPY energy. The energies are scaled with respect to the initial energy at $t=0$.

As shown in Fig.58a for the scaled total energy of the DTE transport coordinate, an indirect coupling of the DTE fragment to the environment is observable. For very high friction coefficients (red) a rapid decrease of the total energy of the DTE transport coordinate is observable after $\approx 200\text{ fs}$. In contrast to this fast

dissipation, the medium and low coupling case show the typical damped oscillatory dynamics as observed before. The efficient energy dissipation induced by the coupled phenomenological environment is also observed in the total energy of the fragments (see Fig.58b). Again, a rapid decrease of the DTE total energy is observable for very high coupling values resulting in a stationary state, whereas the BODIPY total energy increases.

So far, the theoretical results shown for the energy transfer dynamics in a DTE-BODIPY dyad after FC excitation are only based on *ab initio* calculations and transformations of normal modes. To validate if the results of the quantum dynamical simulations, the model and parameters are able to represent the experimentally observed dynamics in an appropriate way, the experimentally observed energy change ΔE is compared to the theoretical results using the originally obtained parameters $\kappa=313 \text{ cm}^{-1}$, $\epsilon=15 \text{ cm}^{-1}$ and $\gamma=750 \text{ fs}^{-1}$.

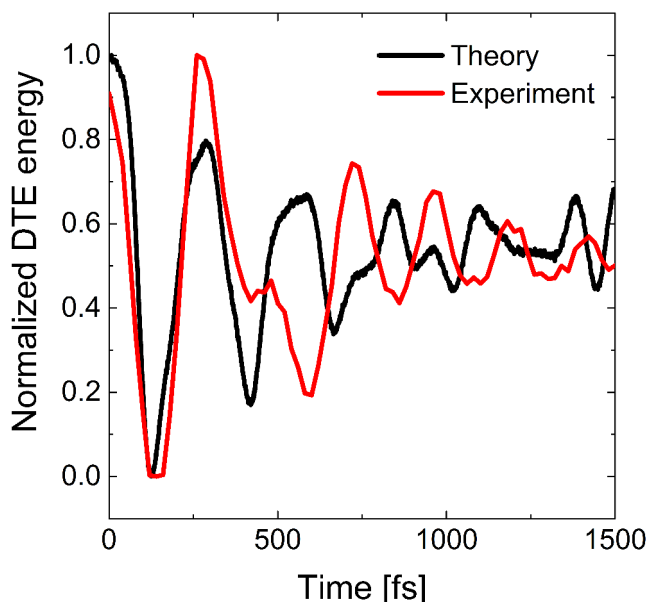


Figure 59: Comparison of the DTE total energy with the theoretically determined parameters to the experimentally observed ΔE (both values are normalized to 1 at $t=0$).

The main discrepancy of theory and experiments is the order of magnitude in the energy change ΔE , and therefore, theoretical and experimental values are normalized with respect to the initial value (the theoretical description underestimates the absolute value of transferred energy by a factor of 10^2 , which is mainly related to our model). As shown in Fig.59, the overall amplitude and frequency of the energy transfer is in good agreement with the experiment, up to a time of $\approx 300 \text{ fs}$. After this time, a shift is observable, but the dynamics are still in good agreement. This shift can be explained by an additional frequency in the experimental sig-

nal. Also the time for the formation of a quasi-stationary state is comparable. These observations lead to the conclusion that the model and parametrization are quite accurate for the description of the energy transfer in the DTE-BODIPY dyad including dissipative coupling effects to a phenomenological environment.

5.5.4 Conclusion

The observations presented in this section show an excellent agreement between experiment and theory. First, a theoretical explanation of experimentally observed oscillations in a time-resolved experiment is derived starting from the geometry of a DTE-BODIPY dyad using *ab initio* methods. These results show that the electronic states of the DTE-BODIPY dyad under study are indeed electronically decoupled and located on the DTE and BODIPY fragment and that the selective excitation of the DTE fragment can induce an energy transfer via a transfer of momentum. This energy transfer via the bridge is related to a normal mode of the system centered around $\approx 147.0 \text{ cm}^{-1}$ which is in very good agreement with the experimentally observed oscillations. Furthermore, a second normal mode, also observed in the experiment, has been found, indicating an energy transfer from DTE to BODIPY via the rigid bridge.

Second, a mapping of the DTE-BODIPY dyad onto a model system including an appropriate parametrization is presented. This model describes the system in terms of coupled harmonic oscillators, which are representing the DTE or BODIPY moiety. Furthermore, a heat bath, representing the hot vibrational state after FC excitation is introduced by a set of DTE local coordinates. Dissipative effects are represented by a harmonic oscillator bath. This model is parametrized using *ab initio* results and calculated spectral densities and is able to reproduce the experimentally observed dynamics and time scales in good agreement.

Finally, the mechanism of the energy transfer is evaluated by systematically changing the parameters of the model Hamiltonian. Intuitively, the energy transfer is expected to show a strong dependency on the coupling between the two coordinates representing the DTE and BODIPY moiety. Interestingly, this coupling parameter does not effect the absolute value of transferred energy in such a strong way as one would expect. However, it has been shown that the coupling to a dissipative environment and the coupling to the DTE local coordinates has a much stronger effect on the absolute value of transferred energy. This is explained by the fact that the local mode energy is funneled into the DTE transport coordinate and dissipate to the environment after transfer to the BODIPY. For a high local coupling, more energy can be redistributed or funneled to the DTE transport coordinate than for

the low coupling case. A similar statement can be formulated for the effect of the dissipative environment: for a high coupling value, a strong energy gradient to the bath is found, resulting in a fast and effective IVR via the BODIPY to the bath. The presented results lead to the conclusion that the observed energy transfer depends on site-local relaxation processes and coupling effects rather than on site-site coupling effects. Nevertheless, the model is approximate and can be improved by including more coupling terms from the site-local modes to the BODIPY fragment.

Concluding Remarks and Outlook

6 | Concluding Remarks and Outlook

The work presented in this thesis helps to clarify the mechanism of excitation energy transfer (EET) after photoexcitation in organic semi-conducting polymers like PPV and PT, or small functional building blocks as exemplified by a DTE-BODIPY dyad. We have focused upon the elementary EET steps on ultrafast time scales, where standard kinetic descriptions are not applicable. Our theoretical approach is based upon electron-hole Hamiltonians of Frenkel or Merrifield type, which are parametrized using high-level electronic structure methods together with adiabatic-to-diabatic mapping procedures. These first-principles parametrized Hamiltonians are subsequently used for high-dimensional quantum dynamical calculations including explicit electronic-vibrational (vibronic) interactions. Similarly, the description of vibrational energy transfer in a DTE-BODIPY system is based upon a first-principles parametrized model for intramolecular vibrational energy redistribution (IVR).

In the context of semi-conducting polymers, small oligomer species were studied – i.e., hexamer or 20-mer species – whose size is sufficient to exhibit the excitonic (band-like) properties that are typical of larger polymer segments. To show this, the electronically excited states which were computed using the high-level ADC(2) method, have been analyzed by a transition density analysis. From excited-state PES cuts along a set of relevant coordinates, including torsional and bond length alternation (BLA) coordinates, diabatic potentials are then generated using a novel adiabatic-to-diabatic mapping scheme. These potentials are used in quantum dynamical calculations by the Multiconfiguration Time-Dependent Hartree (MCTDH) method.

Specifically, an *ab initio* parametrized model Hamiltonian is employed to study ultrafast exciton dynamics across a torsional defect in an oligo-thiophene (OT) fragment. The torsional coordinate planarizes on a time scale of less than one picosecond and guides the exciton dynamics on the lattice. Starting from an initially prepared wave packet on a sub-lattice of the OT oligomer, the exciton dynamics exhibits an EET process on a sub-ps time scale, resulting in a new quasi-stationary state, a so-called *local excitonic ground state* (LEGS), centered in the middle of the overall lattice. The LEGS state can be directly related to the relaxed excited state obtained from our electronic structure (ADC(2)) calculations.

For the smaller hexamer lattice, we observed the spreading of an exciton across a torsional defect, from an initial condition located close to the defect. The larger 20-mer system allowed us to monitor the torsion-induced migration of an exciton which is initially trapped on a sub-lattice. Interestingly, the exciton is found to undergo a “coherent hopping” type dynamics: That is, starting from a LEGS type initial condition localized on a sub-lattice, a rather sudden transition occurs to a LEGS on the overall lattice. The transition is of electronically coherent nature, but the coherent transients subside rapidly, on a scale of ~ 100 fs. Exciton trapping is found to be caused by the high-frequency bond length alternation (BLA) coordinates, and very rapidly acts to create a relaxed, polaronic LEGS state. The “hopping” of the LEGS state is driven by the healing of the torsional defect, and necessitates energy dissipation which is provided by a bath coupled to the torsional mode. These results support the “spectroscopic unit” concept, according to which exciton delocalization is determined by structural defects and conjugation breaks.

The results of the full Merrifield (generalized $e-h$) model are very close to the results of the simplified Frenkel type model, with the drawback that the computational effort is much higher due to the large number of electronic states. Therefore, the full $e-h$ representation is not necessarily needed to describe intra-chain dynamics. This allows the dynamical description of energy transfer on a full quantum level, using a Frenkel model.

For an OPV hexamer and 20-mer system, similar results have been obtained. The model Hamiltonian differs slightly, though, since the torsional and BLA modes are now treated as site-local modes, while these modes were taken to be correlated (i.e., coupled simultaneously to neighboring sites) in the case of OT. Again, an adiabatic-to-diabatic mapping of PES cuts was performed to generate high-dimensional potential surfaces, and MCTDH calculations were performed including BLA and torsional modes.

Based on the potential energy surfaces for OPV, EET dynamics was studied for larger systems including more degrees of freedom and an explicit description of temperature, using the semi-classical Ehrenfest approach including dissipative Langevin dynamics. A FORTRAN 90 program was written specifically for this purpose. In order to validate the semi-classical Ehrenfest method, benchmark calculations are performed for a PPV hexamer system in a Frenkel type basis using the full-quantum MCTDH method. These benchmark calculations show very good agreement with regard to the torsional dynamics and LEGS formation, even though coherent transients on a time scale of several hundred femtoseconds are not

correctly reproduced. We attribute this to the fact that the Ehrenfest approach is not capable of capturing the full electronic-nuclear correlations. Furthermore, it has been shown that a reasonably small number of trajectories are able to describe the dynamics with acceptable accuracy: For a converged Ehrenfest calculation, ≈ 3000 independent trajectories are needed. Dissipation is included either in a Langevin setting, or else using a density-based version of the Ehrenfest dynamics. (The latter, however, does not prove numerically robust.) In the Langevin setting, it turns out that the dynamics depends in a sensitive fashion on whether the fluctuations act in the same way on all trajectory realizations.

The Ehrenfest approach is used to simulate the dynamics of an OPV 20-mer system, including 20 Frenkel states and 80 coordinates. Using this model, the effects of thermal noise and structural disorder are studied by systematically varying the initial conditions of the classical coordinates and the temperature. The results of the systematic variation of these parameters show some drastic effects. On the one hand, no strong effect of the torsional coordinate on the overall exciton dynamics is observed. On the other hand, a strong correlation between the exciton dynamics and temperature is observed. For very low temperatures ($T \leq 10$ K), the formation of a new LEGS on the overall lattice is found whereas for higher temperatures ($T \geq 10$ K) a compact exciton packet can be seen to undergo a hopping type dynamics on the entire lattice. This compact dynamics seems to be correlated to the formation of a minimum energy path created due to the thermal fluctuations of the system coordinates, especially the torsional modes. Increasing the temperature to more than 200 K, the thermal fluctuations of the coordinates are increasingly large, and no minimum energy path is formed. In order to investigate the effect of the different coordinates (i.e., BLA and torsion) a systematic study at 1 K and 100 K has been performed. This study indicates that the high-frequency BLA coordinates are essential for the observed trapping effect at low temperatures while the torsional coordinates are essential for the formation of a minimum energy path.

The results of this project part indicate the capability of a simple mixed quantum-classical method to describe EET on intermediate time scales, beyond the ultrafast regime which necessitates a correct description of quantum coherence. The influence of noise and disorder on the EET process can be captured very well by the Ehrenfest/Langevin approach.

The second type of system that was investigated using high-dimensional quantum dynamical methods is a functional DTE-BODIPY dyad. These investigations were intended to help understand experimental observations and clarify the IVR mechanism in this system. Quite remarkably, ultrafast oscillatory signals associ-

ated with the BODIPY moiety were observed following electronic excitation of the DTE moiety.

Using standard TDDFT methods, several normal modes were identified that are likely associated with the experimentally observed oscillations. In a local-mode picture, an IVR process was proposed explaining the energy transfer between the relevant DTE and BODIPY modes. A model Hamiltonian was set up that includes a subset of transport modes responsible for the energy transfer, along with a “bath” of local modes for each moiety. Using this model, the competition between intra- and intermolecular transfer has been investigated. The outcome of this investigation shows a correlation between an intra-molecular heat-bath created by the photoexcitation and the vibrational energy transfer. Furthermore, the effect of different external environments has been demonstrated, indicating that the external environment has a strong effect on the energy transfer in the system. In general, the projects addressed in this thesis show how a realistic quantum dynamical analysis can be carried out by combining (i) suitable model Hamiltonians, (ii) an *ab initio* based parametrization, and (iii) high-dimensional multiconfigurational quantum dynamics and approximate semi-classical approaches. The strength of this approach is a consistent and transparent treatment of all relevant interactions, and an adequate treatment of ultrafast, coherent transients. Nevertheless, the projects also reveal the limitations of the approach: A full atomistic description is out of reach both from the electronic structure side and from the quantum dynamical perspective (and would require accurate on-the-fly quantum dynamics in many dimensions, which is not yet available). The present approach offers a reasonable compromise, in terms of first-principles parametrized model Hamiltonians that carry over to many dimensions and can be equally used for quantum-dynamical, mixed quantum-classical, and kinetic treatments. Indeed, the present approach is very suitable as a starting point for a multi-scale treatment, and a QM/MM type embedding into a classical environment.

Bibliography

- [1] R. S. Gupta, T. Mukhtar, B. Singh, *Mol. Microbiol.* **1999**, *32*, 893.
- [2] A. W. Rutherford, P. Faller, *Phil. Trans. R. Soc. B* **2003**, *358*, 245.
- [3] D. M. Chapin, C. S. Fuller, G. L. Pearson, *J. Appl. Phys.* **1954**, *25*, 676.
- [4] USA, *US Department of Energy Office of Energy Efficiency and Renewable Energy*, http://www.nrel.gov/ncpv/images/efficiency_chart.jpg, **2015**.
- [5] A. Molki, *Phys. Ed.* **2010**, *45*, 456.
- [6] B. Li, L. Wang, B. Kang, P. Wang, Y. Qiu, *Solar Energy Materials and Solar Cells* **2006**, *90*, 549.
- [7] D. L. Pulfrey, *Photovoltaic Power Generation*, Krieger Pub Co, **1978**.
- [8] F. C. Krebs, M. Hösel, M. Corazza, B. Roth, M. V. Madsen, S. A. Gevorgyan, R. R. Søndergaard, D. Karg, M. Jørgensen, *Energy Technol.* **2013**, *1*, 378.
- [9] A. J. Lennon, R. Y. Utama, M. A. Lenio, A. W. Ho-Baillie, N. B. Kuepper, S. R. Wenham, *Sol. Energ. Mat. Sol. Cells* **2008**, *92*, 1410.
- [10] J. H. Burroughes, D. D. C. Bradley, A. R. Brown, R. N. Marks, K. Mackay, R. H. Friend, P. L. Burns, A. B. Holmes, *Nature* **1990**, *347*, 539.
- [11] L. Dworak, A. J. Reuss, M. Zastrow, K. Rück-Braun, J. Wachtveitl, *Nanoscale* **2014**, *6*, 14200.
- [12] V. May, O. Kühn, *Charge and Energy Transfer Dynamics in Molecular Systems*, Wiley-VCH, **2011**.
- [13] E. Collini, G. D. Scholes, *Science* **2009**, *323*, 369.
- [14] H. Meyer, U. Manthe, L. Cederbaum, *Chem. Phys. Lett.* **1990**, *165*, 73.
- [15] O. Vendrell, H.-D. Meyer, *J. Chem. Phys.* **2011**, *134*, 044135.
- [16] H. Zhou, Q. Chen, G. Li, S. Luo, T.-B. Song, H.-S. Duan, Z. Hong, J. You, Y. Liu, Y. Yang, *Science* **2014**, *345*, 542.
- [17] S. Collavini, S. F. Völker, J. L. Delgado, *Angew. Chem. Int. Ed.* **2015**, *54*, 9757.
- [18] E. N. Hooley, A. J. Tilley, J. M. White, K. P. Ghiggino, T. D. M. Bell, *Phys. Chem. Chem. Phys.* **2014**, *16*, 7108.
- [19] K. M. Gaab, C. J. Bardeen, *J. Phys. Chem. B* **2004**, *108*, 4619.

- [20] F. S. F. Morgenstern, A. Rao, M. L. Böhm, R. J. P. Kist, Y. Vaynzof, N. C. Greenham, *ACS Nano* **2014**, *8*, 1647.
- [21] C. Consani, F. Koch, F. Panzer, T. Unger, A. Köhler, T. Brixner, *J. Chem. Phys.* **2015**, *142*, 212429.
- [22] I. Burghardt, E. R. Bittner, H. Tamura, A. Pereverzev, J. G. S. Ramon in *Energy Transfer Dynamics in Biomaterial Systems, Vol. 93*, (Eds.: I. Burghardt, V. May, D. A. Micha, E. R. Bittner), **2009**, pp. 183–212.
- [23] F. Sterpone, R. Martinazzo, A. N. Panda, I. Burghardt, *Z. Phys. Chem.* **2011**, *225*, 541.
- [24] K. Sen, R. Crespo-Otero, O. Weingart, W. Thiel, M. Barbatti, *J. Chem. Theory Comput.* **2013**, *9*, 533.
- [25] S.-J. Xiong, Y. Xiong, Y. Zhao, *J. Chem. Phys.* **2012**, *137*, 094107.
- [26] T. Adachi, G. Lakhwani, M. C. Traub, R. J. Ono, C. W. Bielawski, P. F. Barbara, D. A. V. Bout, *J. Phys. Chem. B* **2012**, *116*, 9866.
- [27] A. Köhler, S. T. Hoffmann, H. Bässler, *J. Am. Chem. Soc.* **2012**, 11594.
- [28] M. M. L. Grage, P. W. Wood, A. Ruseckas, T. Pullerits, W. Mitchell, P. L. Burn, I. D. W. Samuel, V. Sundstrom, *J. Chem. Phys.* **2003**, *118*, 7644.
- [29] A. N. Panda, F. Plasser, A. J. A. Aquino, I. Burghardt, H. Lischka, *J. Phys. Chem. A* **2013**, *117*, 2181.
- [30] M. H. Lee, J. Aragó, A. Troisi, *J. Phys. Chem. C* **2015**, *119*, 14989.
- [31] M. Scheidler, U. Lemmer, R. Kersting, S. Karg, W. Riess, B. Cleve, R. F. Mahrt, H. Kurz, H. Bässler, E. O. Göbel, P. Thomas, *Phys. Rev. B* **1996**, *54*, 5536.
- [32] J. Wahl, R. Binder, I. Burghardt, *Comp. Theo. Chem.* **2014**, *1040–1041*, 167.
- [33] M. Hultell, S. Stafstrøm, *Phys. Rev. B* **2009**, *79*, 014302.
- [34] M. Linares, M. Hultell, S. Stafstrøm, *Synthetic Metals*, International Conference on Science and Technology of Synthetic Metals, Porto de Galinhas Pernambuco, Brazil, July 6-11, 2008 ICSM 2008 **2009**, *159*, 2219.
- [35] L. A. R. Junior, W. F. da Cunha, G. M. e Silva, *J. Phys. Chem. A* **2014**, *118*, 6272.

- [36] A. Kushnarenko, V. Krylov, E. Miloglyadov, M. Quack, G. Seyfang, English in *Ultrafast Phenomena XVI*, (Eds.: P. Corkum, S. Silvestri, K. A. Nelson, E. Riedle, R. W. Schoenlein), Springer Series in Chemical Physics, Springer Berlin Heidelberg, **2009**, pp. 349–351.
- [37] M. Schade, A. Moretto, M. Crisma, C. Toniolo, P. Hamm, *J. Phys. Chem. B* **2009**, *113*, 13393.
- [38] P. Hamm, M. Schade, E. H. Backus, A. Moretto, C. Toniolo in International Conference on Ultrafast Phenomena, Optical Society of America, **2010**, ThD2.
- [39] M. Schade, P. Hamm, *J. Chem. Phys* **2012**, *393*, 46.
- [40] M. Schade, P. Hamm, *J. Chem. Phys.* **2009**, *131*, 044511.
- [41] M. Schulze, M. Utecht, A. Hebert, K. Rück-Braun, P. Saalfrank, P. Tegeder, *J. Phys. Chem. Lett.* **2015**, *6*, 505.
- [42] F. Schweighöfer, L. Dworak, M. Braun, M. Zastrow, J. Wahl, I. Burghardt, K. Rück-Braun, J. Wachtveitl, *Sci. Rep.* **2015**, *5*, 9368.
- [43] W. J. D. Beenken, *Phys. Status Solidi A* **2009**, *206*, 2750.
- [44] H. Gest, *Photosynth. Res.* **2002**, *73*, 7.
- [45] G. D. Scholes, *ACS Nano* **2008**, *2*, 523.
- [46] J. Frenkel, *Phys. Rev.* **1931**, *37*, 17.
- [47] G. H. Wannier, *Phys. Rev.* **1937**, *52*, 191.
- [48] J. D. Wright, *Molecular Crystals*, Cambridge University Press, **1995**.
- [49] McGraw-Hill, *McGraw Hill Encyclopedia of Science & Technology (McGraw-Hill Encyclopedia of Science & Technology (20v.))* McGraw-Hill Professional, **2007**.
- [50] T. Brixner, J. Stenger, H. M. Vaswani, M. Cho, R. E. Blankenship, G. R. Fleming, *Nature* **2005**, *434*, 625.
- [51] E. Romero, R. Augulis, V. I. Novoderezhkin, M. Ferretti, J. Thieme, D. Zigmantas, R. van Grondelle, *Nat. Phys.* **2014**, *10*, 676.
- [52] H. Lee, Y.-C. Cheng, G. R. Fleming, *Science* **2007**, *316*, 1462.
- [53] C. Olbrich, T. L. C. Jansen, J. Liebers, M. Aghtar, J. Strümpfer, K. Schulten, J. Knoester, U. Kleinekathöfer, *J. Phys. Chem. B* **2011**, *115*, 8609.
- [54] C. Olbrich, J. Strümpfer, K. Schulten, U. Kleinekathöfer, *J. Phys. Chem. Lett.* **2011**, *2*, 1771.

- [55] C. G. Gillis, G. A. Jones, *J. Phys. Chem. B* **2015**, *119*, 4165.
- [56] K. A. Mazzio, C. K. Luscombe, *Chem. Soc. Rev.* **2015**, *44*, 78.
- [57] W. Cao, J. Xue, *Energy Environ. Sci.* **2014**, *7*, 2123.
- [58] P. N. Rivers, *Leading Edge Research in Solar Energy*, Nova Science Pub Inc, **2007**.
- [59] H. Hertz, *Ann. Phys. Chem.* **1887**, *267*, 983.
- [60] F. Yang, M. Shtein, S. R. Forrest, *Nat. Mater* **2005**, *4*, 37.
- [61] T. Förster, *Ann. Phys.* **1948**, *2*, 55.
- [62] D. L. Dexter, *J. Chem. Phys.* **1953**, *21*, 836.
- [63] *Chemistry 1991-1995 (Nobel Lectures)*, World Scientific Pub Co Inc, **1997**.
- [64] R. A. Marcus, *J. Chem. Phys.* **1956**, *24*, 966.
- [65] S. L. Smith, A. W. Chin, *Phys. Chem. Chem. Phys.* **2014**, *16*, 20305.
- [66] K. M. Kaunisto, P. Vivo, R. K. Dubey, V. I. Chukharev, A. Efimov, N. V. Tkachenko, H. J. Lemmetyinen, *J. Phys. Chem. C* **2014**, *118*, 10625.
- [67] *Handbook of Photovoltaic Science and Engineering*, (Eds.: A. Luque, S. Hegedus), Wiley-Blackwell, **2010**.
- [68] J. Nelson, *The Physics of Solar Cells (Properties of Semiconductor Materials)*, Imperial College Press, **2003**.
- [69] D. Wøhrle, D. Meissner, *Adv. Mater.* **1991**, *3*, 129.
- [70] W. Barford, *Electronic and Optical Properties of Conjugated Polymers*, Oxford University Press, **2013**, 321 pp.
- [71] E. N. Hooley, A. J. Tilley, J. M. White, K. Ghiggino, T. D. M. Bell, *Phys. Chem. Chem. Phys.* **2014**.
- [72] M. R. Raj, S. Anandan, R. V. Solomon, P. Venuvanalingam, S. S. K. Iyer, M. Ashokkumar, *J. Photochem. Photobiol. A* **2013**, *262*, 34.
- [73] H. N. Serap Günes, *Chem. Rev.* **2007**, *107*, 1324.
- [74] C. A. M. Borges, A. Marletta, R. M. Faria, F. E. G. Guimarães, *Braz. J. Phys.* **2004**, *34*, 590.
- [75] W. Barford, O. R. Tozer, *J. Chem. Phys.* **2014**, *141*, 164103.
- [76] M. Sim, J. Shin, C. Shim, M. Kim, S. B. Jo, J.-H. Kim, K. Cho, *J. Phys. Chem. C* **2013**.

- [77] R. Fitzner, E. Mena-Osteritz, A. Mishra, G. Schulz, E. Reinold, M. Weil, C. Körner, H. Ziehlke, C. Elschner, K. Leo, M. Riede, M. Pfeiffer, C. Urich, P. Bäuerle, *J. Am. Chem. Soc.* **2012**, *134*, 11064.
- [78] Z. Sun, S. Stafstrøm, *J. Chem. Phys.* **2013**, *138*, 164905.
- [79] A. Pivrikas, N. S. Sariciftci, G. Juška, R. Österbacka, *Prog. Photovolt: Res. Appl.* **2007**, *15*, 677.
- [80] H. Hoppe, N. S. Sariciftci, *J. Mater. Res.* **2004**, *19*, 1924.
- [81] I.-W. Hwang, C. Soci, D. Moses, Z. Zhu, D. Waller, R. Gaudiana, C. J. Brabec, A. J. Heeger, *Adv. Mater.* **2007**, *19*, 2307.
- [82] Z. E. Lampert, C. L. Reynolds, J. M. Papanikolas, M. O. Aboelfotoh, *J. Phys. Chem. B* **2012**, *116*, 12835.
- [83] R. Chang, J. H. Hsu, W. S. Fann, K. K. Liang, C. H. Chiang, M. Hayashi, J. Yu, S. H. Lin, E. C. Chang, K. R. Chuang, S. A. Chen, *Chem. Phys. Lett.* **2000**, *317*, 142.
- [84] W. P. Su, J. R. Schrieffer, A. J. Heeger, *Phys. Rev. Lett.* **1979**, *42*, 1698.
- [85] J. Bakalis, A. R. Cook, S. Asaoka, M. Forster, U. Scherf, J. R. Miller, *J. Phys. Chem. C* **2014**, *118*, 114.
- [86] S. Yamamoto, H. Ohkita, H. Benten, S. Ito, *J. Phys. Chem. C* **2012**, *116*, 14804.
- [87] M. Planells, A. Abate, H. J. Snaith, N. Robertson, *ACS Appl. Mater. Interfaces* **2014**, *6*, 17226.
- [88] M. Hultell, S. Stafstrøm, *Chem. Phys. Lett.* **2006**, *428*, 446.
- [89] S. Stafstrøm, R. Riklund, K. A. Chao, *Phys. Rev. B* **1983**, *27*, 6158.
- [90] D. P. McMahon, A. Troisi, *Chem. Phys. Chem.* **2010**, *11*, 2067.
- [91] W. Barford, D. Trembath, *Phys. Rev. B* **2009**, *80*, 165418.
- [92] Y.-A. Yan, S. Cai, *J. Chem. Phys.* **2014**, *141*, 054105.
- [93] K. F. Wong, M. S. Skaf, C. Y. Yang, P. J. Rossky, B. Bagchi, D. H. Hu, J. Yu, P. F. Barbara, *J. Phys. Chem. B* **2001**, *105*, 6103.
- [94] S. Saini, B. Bagchi, *Phys. Chem. Chem. Phys.* **2010**, *12*, 7427.
- [95] N. Takeda, J. R. Miller, *J. Phys. Chem. B* **2012**, *116*, 14715.
- [96] W. Barford, E. R. Bittner, A. Ward, *J. Phys. Chem. A* **2012**, *116*, 10319.
- [97] T. Holstein, *Ann. Phys.* **1959**, *8*, 343.

- [98] R. E. Merrifield, *J. Chem. Phys.* **1963**, *38*, 920.
- [99] R. E. Merrifield, *J. Chem. Phys.* **1961**, *34*, 1835.
- [100] W. P. Su, J. R. Schrieffer, A. J. Heeger, *Phys. Rev. B* **1980**, *22*, 2099.
- [101] A. Kawamori, J. Yamauchi, H. Ohta, *EPR in the 21st Century*, Elsevier Science, **2002**.
- [102] A. Szabo, N. S. Ostlund, *Modern Quantum Chemistry: Introduction to Advanced Electronic Structure Theory (Dover Books on Chemistry)*, Dover Publications, **1996**.
- [103] C. J. Cramer, *Essentials of Computational Chemistry: Theories and Models*, Wiley, **2004**.
- [104] R. M. Dreizler, E. K. Gross, *Density Functional Theory: An Approach to the Quantum Many-Body Problem*, Springer, **1996**.
- [105] M. Wormit, PhD thesis, Goethe University Frankfurt, **2009**.
- [106] O. Christiansen, H. Koch, P. Jørgensen, *Chem. Phys. Lett.* **1995**, *243*, 409.
- [107] A. B. Trofimov, J. Schirmer, *J. Phys. B* **1995**, *28*, 2299.
- [108] F. Jensen, *Introduction to Computational Chemistry*, Wiley, **2007**.
- [109] M. H. Beck, A. Jäckle, G. A. Worth, H. D. Meyer, *Phys. Rep.* **2000**, *324*, 1.
- [110] H.-D. Mayer, F. Gatti, G. A. Worth, *Multidimensional Quantum Dynamics*, Wiley-VCH, **2009**.
- [111] P. Ehrenfest, *Z. Physik* **1927**, *45*, 455.
- [112] J. L. Alonso, J. Clemente-Gallardo, J. C. Cuchí, P. Echenique, F. Falceto, *J. Chem. Phys.* **2012**, *137*, 054106.
- [113] M. Born, R. Oppenheimer, *Ann. Phys.* **1927**, *389*, 457.
- [114] P. Hohenberg, W. Kohn, *Phys. Rev.* **1964**, *136*, B864.
- [115] W. Kohn, L. J. Sham, *Phys. Rev.* **1965**, *140*, A1133.
- [116] R. G. Parr, Y. Weitao, *Density-Functional Theory of Atoms and Molecules (International Series of Monographs on Chemistry)*, Oxford University Press, **1994**.
- [117] J. P. Perdew, J. A. Chevary, S. H. Vosko, K. A. Jackson, M. R. Pederson, D. J. Singh, C. Fiolhais, *Phys. Rev. B* **1992**, *46*, 6671.

-
- [118] P. J. Stephens, F. J. Devlin, C. F. Chabalowski, M. J. Frisch, *J. Phys. Chem.* **1994**, *98*, 11623.
- [119] E. Runge, E. K. U. Gross, *Phys. Rev. Lett.* **1984**, *52*, 997.
- [120] C. Hättig, F. Weigend, *J. Chem. Phys.* **2000**, *113*, 5154.
- [121] C. Møller, M. S. Plesset, *Phys. Rev.* **1934**, *46*, 618.
- [122] G. A. Worth, L. S. Cederbaum, *Annu. Rev. Phys. Chem.* **2004**, *55*, 127.
- [123] G. A. Worth, M. H. Beck, A. Jäckle, H.-D. Meyer, The MCTDH Package, Version 8.2, (2000). H.-D. Meyer, Version 8.3 (2002), Version 8.4 (2007). Current version: 8.5.4 (2015). See <http://mctdh.uni-hd.de>, University of Heidelberg, Germany.
- [124] D. J. Tannor, *Introduction to Quantum Mechanics: A Time-Dependent Perspective*, University Science Books, **2006**.
- [125] T. C. Berkelbach, T. E. Markland, D. R. Reichman, *J. Chem. Phys.* **2012**, *136*, 084104.
- [126] T. C. Berkelbach, D. R. Reichman, T. E. Markland, *J. Chem. Phys.* **2012**, *136*, 034113.
- [127] R. Zwanzig, *J. Stat. Phys.* **1973**, *9*, 215.
- [128] D. V. Shalashilin, *J. Chem. Phys.* **2010**, *132*, 244111.
- [129] D. V. Shalashilin, *J. Chem. Phys.* **2009**, *130*, 244101.
- [130] S. Römer, I. Burghardt, *Mol. Phys.* **2013**, *111*, 3618.
- [131] T. Ma, R. Hegger, I. Burghardt, *in preparation* **2016**.
- [132] D. V. Shalashilin, I. Burghardt, *J. Chem. Phys.* **2008**, *129*, 084104.
- [133] I. Burghardt, L. S. Cederbaum, *J. Chem. Phys.* **2001**, *115*, 10303.
- [134] G. E. P. Box, M. E. Muller, *Ann. Math. Statist.* **1958**, *29*, 610.
- [135] T. A. B. G. Marsaglia, *SIAM Review* **1964**, *6*, 260.
- [136] P. E. Kloeden, E. Platen, *Numerical Solution of Stochastic Differential Equations*, Springer Science, **1992**.
- [137] J. C. Butcher, *Numerical Methods for Ordinary Differential Equations*, Wiley, **2003**.
- [138] W. H. Press, B. P. Flannery, S. A. Teukolsky, W. T. Vetterling, *Numerical Recipes in Fortran 77: The Art of Scientific Computing*, Cambridge University Press, **1992**.

- [139] E. Hairer, G. Wanner, *Solving Ordinary Differential Equations II: Stiff and Differential-Algebraic Problems (Springer Series in Computational Mathematics) (v. 2)*, Springer, **2004**.
- [140] U. Mutze, *arXiv:1311.6602 [math]* **2013**.
- [141] R. Binder, S. Römer, J. Wahl, I. Burghardt, *J. Chem. Phys.* **2014**, *141*, 014101.
- [142] V. Martina, K. Ionescu, L. Pigani, F. Terzi, A. Ulrici, C. Zanardi, R. Seeber, *Anal. Bioanal. Chem.* **2007**, *387*, 2101.
- [143] K. Müllen, G. Wegner, *Electronic Materials: The Oligomer Approach*, Wiley-VCH, **1998**.
- [144] I. F. Perepichka, D. F. Perepichka, H. Meng, F. Wudl, *Adv. Mater.* **2005**, *17*, 2281.
- [145] D. Fichou, *Handbook of Oligo- and Polythiophenes*, Wiley-VCH, **1999**.
- [146] Y. Kim, S. Cook, S. M. Tuladhar, S. A. Choulis, J. Nelson, J. R. Durrant, D. D. C. Bradley, M. Giles, I. McCulloch, C.-S. Ha, M. Ree, *Nat. Mater.* **2006**, *5*, 197.
- [147] W. J. E. Beek, M. M. Wienk, R. A. J. Janssen, *Adv. Funct. Mater.* **2006**, *16*, 1112.
- [148] D. Beljonne, Z. Shuai, J. L. Bredas, *J. Chem. Phys.* **1993**, *98*, 8819.
- [149] E. A. Lukina, M. N. Uvarov, L. V. Kulik, *J. Phys. Chem. C* **2014**, *118*, 18307.
- [150] F. E. Osterloh, M. A. Holmes, J. Zhao, L. Chang, S. Kawula, J. D. Roehling, A. J. Moulé, *J. Phys. Chem. C* **2014**, *118*, 14723.
- [151] W. Barford, *J. Phys. Chem. A* **2013**, *117*, 2665.
- [152] W. Barford, D. G. Lidzey, D. V. Makhov, A. J. H. Meijer, *J. Chem. Phys.* **2010**, *133*, 044504.
- [153] S. Stafstrøm, *Chem. Soc. Rev.* **2010**, *39*, 2484.
- [154] P. Shushkov, R. Li, J. C. Tully, *J. Chem. Phys.* **2012**, *137*, 22A549.
- [155] H. Yamagata, F. C. Spano, *J. Chem. Phys.* **2012**, *136*, 184901.
- [156] D. Beljonne, G. Pourtois, C. Silva, E. Hennebicq, L. M. Herz, R. H. Friend, G. D. Scholes, S. Setayesh, K. Mullen, J. L. Bredas, *Proc. Natl. Acad. Sci. USA* **2002**, *99*, 10982.
- [157] E. Benassi, S. Corni, *J. Phys. Chem. C* **2013**, *117*, 25026.

- [158] E. E. Jelley, *Nature* **1936**, *138*, 1009.
- [159] H. Yamagata, N. J. Hestand, F. C. Spano, A. Köhler, C. Scharsich, S. T. Hoffmann, H. Baessler, *J. Chem. Phys.* **2013**, *139*, 114903.
- [160] J. Clark, T. Nelson, S. Tretiak, G. Cirmi, G. Lanzani, *Nat. Phys.* **2012**, *8*, 225.
- [161] M. Hultell, S. Stafström, *Phys. Rev. B* **2007**, *75*, 104304.
- [162] V. Lukes, A. J. Aguiar Aquino, H. Lischka, H.-F. Kauffmann, *J. Phys. Chem. B* **2007**, *111*, 7954.
- [163] G. Horowitz, B. Bachet, A. Yassar, P. Lang, F. Demanze, J.-L. Fave, F. Garnier, *Chem. Mater.* **1995**, *7*, 1337.
- [164] A. C. Alguno, W. C. Chung, R. V. Bantaculo, R. M. Vequizo, H. Miyata, E. W. Ignacio, A. M. Bacala, *NECTEC Tec. J.* **2010**, *2*, 215.
- [165] T.-C. Chung, J. H. Kaufman, A. J. Heeger, F. Wüdl, *Phys. Rev. B* **1984**, *30*, 702.
- [166] R. Binder, J. Wahl, S. Roemer, I. Burghardt, *Farad. Discuss.* **2013**, *163*, 205.
- [167] S. Karabunarliev, E. R. Bittner, *J. Chem. Phys.* **2003**, *118*, 4291.
- [168] R. Ahlrichs, M. Bär, M. Häser, H. Horn, C. Kölmel, *Chem. Phys. Lett.* **1989**, *162*, 165.
- [169] TURBOMOLE V6.4 2012, a development of University of Karlsruhe and Forschungszentrum Karlsruhe GmbH, 1989-2007, TURBOMOLE GmbH, since 2007; available from <http://www.turbomole.com>.
- [170] C. Hättig, G. Schmitz, J. Kößmann, *Phys. Chem. Chem. Phys.* **2012**, *14*, 6549.
- [171] F. Weigend, R. Ahlrichs, *Phys. Chem. Chem. Phys.* **2005**, *7*, 3297.
- [172] K. Eichkorn, F. Weigend, O. Treutler, R. Ahlrichs, *Theor. Chem. Acta.* **1997**, *97*, 119.
- [173] F. Weigend, M. Häser, H. Patzelt, R. Ahlrichs, *Chem. Phys. Lett.* **1998**, *294*, 143.
- [174] A. Dreuw, M. Head-Gordon, *J. Am. Chem. Soc.* **2004**, *126*, 4007.
- [175] G. Horowitz, B. Bachet, A. Yassar, P. Lang, F. Demanze, J.-L. Fave, F. Garnier, *Chem. Mat.* **1995**, *7*, 1337.

- [176] V. Hernandez et al., *J. Chem. Phys.* **1994**, *101*, 1369.
- [177] A. Almenningen et al., *Acta. Chem. Scand.* **1958**, *12*, 1671.
- [178] K. H. Park, P. Kim, W. Kim, H. Shimizu, M. Han, E. Sim, M. Iyoda, D. Kim, *Angew. Chem. Int. Ed.* **2015**, *54*, 12711.
- [179] F. Plasser, H. Lischka, *J. Chem. Theory Comput.* **2012**, *8*, 2777.
- [180] M. Al-Anber, B. Milde, W. Alhalasah, H. Lang, R. Holze, *Electrochim. Acta* **2008**, *53*, 6038.
- [181] P. Garcia, J. M. Pernaut, P. Hapiot, V. Wintgens, P. Valat, F. Garnier, D. Delabouglise, *J. Phys. Chem.* **1993**, *97*, 513.
- [182] A. Yassar, G. Horowitz, P. Valat, V. Wintgens, M. Hmyene, F. Deloffre, P. Srivastava, P. Lang, F. Garnier, *J. Phys. Chem.* **1995**, *99*, 9155.
- [183] F. Plasser, R. Crespo-Otero, M. Pederzoli, J. Pittner, H. Lischka, M. Barbatti, *J. Chem. Theory Comput.* **2014**, *10*, 1395.
- [184] N. O. C. Winter, N. K. Graf, S. Leutwyler, C. Hättig, *Phys. Chem. Chem. Phys.* **2013**, *15*, 6623.
- [185] O. R. Tozer, W. Barford, *J. Phys. Chem. A* **2012**, *116*, 10310.
- [186] T. J. Magnanelli, A. E. Bragg, *J. Phys. Chem. Lett.* **2015**, *6*, 438.
- [187] I. Hwang, G. D. Scholes, *Chem. Mat.* **2011**, *23*, 610.
- [188] D. V. Makhov, W. Barford, *Phys. Rev. B* **2010**, *81*, 165201.
- [189] S. Tretiak, A. Saxena, R. L. Martin, A. R. Bishop, *Phys. Rev. Lett.* **2002**, *89*, 097402.
- [190] M. O. Reese, A. J. Morfa, M. S. White, N. Kopidakis, S. E. Shaheen, G. Rumbles, D. S. Ginley, *Sol. Energ. Mat. Sol. Cells* **2008**, *92*, 746.
- [191] M. Jørgensen, K. Norrman, S. A. Gevorgyan, T. Tromholt, B. Andreasen, F. C. Krebs, *Adv. Mater.* **2011**, *24*, 580.
- [192] K. Norrman, F. C. Krebs, *Sol. Energ. Mat. Sol. Cells* **2006**, *90*, 213.
- [193] *Organic Photovoltaics*, (Eds.: C. Brabec, U. Scherf, V. Dyakonov), Wiley-Blackwell, **2014**.
- [194] T. E. Dykstra, E. Hennebicq, D. Beljonne, J. Gierschner, G. Claudio, E. R. Bittner, J. Knoester, G. D. Scholes, *J. Phys. Chem. B* **2009**, *113*, 656.
- [195] E. Collini, G. D. Scholes, *J. Phys. Chem. A* **2009**, *113*, 4223.
- [196] W. Xie, S. Bai, L. Zhu, Q. Shi, *J. Phys. Chem. A* **2013**, *117*, 6196.

- [197] G. Li, B. Movaghar, A. Nitzan, M. A. Ratner, *J. Chem. Phys.* **2013**, *138*, 044112.
- [198] A. Mishchenko, D. Vonlanthen, V. Meded, M. Bürkle, C. Li, I. V. Pobelov, A. Bagrets, J. K. Viljas, F. Pauly, F. Evers, M. Mayor, T. Wandlowski, *Nano Lett.* **2010**, *10*, 156.
- [199] *Charge and Exciton Transport through Molecular Wires*, (Eds.: L. D. A. Siebbeles, F. C. Grozema), Wiley-Blackwell, **2011**.
- [200] A. Schäfer, H. Horn, R. Ahlrichs, *J. Chem. Phys.* **1992**, *97*, 2571.
- [201] W. J. D. Beenken, T. Pullerits, *J. Chem. Phys. B* **2004**, *108*, 6164.
- [202] M. M.-L. Grage, Y. Zaushitsyn, A. Yartsev, M. Chachisvilis, V. Sundström, T. Pullerits, *Phys. Rev. B* **2003**, *67*, 205207.
- [203] M. M.-L. Grage, P. W. Wood, A. Ruseckas, T. Pullerits, W. Mitchell, P. L. Burn, I. D. W. Samuel, V. Sundström, *J. Chem. Phys.* **2003**, *118*, 7644.
- [204] J. C. Tully, *J. Chem. Phys.* **2012**, *137*, 22A301.
- [205] V. N. Gorshkov, S. Tretiak, D. Mozyrsky, *Nat. Commun.* **2013**, *4*.
- [206] K. Saita, M. G. D. Nix, D. V. Shalashilin, *Phys. Chem. Chem. Phys.* **2013**, *15*, 16227.
- [207] M.-M. Russew, S. Hecht, *Adv. Mater.* **2010**, *22*, 3348.
- [208] J. Wirth, N. Hatter, R. Drost, T. R. Umbach, S. Barja, M. Zastrow, K. Rück-Braun, J. I. Pascual, P. Saalfrank, K. J. Franke, *J. Phys. Chem. C* **2015**, *119*, 4874.
- [209] S. Kühn, S. Friede, M. Zastrow, C. Gahl, K. Rück-Braun, T. Elsässer, *Chem. Phys. Lett.* **2012**, *542*, 94.
- [210] A. Loudet, K. Burgess, *Chem. Rev.* **2007**, *107*, 4891.
- [211] J. C. Slater, *Phys. Rev.* **1951**, *81*, 385.
- [212] A. D. Becke, *J. Chem. Phys.* **1993**, *98*, 1372.
- [213] A. D. Becke, *Phys. Rev. A* **1988**, *38*, 3098.
- [214] C. T. Lee, W. T. Yang, R. G. Parr, *Phys. Rev. B* **1988**, *37*, 785.
- [215] P. A. M. Dirac, *Proc. R. Soc. A* **1929**, *123*, 714.
- [216] J. S. Binkley, J. A. Pople, W. J. Hehre, *J. Am. Chem. Soc.* **1980**, *102*, 939.
- [217] M. S. Gordon, J. S. Binkley, J. A. Pople, W. J. Pietro, W. J. Hehre, *J. Am. Chem. Soc.* **1982**, *104*, 2797.

- [218] *Density-Functional Methods for Excited States*, (Eds.: N. Ferré, M. Filatov, M. Huix-Rotllant), Springer International Publishing, **2016**.
- [219] A. P. Scott, L. Radom, *J. Phys. Chem.* **1996**, *100*, 16502.
- [220] C. Slavov, N. Bellakbil, J. Wahl, K. Mayer, K. Rück-Braun, I. Burghardt, J. Wachtveitl, M. Braun, *Phys. Chem. Chem. Phys.* **2015**, *17*, 14045.
- [221] M. J. Frisch, G. W. Trucks, H. B. Schlegel, G. E. Scuseria, M. A. Robb, J. R. Cheeseman, G. Scalmani, V. Barone, B. Mennucci, G. A. Petersson, H. Nakatsuji, M. Caricato, X. Li, H. P. Hratchian, A. F. Izmaylov, J. Bloino, G. Zheng, J. L. Sonnenberg, M. Hada, M. Ehara, K. Toyota, R. Fukuda, J. Hasegawa, M. Ishida, T. Nakajima, Y. Honda, O. Kitao, H. Nakai, T. Vreven, J. A. Montgomery, Jr., J. E. Peralta, F. Ogliaro, M. Bearpark, J. J. Heyd, E. Brothers, K. N. Kudin, V. N. Staroverov, R. Kobayashi, J. Normand, K. Raghavachari, A. Rendell, J. C. Burant, S. S. Iyengar, J. Tomasi, M. Cossi, N. Rega, J. M. Millam, M. Klene, J. E. Knox, J. B. Cross, V. Bakken, C. Adamo, J. Jaramillo, R. Gomperts, R. E. Stratmann, O. Yazyev, A. J. Austin, R. Cammi, C. Pomelli, J. W. Ochterski, R. L. Martin, K. Morokuma, V. G. Zakrzewski, G. A. Voth, P. Salvador, J. J. Dannenberg, S. Dapprich, A. D. Daniels, Ö. Farkas, J. B. Foresman, J. V. Ortiz, J. Cioslowski, D. J. Fox, Gaussian 09 Revision E.01.
- [222] C. R. Jacob, S. Lubner, M. Reiher, *J. Phys. Chem. B* **2009**, *113*, 6558.
- [223] T. Weymuth, C. R. Jacob, M. Reiher, *J. Phys. Chem. B* **2010**, *114*, 10649.
- [224] V. Liégeois, C. R. Jacob, B. Champagne, M. Reiher, *J. Phys. Chem. A* **2010**, *114*, 7198.
- [225] T. Siebert, B. Guchhait, Y. Liu, R. Costard, T. Elsässer, *J. Phys. Chem. B* **2015**, *119*, 9670.

Scientific contributions

Publications

1. H. Tamura, K. H. Hughes, R. Martinazzo, J. Wahl, R. Binder, and I. Burghardt, "*Ultrafast energy and charge transfer in functional molecular nanoscale aggregates*", in *Ultrafast Dynamics at the nanoscale: Biomolecules and Supramolecular Assemblies*, Eds. S. Haacke and I. Burghardt, Pan Stanford Publishers, **2016**
2. C. Slavov, N. Bellakbil, J. Wahl, K. Mayer, K. Rück-Braun, I. Burghardt, J. Wachtveitl, M. Braun, "*Ultrafast coherent dynamics reveals a reactive mode in the ring-opening reaction of fulgides*", *Phys. Chem. Chem. Phys.*, **2015**, 17, 14045
3. F. Schweighöfer, L. Dworak, M. Braun, M. Zastrow, J. Wahl, I. Burghardt, K. Rück-Braun, J. Wachtveitl, "*Vibrational coherence transfer in an electronically decoupled molecular dyad*", *Sci. Rep.*, **2015**, 5, 9368
4. J. Wahl, R. Binder, I. Burghardt, "*Quantum dynamics of ultrafast exciton relaxation on a minimal lattice*", *Comp. Theo. Chem.*, **2014**, 1040, 167
5. R. Binder, S. Römer, J. Wahl, I. Burghardt, "*An analytic mapping of oligomer potential energy surfaces to an effective Frenkel model*", *J. Chem. Phys.*, **2014**, 141, 014101
6. R. Binder, J. Wahl, S. Römer, I. Burghardt, "*Coherent exciton transport driven by torsional dynamics: a quantum dynamical study of phenylene-vinylene type conjugated systems*", *Faraday Disc.*, **2013**, 163, 205

Oral contributions to conferences

1. "*Vibrationally coherent transfer in an electronically decoupled DTE-BODIPY dyad investigated by pump-probe experiments and theoretical modelling*", The 12th Femtochemistry Conference (FEMTO12) Hamburg/Germany, **2015**

Poster contributions to conferences

1. "*Vibrationally coherent transfer in an electronically decoupled DTE-BODIPY dyad investigated by pump-probe experiments and theoretical modelling*", The 12th Femtochemistry Conference (FEMTO12) Hamburg/Germany, **2015**
2. "*Quantum Dynamics of Ultrafast Energy and Charge Transfer Processes in Organic Photovoltaics*", Summerschool Lyon/France, **2014**
3. "*Multiconfigurational Quantum Dynamics of Ultrafast Energy and Charge Transfer in Organic Polymers*", Faraday Discussions 163, Nottingham/UK, **2013**
4. "*Multiconfigurational Quantum Dynamics of Ultrafast Energy and Charge Transfer in Organic Polymers*", Central European Symposium on Theoretical Chemistry, Mariapfarr/Austria, **2012**
5. "*Multiconfigurational Quantum Dynamics of Ultrafast Energy and Charge Transfer in Extended Molecular Systems*", Open-quantum systems, Birmingham/UK, **2012**

Oral presentations

1. Weekly seminar of the Institute of Physical and Theoretical Chemistry, Goethe University, **2016**
2. Annual seminar of the Institute of Physical and Theoretical Chemistry, Goethe University, Hirschegg/Austria, **2015**
3. Internal group seminar, **2015**
4. Internal group seminar, **2014**
5. Internal group seminar, **2013**

Eidesstattliche Erklärung

Ich versichere an Eides statt durch meine eigene Unterschrift, dass ich die vorstehende Arbeit selbständig und ohne fremde Hilfe angefertigt und alle Stellen, die wörtlich oder annähernd wörtlich aus Veröffentlichungen genommen sind, als solche kenntlich gemacht habe. Die Versicherung bezieht sich auch auf in der Arbeit gelieferte Zeichnungen, Skizzen, bildliche Darstellungen und dergleichen.

Ort, Datum

Unterschrift